UNIVERSITY OF SOUTHAMPTON

Hybrid Optoelectronics with Colloidal Nanocrystals

by

Stefan Rohrmoser

A thesis submitted in partial fulfillment for the
degree of Doctor of Philosophy

in the
Faculty of Engineering, Science and Mathematics
School of Physics and Astronomy

April 2010

UNIVERSITY OF SOUTHAMPTON

ABSTRACT

FACULTY OF ENGINEERING, SCIENCE AND MATHEMATICS

SCHOOL OF PHYSICS AND ASTRONOMY

Doctor of Philosophy

Hybrid Optoelectronics with Colloidal Nanocrystals

by Stefan Rohrmoser

In this work we present spectroscopic studies of the exciton dynamics in colloidal spherical cadmium sulfide CdS nanocrystals (NC) in the vicinity of a single indium gallium nitride $InGaN$ quantum well (QW) in dependence of temperature. QWs of the alloy material $InGaN$ exhibit a dependence of the exciton dimensionality on the thermal energy available. It was demonstrated that this dependence influences the rate for fluorescence resonant energy transfer from the QW to a layer of CdS-NC deposited on top of its capping layer. Investigations of different capping layer thicknesses demonstrated the dependence of the exciton dimensionality on the disorder potential of the QW.

Furthermore, spectroscopic measurements of elongated asymmetric cadmium selenide/-cadmium sulfide $CdSe/CdS$ nanorods (NR) under the application of external magnetic and electric fields are discussed. Asymmetric $CdSe/CdS$-NR represent a special case of elongated NR as the analytical treatment of spherical NC can be combined with numerical methods of calculating the electron and hole energies and wave functions. The results for the excitonic fine structure splitting in these nanomaterials is used to explain the dependence of the exciton dynamics under an external magnetic field. For the first time, a separate measurement of the Zeeman splitting and the magnetic field induced spin admixture in colloidal NR was performed. Electric field mediated carrier separation in asymmetric $CdSe/CdS$-NR is measured in time resolved luminescence quenching experiments. Retrieval of stored excitations is demonstrated employing a synchronised ultrafast voltage pulse detection scheme.

For my daughter Sasha

Contents

List of Figures

List of Tables

DECLARATION OF AUTHORSHIP

I, Stefan Rohrmoser, declare that the thesis entitled 'Hybrid Optoelectronics with Colloidal Nanocrystals' and the work presented in the thesis are both my own, and have been generated by me as the result of my own original research. I confirm that:

- this work was done wholly or mainly while in candidature for a research degree at this University;
- where any part of this thesis has been previously submitted for a degree or any other qualification at this University or any other institution, this has been clearly stated;
- where I have consulted the published work of others, the source is always given. With the exception of such quotations, this thesis is entirely my own work;
- I have acknowledged all main sources of help
- where the thesis is based on work done by myself jointly with others, I have made clear exactly what was done by others and what I have contributed myself;
- parts of this work have been published, the details of which are given overleaf;

Signed:

Date:

LIST OF PUBLICATIONS

S. Rohrmoser, J. Baldauf, R. T. Harley, S. Sapra, A. Eychmüller, I. M. Watson, P. G. Lagoudakis. **Temperature dependence of exciton transfer in hybrid quantum well/nanocrystal heterostructures.** *Applied Physics Letters*, **91**, 092126 (2007).

L. Lagonigro, A. C. Peacock, S. Rohrmoser, T. Hasell, S. M. Howdle, P. J. A. Sazio, P. G. Lagoudakis. **Time and spectrally resolved enhanced fluorescence using silver nanoparticle impregnated polycarbonate substrates.** *Applied Physics Letters*, **93**, 261114 (2009).

S. Rohrmoser, A. Susha, A. Rogach, D. Talapin, H. Weller, R. T. Harley, and P. G. Lagoudakis. **Tuning exchange interaction in colloidal nanocrystals.** *MRS 2007 Fall Meeting*, **GG4.4**, Boston, Massachusetts, USA.

S. Rohrmoser, A. Susha, A. Rogach, D. Talapin, H. Weller, R. T. Harley, and P. G. Lagoudakis. **Tuning exchange interaction in colloidal nanocrystals.** *PLMCN8: 8th International Conference on Physics of Light-Matter Coupling in Nanostructures*, **TuB-7**, Tokyo, Japan.

S. Rohrmoser, A. Susha, A. Rogach, D. Talapin, H. Weller, R. T. Harley, and P. G. Lagoudakis. **Tuning exchange interaction in colloidal nanocrystals.** *CLEO/QELS 2008*, **QWC6**, San Jose, California, USA.

S. Rohrmoser, A. Susha, A. Rogach, D. Talapin, H. Weller, R. T. Harley, and P. G. Lagoudakis. **Tuning exchange interaction in colloidal nanocrystals.** *ICPS 2008*, **Fr-M2e-2**, Rio de Janeiro, Brazil.

A. Peacock, L. Lagonigro, T. Hasell, S. Rohrmoser, S. Howdle, P. J. A. Sazio, and P. G. Lagoudakis. **Silver nanoparticle impregnated polycarbonate substrates for plasmonic applications.** *IEEE LEOS 2009*, **TuA2.3**, Innsbruck, Austria.

Acknowledgements

First and foremost I would like to thank Pavlos Lagoudakis for providing me with this excellent opportunity to conduct challenging and interesting research. It was a remarkable experience to be part of his quickly developing research group and I am thankful for his continuing support.

I am grateful to Richard Harley who, with an extraordinary wealth of scientific insight and experience, always had an open ear for my questions and quirky ideas.

I am greatly indebted to my 'colleagues from the very beginning' Peter Eldridge and Soontorn Chanyawadee who were there day and night. You paved the way guys!

My most heartfelt thanks go to my other colleagues Maria Maragkou, Alastair Grundy, Dave English, Peri Andreakou, Ruiqi Chen and the new hybrids Junis Rindermann and Elena Kammann. You made the whole thing worthwhile!

For the great support without which my research would not have been possible I would like to thank Colin Miles, Tom Perkins, Justin Harris, Vince Davey and all the other support staff at the School of Physics and Astronomy and the Optoelectronic Research Centre.

Last but not least I would like to thank my wife and my family for 'hanging in there' with me.

Chapter 1

Introduction

Humankind's curiosity knows no boundary and its endeavour to understand the principal building blocks of the universe stretched into the realm of the nanoworld in the second half of the 20th century. Since then a lot of effort has been put into developing means to control and construct entities on the atomic scale. This work led to the development of nanomaterials that nowadays come in a vast variety of different constituting chemical elements [1; 2; 3; 4; 5], shapes [6; 7; 8; 9] and assemblies [10; 11; 12; 13; 14]. This work will deal with a special kind of nanomaterial, namely colloidal semiconductor nanocrystals. These have already been researched in the early 1980's [15; 16; 17; 18] however it has not been until the early 1990's that reliable methods of synthesis were developed [19; 20; 21; 22].

Colloidal semiconductor nanocrystals are very interesting because of their excellent spectral tunability that allows one to synthesise nanocrystals that emit in any colour of the visible and near infrared spectrum just by changing their size [23; 24; 25]. The first synthesised nanocrystals featured a luminescence spectrum that was very wide and characterised by a rather low efficiency. However, soon techniques like size selective precipitation [21; 26; 27] and the passivation of dangling surface bonds by epitaxially growing a material with a higher band gap over the core nanocrystal [28; 29] improved the emission properties highly. The scientific field of semiconductor colloidal nanocrystals has since its commencement seen excellent research and continued strong interest, which today leads to a plethora of different nanocrystal applications from fluorescent

labels [30; 31; 32] through spintronics [33; 34; 35] and photovoltaics [36; 37] to light emitting diodes [38; 39] and photodetectors [40]. The popularity of colloidal nanocrystals is evident in the recent announcement by the major display manufacturer LG Innotek to develop a nanocrystal based LCD backlight in collaboration with the University of California Berkeley spin out company Nanosys Inc. All this is evidence for a bright future for colloidal nanocrystals.

1.1 Magnetic field effects

In this work magnetic field effects on the exciton dynamics in special colloidal cadmium selenide $CdSe$ nanorods [41] are investigated. Magnetic field effects on the time-integrated and time-resolved luminescence have been researched since the 1990's. In the seminal work by Efros et al. [42] a decrease in the luminescence lifetime of spherical $CdSe$ nanocrystals upon application of an external magnetic field was described. The nanocrystal luminescence decay at zero field was found to be of the order of μs. The observed increase of radiative rate could successfully be attributed to the ground state being optically inactive in small (radius $< 5\ nm$) spherical nanocrystals. The external magnetic field has the effect of mixing the ground state with higher lying circular dipole allowed states and hence increases the radiative rate. In a later paper [43] the same researchers investigated the magnetic circular dichroism of different sizes of $CdSe$ nanocrystals. The two lowest exciton states have been measured with respect to their Landé g-factor and the oscillator strengths of the respective fine structure levels were ascertained. A crossing of the relative oscillator strengths of two different circular fine structure levels was observed and this could be assigned to the increase of the electron-hole exchange interaction as has been shown earlier [44]. In following work it was possible to perform polarisation resolved spectroscopic investigations on $CdSe$ nanocrystals up to very high magnetic fields of $B = 60\ T$ [45] using pulsed superconducting magnets. In these experiments the development of a circular polarisation with increasing magnetic field was observed. This could be explained by the Zeeman split level's uneven coupling to the optically inactive ground state and an additional bright and dark level mixing induced by the magnetic field.

Significant insight into the behaviour of the emitting fine structure state in medium to strong magnetic fields has been provided by Klimov et al. [46; 47; 48]. The Zeeman splitting of the circular lowest bright states has been investigated up to $B = 45\ T$ and the degree of thermalisation with the dark ground state could be shown for temperatures as low as $T = 1.6\ K$. This work has been refined by performing high resolution single particle spectroscopy under external magnetic fields of up to $B = 33\ T$. In these experiments it was possible to reveal an intrinsic fine structure splitting of bright excitonic states stemming from an asymmetry of the nanocrystals perpendicular to their symmetry axis. This splitting leads to a mixing of the circular bright states into orthogonal composite linear states.

The extensive work of Awschalom et al. [49; 50; 51] investigated the behaviour and manipulation of spins in colloidal semiconductor nanocrystals. Time-resolved Faraday rotation spectroscopy proved an excellent tool to investigate the decay dynamics of optically induced spins in semiconductor $CdSe$ nanocrystals. A spin polarised state in the nanocrystals is achieved by near resonant excitation of the excitonic level with a circularly polarised pump laser pulse of a few hundred femtosecond duration. An external magnetic field induces a quantum beating of the coherent spin states following the Larmor frequency. A linearly polarised time-shifted probe pulse experiences a Faraday rotation by the spin magnetisation in the nanocrystals. It was found that the arbitrary orientation of the individual nanocrystals in the ensemble made the interpretation of the multitude of rotation frequencies measured difficult. However it was possible to assign individual frequencies to the rotation of exciton and electron spins. In their later work this technique was extended to allow for multi-colour time-resolved Faraday rotation spectroscopy which allowed investigation of coherent spin transfer between different nanocrystals molecularly bound using conjugated molecules. The spin transfer was found to be temperature dependent due to a conformational change of the molecular bridge at low temperatures.

1.2 Electric field effects

Another aspect of this thesis is the effect of an electric field on the luminescence dynamics of the investigated nanorods and the combination with the magnetic field effect. Earlier work treating electric field effects in colloidal nanocrystals was mainly performed on single particle samples [52; 53; 54; 55; 56]. Already in one of the first published works on spectroscopy of single $CdSe$ nanocrystals [52] the effect of an electric field has been investigated. A Stark shift quadratic with the applied field has been revealed and using the Stark effect to investigate spectral diffusion showed that the single nanocrystal linewidth is an effect of spectral diffusion and not due to physical effects in the nanocrystals. Later this investigation was extended to symmetrical [53] and asymmetric $CdSe$ nanorods. Spectral shifting, jumping and fluorescence quenching have been observed and attributed to wave function separation and carrier trapping and de-trapping induced by the electric field in the first case. The latter case of asymmetric nanorods allowed a Stark shift to be observed that is asymmetric around zero electric field strength, which is direct evidence for the asymmetry in the crystal structure. In spherical nanocrystals a fluorescence intensity modulation with electric field could be observed in [55]. This was attributed to a modulation of trap states located on the surface of the nanocrystals by the applied electric field and theoretical evidence was supplied. Recently the Stark shift in asymmetric $CdSe$ nanorods could even be used to modulate the fluorescence resonance energy transfer to a dye molecule [56] by actively modulating their spectral overlap. However single particle spectroscopy is not the only means to investigate interesting electric field effects in colloidal nanocrystals. Thus have Kraus et al. [57] shown that an electric field applied to an ensemble of asymmetric nanorods allows one to store part of the fluorescence for up to 10^5 times their natural lifetime. This effect is due to a heterogeneous carrier wave function separation in this special kind of nanorod.

1.3 Fluorescence resonance energy transfer

The third experimental part of this thesis is dedicated to fluorescence resonance energy transfer (FRET) in a multidimensional system. FRET between excitonic systems of

different dimensionality has been theoretically studied by Agranovich et al. [58; 59; 60]. It was demonstrated that different dimensionalities in the donor and acceptor excitonic system will produce a strongly varied dependence of the transfer rate on the donor acceptor separation. In [61] the first example of FRET from an epitaxial quantum well to a dense overlayer of colloidal nanocrystals has been demonstrated and in [62] a 20 fold intensity increase has been demonstrated for FRET from a quantum well to an organic semiconductor. A later work [63] theoretically treated different temperature regimes of this quantum well to nanocrystal FRET and a comparison with experimental results has shown good agreement for the case of high temperatures where the electrons and holes form a plasma of free carriers rather than bound excitons. This prior work led to the development of an electrical FRET pumping scheme from quantum wells to nanocrystals as demonstrated in [64; 39; 38]. Another possible utilisation for such a hybrid system can be found in [36]. In this case the FRET is directed from the colloidal nanocrystals to a vertically structured quantum well *p-i-n* structure. This scheme allowed transfer of 89% of the energy absorbed by the nanocrystals into the *p-i-n* structure and a strong increase in the photocurrent of the device has been observed.

1.4 Overview of thesis

The work at hand is structured into seven chapters, the first of which is this introduction. The second chapter deals with the physical concept of semiconductor crystals and semiconductor nanostructures. We introduce the mathematical framework to describe a bound electron/hole pair, commonly called an exciton, in semiconductor nanostructures. Further we outline the mechanism of fluorescence resonant energy transfer that allows one to resonantly transfer energy between excitonic systems like nanocrystals or quantum wells. We finish chapter two with a short introduction into the colloidal material synthesis and epitaxial techniques used to manufacture nanostructures.

Chapter three is dedicated to the experimental and theoretical methods we employed during our research. We discuss the laser system and both integrated and time resolved spectroscopic techniques that allowed us to investigate the exciton structure and dynamics in our material system. After this we close chapter three with a description of

the numerical methods we applied to calculate the excitonic energy structure in heterostructured elongated colloidal nanorods.

We present our results on magnetic field effects on the energy structure in colloidal nanorods in chapter four. First we explain our findings on the excitonic fine structure in the investigated nanorods. Then we continue to introduce the observed effect of external magnetic fields of up to 8 $Tesla$ on their exciton decay dynamics. At this point we introduce the stretched exponential function, an analytical tool that allows us to compare very complex luminescence decay behaviours. After this, we close the chapter with our findings on the magnetic field effects on individual fine structure levels that could be resolved using polarised detection schemes.

In chapter five, we discuss the effect an external electric field has on the exciton dynamics in the investigated samples. We show theoretical results that allow us to interpret our experimental data. In the last sub-chapter we demonstrate that an electric field pulse scheme can be used to store excitons in the investigated nanorods for much longer than their radiative lifetime.

The final experimental chapter treats the temperature dependence we observed in fluorescence energy transfer processes between quantum wells and nanocrystals. Further, we show results taken from different quantum well samples with varying thickness of the passivating capping layer.

This thesis ends with a summary of the work presented here and an outlook towards future experiments that would allow us to understand the subject matter in further detail.

Chapter 2

Nanostructured Semiconductor Systems

In this work we deal with energy transfer effects between colloidal nanocrystals (NCs) and semiconductor quantum wells (QWs) as well as with changes in the excitonic fine structure in heterostructured colloidal nanorods (NRs) induced by changes in external electric and magnetic fields (E- and B-fields). This chapter is devoted to the introduction of the investigated material systems and their synthesis.

To understand the properties of the material system we will first discuss the concept of a semiconductor and then explain the effect of confinement of carriers in semiconductors. After that we will shortly introduce epitaxial growth of semiconductor nanostructures and the $InGaN/GaN$-QW we used for the energy transfer experiments. Then we will discuss the crystal structure of CdSe and CdS and the influence of the crystal surface on the colloidal growth of heterostructured NR. Following that we will introduce the chemical synthesis of spherical NC and heterostructured NR. There we show the critical influence of the surface energy for the formation of asymmetric NR.

2.1 Electronic structure

Bulk semiconductor materials are characterised by their energy (thermal or optical) dependent conduction properties, and can be differentiated from conductors (metals) and insulators. The reduction of spatial degrees of freedom for charge carriers in semiconductor nano-structures results in fundamental changes in the electronic structure compared to the case of the bulk material. Three dimensional confinement of carriers in semiconductor NCs leads to the formation of very sharp energy levels that dominate the absorption and emission properties. We start the theoretical discussion of semiconductor NCs by treating the case of bulk semiconductors and introducing the effective mass model as a means to calculate the band gap. Further on we will discuss the effective mass model for the case of quantum confined carriers and we will derive their energy states for different confinement strengths.

2.1.1 Bulk semiconductors

All investigated material systems presented in this work (*Cadmium-Selenide* ($CdSe$), *Cadmium-Sulphide* (CdS) and *Indium-Gallium-Nitride* ($InGaN$)) belong to the materials class of 'semiconductors'. The electrical properties of semiconductors lie in between insulators, where the *band gap* E_g (that is the energy difference between the fully filled *valence* (VB) and the empty *conduction band* (CB)) is too large to allow electrons to get excited from the VB into the CB (e.g. diamond: $E_g = 5.4eV$; the values for band gaps throughout this thesis are given at room temperature), and metals where E_g is zero. Semiconductors, like insulators, possess a fully filled VB at zero temperature and an empty CB so that no charge transport can occur. This is understandable using the Pauli exclusion principle: as all available VB levels are already occupied electrons cannot change their present state and hence cannot contribute to electrical conduction. However, contrary to insulators, E_g in semiconductors is small enough (see table 2.1) to allow electrons to be excited across the band gap via thermal or optical excitation. In the VB the electrons leave empty states, the so called 'holes', behind as they get excited into the CB. Both the electron and the hole can contribute to charge transport

Material	E_g eV
Ge	0.70
Si	1.10
$GaAs$	1.40
$CdTe$	1.50
$CdSe$	1.68
CdS	2.46
$ZnSe$	2.74
ZnS	3.62

TABLE 2.1: The band gaps for common semiconductor materials are listed: Germanium Ge, Silicon Si, Gallium arsenide $GaAs$, Cadmium telluride $CdTe$, Cadmium selenide $CdSe$, Cadmium sulphide CdS, Zinc selenide $ZnSe$ and Zinc sulphide ZnS.

as there are many unoccupied states now in both the VB and CB. In semiconductors the E_g is of the order of a few electron volts (eV) so that electrons can be excited by absorption of photons from the visible spectrum that ranges from 750 $nm \equiv 1.65\ eV$ to 380 $nm \equiv 3.26\ eV$. Both CdS and $CdSe$ are so called $II-VI$ semiconductors with Cd from the IIB group of the transition metals and S, Se belonging to the VI main group of chalcogens. Their respective E_g's are $E_{g,CdS} = 2.46eV$ and $E_{g,CdSe} = 1.68eV$.

2.1.1.1 Band structure of Bulk Semiconductors

The energy structure of charge carriers in a semiconductor crystal is defined by the periodic potential formed by the crystal lattice of its constituting atoms. If one disregards electron-electron-interaction this can be treated using a time independent Hamilton operator with a periodic potential $U_a(x) = U_a(x + a)$, where x is a spatial coordinate and a is the lattice constant representing the spatial lattice period. Here we will only consider the 1-dimensional case and extension to the 3-dimensional case can be done in an analogous manner. The corresponding Schrödinger equation is:

$$[H + U_a(x)]\psi(x) = E\psi(x), \tag{2.1}$$

with H being the Hamilton operator, $\psi(x)$ is the carrier wave function and E the energy of the charge carrier. Because of the periodicity of the potential and the time

independent Hamiltonian the solution must be periodic as well, therefore:

$$\psi(x+a) = \psi(x) = e^{ikx} u_k(x). \tag{2.2}$$

which is a plane wave modulated with the same period as the periodic potential, hence $u_k(x+a) = u_k(x)$. This solution is the so called Bloch wave of an electron. Solutions that differ by an integer multiple of $2\pi/a$ are identical. It therefore suffices to only take wave numbers $k \in [-\pi/a, \pi/a]$ into account. All wave vectors fulfilling this condition make up the so called *First Brillouin Zone* of the crystal. Figure 2.1a shows the parabolic dispersion relation of a free electron (continuous grey line). At the Brillouin Zone borders

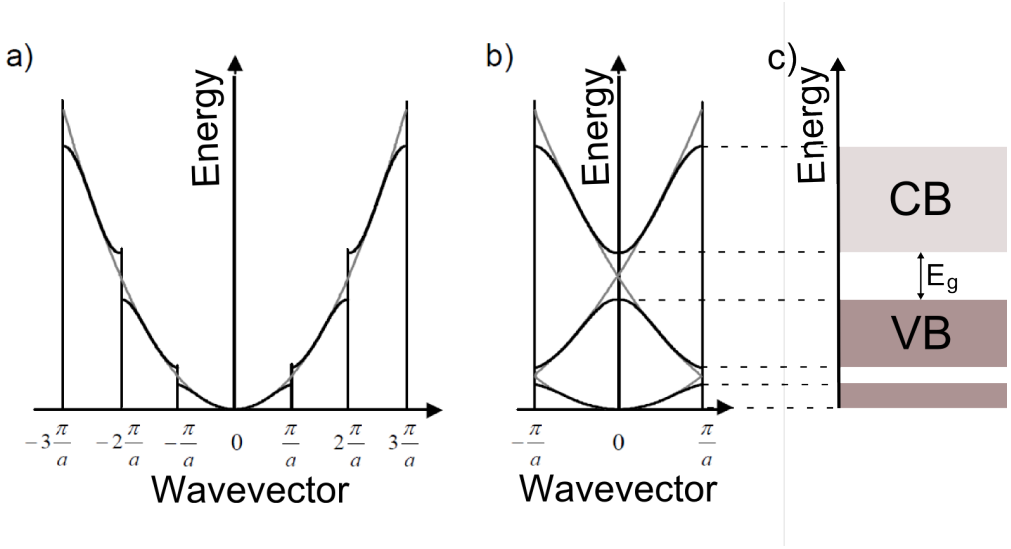

FIGURE 2.1: The dispersion relation of a free electron in the a) extended and the b) reduced zone representation in a 1 dimensional periodic potential with a period of a is displayed. The continuous grey line represents the case of zero potential. Figure c shows the relation between these solutions and the concept of valence band (VB) and conduction band (CB).

($k = \pm\pi/a$) parabolae from adjacent Brillouin Zones intersect and the solution for the Schrödinger equation becomes degenerate. This means, that two different solutions posses the same energy value. The solution is a superposition of two Bloch waves $\psi_+ = \psi_{\pi/a} + \psi_{-\pi/a}$ and $\psi_- = \psi_{\pi/a} - \psi_{-\pi/a}$. One of these standing waves has its antinodes at the position of the atoms whereas the other standing wave's antinodes are in between the atoms. The Coulomb interaction (which describes the electrostatic potential between electrical charges) between the electron and the positively charged atom lifts the degeneracy between these two solutions (at the points indicated by vertical lines

in figure 2.1a). Because of the complete set of solutions being present within the First Brillouin Zone one can show the dispersion relation in the *reduced* representation (see figure 2.1b). The periodicity of the crystal lifts the continuity of the dispersion relation and energetically allowed (*bands*) and forbidden regions appear (see figure 2.1c).

2.1.1.2 Effective Mass

Electronic excitation in semiconductors happens predominantly at extremes of the electronic dispersion relation. The theoretical treatment of semiconductors can for this reason most of the time be limited to values of the wave vectors that lie close to the extremes of the bands. For these k-values the representation of the energy can be expanded in the following Taylor series:

$$E(k) = E_0 + (k - k_0) \left.\frac{dE}{dk}\right|_{k=k_0} + \frac{1}{2}(k - k_0)^2 \left.\frac{d^2E}{dk^2}\right|_{k=k_0} + \ldots \quad . \tag{2.3}$$

We can now set $E_0, k_0 = 0$ and disregard higher order terms. We then derive an equation that closely resembles the parabolic dispersion relation for a free electron:

$$E(k) = \frac{1}{2}k^2 \left.\frac{d^2E}{dk^2}\right|_{k=0} \quad . \tag{2.4}$$

This analogy to the free particle case can be followed even further by assigning to the electron at the CB minimum and to the hole at the VB maximum (a so-called *effective mass*):

$$\frac{1}{m^*} = \frac{1}{\hbar^2} \left.\frac{d^2E}{dk^2}\right|_{k=0} = const, \tag{2.5}$$

with $\hbar$ being the reduced Planck constant. The effective mass can be seen as the strength of the reaction of an electron (hole) to an external force like an electric field and can be measured in exactly this way [65; 66]. Equation 2.5 gives exactly the value for m_0 if applied to the free electron dispersion. Because of its dependence on the form of the dispersion relation, the effective mass is dependent on the direction within the crystal and can even take on negative values [67]. Table 2.2 lists the effective mass and other material parameters used in this work for CdS and CdSe. Note that as the effective

	CdS	$CdSe$
$E_g[eV]$	2.46	1.68
$a_{hex}[A°]$	4.13	4.30
$c_{hex}[A°]$	6.75	7.01
m_e^*	0.20	0.13
m_h^*	$0.7^{\parallel}/2.5^{\perp}$	$0.45^{\parallel}/1.1^{\perp}$
$r_{exc}[nm]$	2.8	4.9
$Ry_{exc}[meV]$	29	16

TABLE 2.2: Important parameters for the semiconductors CdS and $CdSe$ are listed: band gap E_g, hexagonal lattice constants a_{hex}, c_{hex}, effective masses for electron and hole m_e^*, m_h^*, exciton radius r_{exc} and Rydberg constant for the exciton Ry_{exc}.

mass for the hole is dependent on the direction within the crystal lattice, values for two orthogonal directions are given.

2.1.1.3 Excitons

Until now we treated electrons and holes in the bulk crystal as free particles that are created at the same time in the CB and VB respectively. However because of their spatial proximity, one has to take the Coulomb attraction between these oppositely charged particles into account. This electrostatic interaction can lead to composite particles, so called excitons, that are often compared to hydrogen atoms because of their similar energy structure. The excitonic energy levels can be derived from the following Hamiltonian:

$$H = -\frac{\hbar^2}{2m_e^*}\nabla_e^2 - \frac{\hbar^2}{2m_h^*}\nabla_h^2 - \frac{e^2}{4\pi\epsilon\,|\vec{r}_e - \vec{r}_h|} \quad , \tag{2.6}$$

which consists of the kinetic terms for electron and hole respectively plus the Coulomb interaction between the two. Here m_e^* and m_h^* are the effective masses for electron and hole respectively, e is the elementary charge, ϵ is the permitivity of the material and $\vec{r}_{e,\,h}$ are the position vectors for electron and hole. The analogy to the hydrogen atom becomes obvious in formula 2.6 and we can adapt its solution by taking into account the effective masses and the dielectric constant ϵ of the crystal. The Coulomb interaction results in the following excitonic energy eigenstates:

$$E_n = \frac{R_y^*}{n^2} \quad , \tag{2.7}$$

with $n \in 1, 2, 3, ...$ and

$$R_y^* = \frac{e^2}{8\pi\epsilon a_B} \tag{2.8}$$

being the Rydberg energy (ground state energy) of the exciton. In 2.8 we make use of the expression

$$a_B = \frac{4\pi\epsilon\hbar^2}{\mu e^2} \tag{2.9}$$

for the radius of the exciton (here $1/\mu = 1/m_e^* + 1/m_h^*$ is the reduced mass of the exciton) which follows the well-known definition of the Bohr radius in the case of the hydrogen atom. If the exciton is created through the absorption of a photon we can derive for its total energy:

$$E_{exc} = E_g - \frac{R_y^*}{n^2} \tag{2.10}$$

which does not comprise a kinetic term as the photon possesses negligibly small momentum. Because of the effective masses in equation 2.9 being smaller than the electron mass, exciton radii are of the range of several nanometres. The charge carriers therefore are delocalised over several thousand crystal lattice points. This kind of exciton is called a Wannier-Mott-exciton in contrast to Frenkel-excitons which are strongly localised electron-hole-pairs. The Rydberg energy of excitons on the other hand is smaller than for the hydrogen atom and lies in the range of $1 - 100meV$.

2.1.1.4 Spin-Orbit-Interaction

So far we treated the electrons forming the energy bands as not being part of an atom. In real semiconductors these electrons come from the valence orbitals of the constituting atoms. These atomic orbitals have spin and angular momentum degrees of freedom which influence the formation of energy bands in the periodic crystal as well.

In $CdSe$ the CB is formed by the 5s-orbital of the Cd atoms [68; 69] which has an angular momentum of $L = 0$, is isotropic in space and degenerate only by the electron spin. For the VB on the other hand, which is formed by the 4p-orbitals of the Se atoms, the spin-orbit interaction results in significant energy splitting. The total angular momentum in this case is $J = L + s, ..., |L - s| = \{3/2, 1/2\}$. This in turn allows for the exciton's magnetic quantum number the cases $m_J = \pm 3/2$ (the so called *A-exciton*)

and $m_J = \pm 1/2$ (the *B-exciton*). These two bands have different effective masses for the hole and are split by $25meV$ at $k = 0$ [70]. For $J = 1/2$ another split off band (the so called *C-exciton*) appears $420meV$ below the B-exciton [70; 69].

2.1.2 Semiconductor Nanocrystal

In our discussion so far we considered the semiconductor dimensions to be infinite in all three spatial directions and hence we could disregard any effects of the surface or of confinement of the charge carriers. The *density of states* (DOS) of bulk semiconduc-

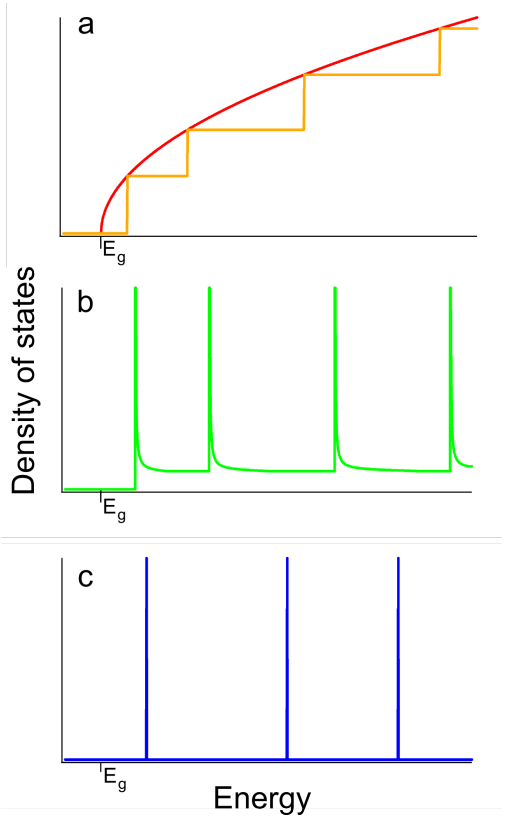

FIGURE 2.2: The density of states for a) bulk semiconductor (in red), quantum well (in orange), b) quantum wire, and c) quantum dot is displayed.

tors therefore increases continuously above E_g (see figure 2.2a). In general one finds the following dependence for the density of states $\rho(E)$ on the dimensionality d of the semiconductor system under consideration and the energy E:

$$\rho(E) \propto E^{d/2-1} \qquad d = 1, 2, 3. \tag{2.11}$$

In thin epitaxially grown semiconductor layers, a confinement of the movement and the momentum of charge carriers along one dimension can be achieved. In these 2 dimensional semiconductor structures, so called *quantum wells* (QW), one finds a steplike DOS (figure 2.2a). Further confinement to the 1 dimensional case can be achieved in *quantum wire* (QWR) structures (figure 2.2b) where the DOS decays as $E^{-\frac{1}{2}}$ above each confined state. The 0 dimensional case (confinement of the movement of charge carriers in all 3 spatial dimensions), is realised in epitaxially grown *quantum dots* (QDs) or in colloidal *nanocrystals* (NCs) (figure 2.2c). By suitable choice of material and growth parameters one can tune the emission energy in these nanostructures over the whole range of the visible spectrum [21; 24] and it is even possible to synthesise white light emitting NCs [71].

We will now extend the theoretical treatment of excitons in bulk semiconductors to the case of NCs. When the radius of a spherical crystallite is reduced until it is comparable with (but is still larger than) the exciton Bohr radius then the kinetic energy of the whole exciton is quantised and can only take on discrete values. This regime is called the *weak confinement* as the exciton is still a composite particle. Reducing the crystallite radius even further so that the exciton's Bohr radius becomes bigger than the spatial extension of the crystal one reaches the regime of *strong confinement*. Here the individual quantisation energies of electron and hole both become larger than their Coulomb interaction and they can be treated as independent charge carriers [72]. Although in the strong confinement regime one can no longer hold on to the concept of an exciton in the traditional meaning, this term has been upheld by the scientific community to define an electron-hole-pair in a semiconductor NC.

2.1.2.1 Solutions of the spherically symmetrical potential

Most NCs used in this work provide full or partial spherical symmetry for the exciton and hence we start with a short treatment of the underlying quantum mechanical problem of the spherically symmetrical potential. The Hamiltonian for this problem with radial

symmetry ($r = \sqrt{x^2 + y^2 + z^2}$) has the following form:

$$H = -\frac{\hbar^2}{2m}\nabla^2 + U(r) \tag{2.12}$$

where m is the mass and $U(r)$ signifies the radial potential. The symmetry of the potential suggests solving the Schrödinger equation in spherical coordinates. This gives for the Laplace operator in spherical coordinates:

$$\nabla^2 = -\frac{\partial}{r^2\partial r}\left(r^2\frac{\partial}{\partial r}\right) - \frac{1}{r^2\sin\nu}\left[\frac{\partial}{\partial\nu}\left(\sin\nu\frac{\partial}{\partial\nu}\right) + \frac{\partial^2}{\sin\nu\partial\phi^2}\right] \quad , \tag{2.13}$$

with r being the radial distance, ν the azimuth and ϕ the radial angle. We can separate the ansatz because of the symmetry of the potential. Without going into all the detail, we arrive at the solution for 2.12 [73]:

$$\psi_{n,l,m}(r,\nu,\phi) = \frac{u_{n,l}(r)}{r}Y_{lm}(\nu,\phi) \quad . \tag{2.14}$$

where the wave function $\psi_{n,l,m}$ separates into a radial part with the spherical symmetrical wave function $u_{n,l}$ and the Laguerre polynomials $Y_{lm}(\nu,\phi)$ that contain the angular dependence of the solution. The energy eigenvalues $E_{n,l}$ depend for the spherical potential solely on the radial part of the Hamiltonian:

$$\left[-\frac{\hbar^2}{2mr^2}\frac{d^2}{dr^2} + U(r) + \frac{\hbar^2}{2mr^2}l(l+1)\right]u_{n,l}(r) = E_{n,l}u_{n,l}(r) \quad . \tag{2.15}$$

with the spherical potential $U(r)$. The solutions for 2.15 are characterised by three quantum numbers: the main quantum number n, the angular momentum quantum number l and its component in the z-direction m. By analogy to the case of the hydrogen atom we symbolise different energetic states by their angular momentum as s-, p-, d- and f-states and each of them is $(2l+1)$ times degenerate ($m = 0, \pm1, \pm2, ..., \pm l$) [73]. In the most basic case the potential $U(r)$ is taken to be a well with potential walls of infinite height:

$$U(r) = \begin{cases} 0 & for \quad r \leq a \\ \infty & for \quad r > a \end{cases} \quad , \tag{2.16}$$

for which the energy eigenvalues are given by the spherical Bessel functions χ_{nl}:

$$E_{n,l} = \frac{\hbar^2 \chi_{nl}^2}{2ma^2} \quad . \tag{2.17}$$

The value of the first spherical Bessel function χ_{10} is exactly π. Because of the inverse square dependence on the radius, it is clear that for small enough NC one can achieve very large quantisation energies.
Using this solution we can now treat the different confinement regimes in semiconductor NC.

2.1.2.2 Weak confinement

In the regime of weak confinement the centre of mass movement of the exciton is quantised and its quantisation energy is smaller than the Coulomb binding energy. A typical example for a material that shows weak confinement of excitons is copper chloride ($CuCl$). There the exciton Bohr radius is $a_{B,CuCl} = 0.7nm$ and the exciton Rydberg energy is $R^*_{y,CuCl} = 190meV$ [70]. Typical NC diameters of $CuCl$ are in the range of a few nanometers and hence are larger than $a_{B,CuCl}$. The total energy of the excitons becomes a sum of the band gap and the binding energy with the quantisation energy as a small correction:

$$E_{n,m,l} = E_g - \frac{R^*_y}{n^2} + \frac{\hbar^2 \chi_{ml}^2}{2Ma} \quad , \tag{2.18}$$

with M being the total mass of the exciton. The quantisation energy for a $CuCl$-NC with a diameter of $2a = 10nm$ is of the order of magnitude of a few μeV and hence much smaller than the Coulomb binding energy.

2.1.2.3 Strong confinement

Taking a material with a bigger exciton Bohr radius or reducing the radius of the nanocrystal even further leads to the regime of strong confinement ($a_{exc} << a_B$) where the actual radius of the exciton is much smaller than the Bohr radius of the exciton in the bulk material. The total energy of the exciton then becomes a sum of

the individual kinetic confinement of the electron and the hole and the band gap (we omit the Coulomb binding energy to first order here):

$$E_{nl} = E_g + \frac{\hbar^2 \chi_{nl}^2}{2m_e^* a} + \frac{\hbar^2 \chi_{nl}^2}{2m_h^* a} = E_g + \frac{\hbar^2 \chi_{nl}^2}{2\mu a} \tag{2.19}$$

with the reduced mass $\frac{1}{\mu} = \frac{1}{m_e^*} + \frac{1}{m_h^*}$. Because of the conservation laws of energy and angular momentum, only transitions between electron and hole states of the same main and angular momentum quantum number are allowed (see figure 2.3). This material system features very discrete energy transitions and it is possible to engineer the energy of these levels by changing the size or the material of the NC (see equation 2.19). For these two reasons one speaks of NC in the strong confinement regime as 'artificial atoms'.

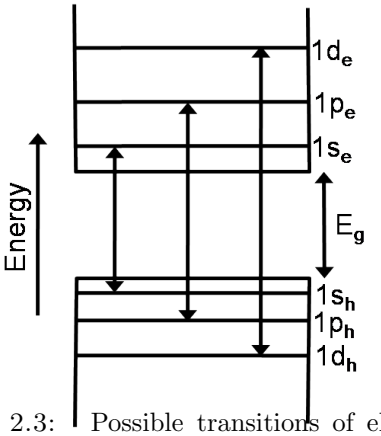

FIGURE 2.3: Possible transitions of electron and hole pairs in a strongly confining quantum dot are shown.

2.1.2.4 Heterostructured confinement

Aside from providing the possibility of strongly confining excitons, NCs also allow for intrinsic spatial separation of the constituting electron and hole. By synthesising nanostructures of two or more materials with different band gaps one can design different spatial areas of confinement for the constituent carriers. In figure 2.4 a schematic of the two different types of confinement is shown. In Type I confinement the conduction band minimum and the valence band minimum are in the same material and electron and hole are confined in the same volume in space. Type II on the other hand features the conduction band minimum in a different material and hence in a different volume

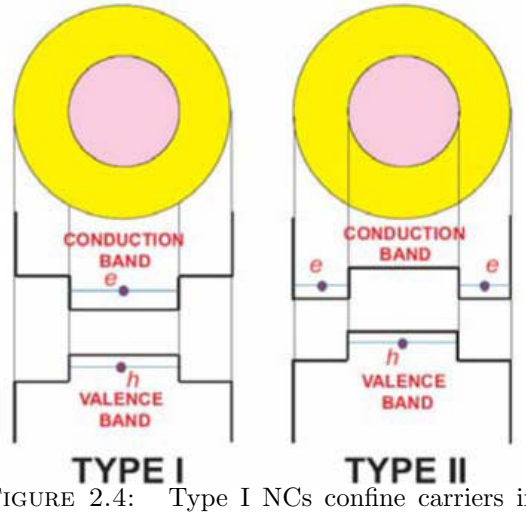

FIGURE 2.4: Type I NCs confine carriers in the same volume whereas in type II NCs the two charge carriers are separated in different volumes.

than the valence band minimum. In this case electrons and holes, though both still subject to strong confinement, are spatially separated in the nanostructure.
In section 2.3.2.2 we will introduce a synthetic method to produce elongated NCs of aspect ratios of up to 5 [41] that feature a nearly spherical $CdSe$ core located on one end of the structure that has been overgrown with a CdS shell. Because of the different valence band minima in the two materials it provides strong confinement of holes in the $CdSe$ core. The conduction band minima on the other hand match in both materials which allows electrons to spread freely over the whole length of the structure.

2.1.2.5 Coulomb interaction

In the above treatment of the strong confinement regime (equation 2.19) we disregarded the Coulomb interaction between electron and hole. However the strong spatial confinement of the charge carriers in nanostructures leads to the Coulomb interaction even becoming enhanced. Although it still remains smaller than the confinement energy it cannot be omitted for a concise treatment of the strong confinement regime [72; 18]. With the electrostatic interaction taken into account the Hamiltonian becomes:

$$H = -\frac{\hbar^2}{2m_e^*(\vec{r}_e)}\nabla_e^2 - \frac{\hbar^2}{2m_h^*(\vec{r}_h)}\nabla_h^2 + V_e(r_e) + V_h(r_h) - \frac{e^2}{4\pi\epsilon\,|\vec{r}_e - \vec{r}_h|} \quad . \tag{2.20}$$

The two independent radially symmetric potentials $V_{e,\,h}(r_{e,\,h})$ and the spatial dependence of the electron and hole effective masses allow for the treatment of type II NCs, because this allows material parameters in equation 2.20 to be set individually for electron and hole.
The Coulomb energy for the creation of an exciton in a strongly confining NC has been treated in several works by variational analysis [18; 23; 74]. Following this the energy of the exciton ground state can be described by:

$$E_{1s} = E_g + E_{quantisation} + E_{Coulomb} = E_g + \frac{\hbar^2\chi_{10}^2}{2\mu a^2} - 1.786\frac{e^2}{4\pi\epsilon a} \quad . \tag{2.21}$$

This correction to the exciton energy leads to a good agreement with experimentally obtained values [72]. The Coulomb interaction is proportional to the inverse NC radius

a whereas the quantisation energy changes with the inverse square of the NC radius. In

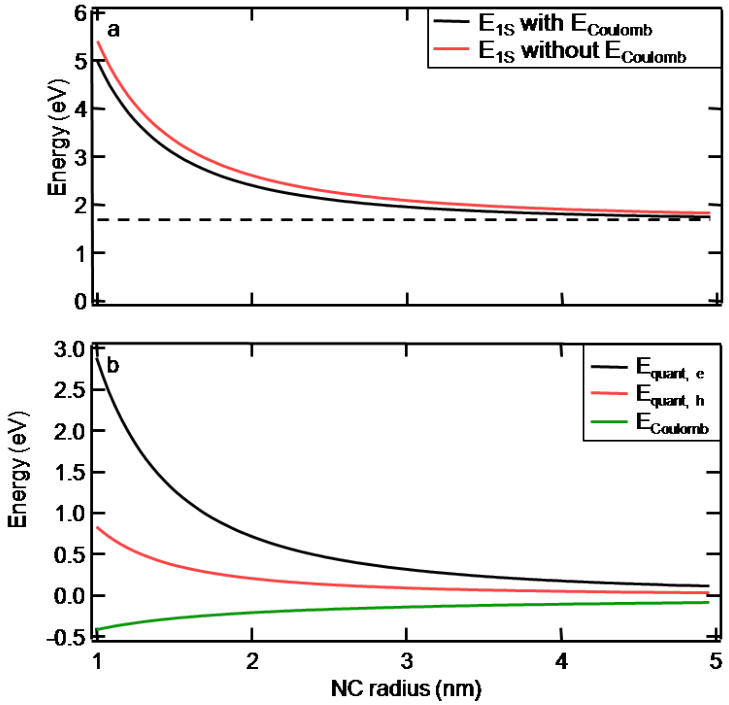

FIGURE 2.5: a) The energy of the first excitonic state $1S$ for a spherical $CdSe$-NC with (black) and without (red) the Coulomb interaction is shown versus the radius. The dashed line signifies the bulk crystal band gap. b) The quantisation energy of the electron (black) and the hole (red) is shown versus the radius of a spherical $CdSe$-NC together with the Coulomb interaction.

figure 2.5a both the energy of the first excitonic state of a spherical $CdSe$-NC with and without the electrostatic interaction are shown as a function of the NC radius. It can be seen that for large NC radii the exciton energy approaches E_g (black dashed line in figure 2.5). Figure 2.5b shows the quantisation energies for electron and hole and their Coulomb interaction separately. The quantisation energy of the hole is reduced with respect to the electron because of its larger effective mass. The heterostructured NCs used in this work have a radius of $2nm$ for which the electrostatic energy is about 20% of the total quantisation energy and cannot be omitted.

2.1.3 Exciton fine structure in NCs

The formula for the exciton structure in strongly confining NCs derived in section 2.1.2.5 is very accurate in describing the large scale absorption spectra of spherical $CdSe$-NC.

However the nature of the emitting exciton state historically proved to be more difficult to explain. Two specific features of the $CdSe$-NC emission (large red shift with respect to the excitation wavelength and much longer radiative lifetime compared to bulk $CdSe$ [19; 42]) required more scientific effort and spurred a variety of theories that tried to explain these phenomena. However in the early 1990's Efros and co-workers presented a realistic multiband calculation of the band-edge exciton fine structure of semiconductor NCs having a degenerate valence band. In this comprehensive theoretical study electron-hole exchange interaction, non-sphericity of the NC shape and the intrinsic hexagonal lattice asymmetry have been taken into account.

In the framework of the effective mass approximation (see 2.1.1.2) the first quantum size level of electrons is a $1S_e$ state that is doubly degenerate with respect to its spin projection. The first quantum size level for the hole is a $1S_{3/2}$ state that is four-fold degenerate with respect to the projection of its total angular momentum ($M = 3/2, 1/2, -1/2, -3/2$). The first excited state of the composite exciton is consequently eightfold degenerate. We will explain below the energy terms that lift this degeneracy when crystal field splitting, shape asymmetry and exchange interaction are taken into account.

2.1.3.1 Crystal field splitting

In the earlier discussed model (see 2.1.1.2) the bulk conduction and valence bands are approximated to be parabolic at $k = 0$. However the real band structure significantly differs from this approximation and especially the valence band deviates because of the strong spin-orbit interaction ($\Delta_{so} = 0.43eV$ for $CdSe$) [69]. In ideal diamond-like semiconductors this interaction causes the valence band to split up into the fourfold degenerate heavy and light hole bands (generally referred to as A and B subband) and the split off band (referred to as C subband). The C subband can be neglected for our purposes as its energetically far away from the A and B subbands. The $CdSe$ crystal structure is different from an ideal diamond like structure as it has no inversion symmetry along its unique $\hat{c}$-axis. The crystal field arising from this symmetry breaking lifts the degeneracy of the A and B subbands at $k = 0$. This crystal field splitting is small in

bulk $CdSe$ ($\Delta_{cf} = 25meV$ [75]) and is usually neglected. However this term causes additional splitting of the exciton fine structure and cannot be neglected for our work. In Efros et al. [76] the crystal field splitting was treated using first order perturbation theory for the case of a spherical NC. A formula that only depends on the mass ratio between the light and the heavy hole β describing this splitting Δ_{int} has been derived there:

$$\Delta_{int} = \Delta_{cf}\nu(\beta), \tag{2.22}$$

where $\nu(\beta)$ is a function of the light to heavy hole mass ratio. This formula is valid as long as the crystal field splitting Δ_{cf} is much smaller than the quantisation energy of the holes. For $CdSe$-NCs of the size we investigated this condition is fulfilled. We employed this approximation for our work because the crystal field splitting acts only on valence band states and as we explained earlier (2.1.2.4) the hole is subject to spherical confinement in the heterostructured NR we investigated.

2.1.3.2 Shape asymmetry splitting

In addition to term 2.22 already mentioned, slight deviations of the NC shape from the perfect spherical form add to the splitting between the higher $1S_{\pm 3/2}$ and the lower $1S_{\pm 1/2}$ hole states. A similar approach to the one described in chapter 2.1.3.1 has been used to derive the shape asymmetry splitting [76]. The surface of crystals whose shape differs slightly from a perfectly spherical one can be described by the following equation:

$$\frac{x^2 + y^2}{b^2} + \frac{z^2}{c^2} = 1. \tag{2.23}$$

By using the following change of variables $x \Rightarrow bx/a$, $y \Rightarrow by/a$ and $z \Rightarrow cz/a$ one can convert equation 2.23 into the equation for the surface of a sphere with radius a: $x^2 + y^2 + z^2 = a^2$. Applying the same change of variables to the Hamiltonian separates it into the following form:

$$\hat{H} = \hat{H}_L + \hat{V}, \tag{2.24}$$

with $\hat{H}_L$ being the so called Luttinger Hamiltonian that describes the unperturbed spherical NC and $\hat{V}$ the anisotropic perturbation resulting from the shape asymmetry.

This means that the hole movement in the elliptical NC is now reduced to its movement in a spherical NC that is described by the anisotropic Hamiltonian 2.24.
If the elliptical shape of the NC only differs insignificantly from a sphere with radius $a = (b^2c)^{1/3}$, we can introduce an ellipticity parameter μ in the following way

$$\frac{c}{b} = 1 + \mu. \tag{2.25}$$

For prolate NC μ is positive and for oblate NC $\mu < 0$ holds true. If $|\mu| << 1$ one can consider the anisotropic term $\hat{V}$ in 2.24 to be a small perturbation. Using analytically derived wave functions [76] for the $1S_{\pm 3/2}$ and $1S_{\pm 1/2}$ hole states one can calculate this small perturbation to be:

$$\Delta_{sh} = 2\mu u(\beta) E_{3/2}(\beta). \tag{2.26}$$

Here $u(\beta)$ is a function that only depends on the mass ratio between light and heavy hole and $E_{3/2}(\beta)$ is the ground state energy of a $1S_{3/2}$ hole state in a spherical NC with radius $a = (b^2c)^{1/3}$. Because of the nearly spherical confinement of the hole in the investigated heterostructured NR we used this approximation in our work and set $\mu = 0$.

2.1.3.3 Exchange interaction

A further perturbation of the general Hamiltonian 2.20 that lifts the exciton fine structure degeneracy in NCs even more is the electron-hole-exchange interaction. The two terms from 2.22 and 2.26 split the states with different hole spin but the exchange interaction takes effect on degenerate excitonic states that have the same total angular momentum projection $F = M + s_z$, with M being the total angular momentum projection of the hole state and s_z the spin projection of the electron state. Again by treating the exchange interaction in the framework of first order perturbation theory [42] and by using the exchange Hamiltonian

$$\hat{H}_{exch} = -\frac{2}{3}\epsilon_{exch} a_0^3 \delta(\vec{r}_e - \vec{r}_h)\sigma J, \tag{2.27}$$

with ϵ_{exch} the exchange strength constant, a_0 the lattice constant, $\delta(\vec{r}_e - \vec{r}_h)$ the Dirac delta function, σ the Pauli spin-1/2 matrix for the electron and J is the hole spin-3/2 matrix, one can derive a term for the splitting and finally find expressions for the fine structure energy levels ϵ_F of the exciton. For this purpose one has to solve the eigenvalue problem $det(\hat{E} - \epsilon_F) = 0$, where the matrix $\hat{E}$ consists of elements of the asymmetry perturbations and the exchange Hamiltonian 2.27, taken between the exciton wave functions $\Psi_{s_z,M}(\vec{r}_e, \vec{r}_h) = \psi_{s_z}(\vec{r}_e)\psi_M(\vec{r}_h)$. The so deduced energy levels are labelled in terms of the exciton total angular momentum projection: one level with $F = \pm 2$, two levels with $F = \pm 1$ and two with $F = 0$. The energy levels are as follows:

$$\begin{aligned} \epsilon_2 &= -\tfrac{3\eta}{2} - \tfrac{\Delta}{2}, \\ \epsilon_1^{U,L} &= \tfrac{\eta}{2} \pm \sqrt{\tfrac{(2\eta-\Delta)^2}{4} + 3\eta^2}, \\ \epsilon_0^{U,L} &= \tfrac{\eta}{2} + \tfrac{\Delta}{2} \pm 2\eta, \end{aligned} \tag{2.28}$$

where the superscripts U, L signify the respective upper and lower level and the total asymmetry term is $\Delta = \Delta_{sh} + \Delta_{int}$. The η in 2.28 represents the exchange splitting and it is proportional to the wave function overlap of electron and hole $\eta = \alpha \int (\psi^*_{s_z})^2(\vec{r}_e)\psi^2_M(\vec{r}_h)d\vec{r}$, where α represents a constant that we adjusted in order for our numerical data to fit the analytical results presented in [42].

2.2 Fluorescence resonance energy transfer

In general any phenomenon during which energy is being transferred between two states in two different excitonic or electronic systems can be referred to as an energy transfer process. This involves mechanisms such as emission and subsequent absorption of a photon, electron transfer and fluorescence resonance energy transfer (FRET). The latter is a resonant interaction of the multipole field of the charge distribution between a donor and an acceptor where the excitation energy of the donor is transferred to the acceptor. Because of the resonant nature of this process it works without the generation of a photon and subsequent absorption of this photon. In this chapter we are going to lay out the theoretical background of FRET and in chapter 6 we will describe the experiments we

performed on the temperature dependence of FRET between donors and acceptors of different dimensionality.

2.2.1 General principle (case of pointlike dipoles)

The process of fluorescence resonance energy transfer was first investigated by T. Förster in 1948 [77]. Based on the Born-Oppenheimer-approximation he assumed the movement of the participating fluorescent organic molecules to be much slower than the FRET process. Consequently Förster could describe the eigenfunction of the molecules as functions of the electron coordinates. For this reason his treatment of FRET was limited to the case of pointlike dipoles where the Born-Oppenheimer-approximation holds true. The process of any FRET interaction can universally be described in five steps [78], see figure 2.6:

1. the donor absorbs a photon of energy $\hbar\omega_0 = \epsilon_{D,n_0}$ and an exciton is generated in the n_0^{th} excited state (resp. an electron is lifted into its n_0^{th} excited state).

2. the exciton (resp. electron) relaxes under the emission of phonons to a lower energy level with energy $\epsilon_{D,n_1} \leq \epsilon_{D,n_0}$. In the classical description of FRET this level needs to be dipole allowed [77], however in later works higher multipole moments have been included into the theory although these terms are much smaller than the second order terms [78].

3. the energy ϵ_{D,n_1} is transferred from the donor to the acceptor via resonant multipole interaction. The main contribution comes from dipole-dipole interaction but quadrupole interaction and exchange interaction need equally to be taken into account [78]. An exciton of the energy $\epsilon_{A,n_0} = \epsilon_{D,n_1}$ is created in the acceptor or an electron is lifted into its n_0^{th} excited state in the acceptor.

4. the exciton (resp. electron) relaxes under the emission of phonons to a lower energy level with energy $\epsilon_{A,n_1} \leq \epsilon_{A,n_0}$.

5. the excitation decays and the acceptor emits a photon of the energy $\hbar\omega_1 = \epsilon_{A,n_1}$.

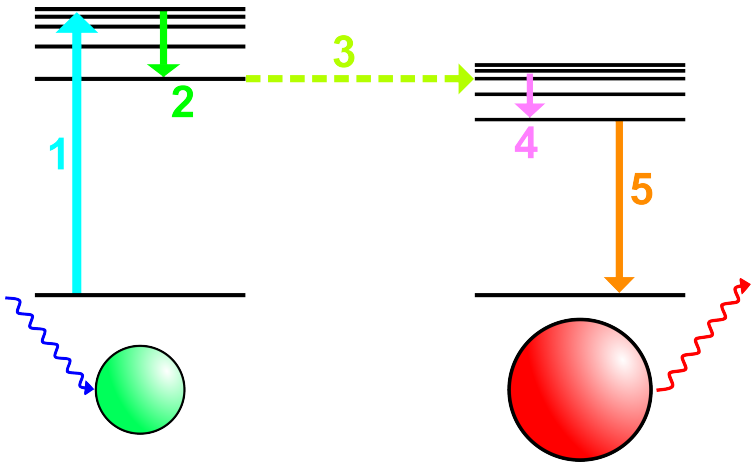

FIGURE 2.6: The general concept of FRET is shown for two fluorescent species in five steps: 1) donor absorption, 2) donor relaxation, 3) donor-acceptor transfer, 4) acceptor relaxation and 5) acceptor emission.

It was found that the FRET process is critically dependent on the distance r between the donor and the acceptor molecules. A dependence proportional to $\frac{1}{r^6}$ was found, however in later works it was shown that this dependence can change dependent on the dimensionality of the donor and acceptor multipoles. The distance at which the efficiency of the FRET decreases by 50% is generally known as the Förster radius and for pointlike dipoles it is:

$$R_F \sim \sqrt[6]{\frac{\kappa^2 \eta_D^0}{n^4} I_{D-A}}. \tag{2.29}$$

The Förster radius is dependent on the following parameters: κ which is the orientation parameter of the donor to the acceptor dipole, η_D^0 which is the quantum efficiency of the donor in the absence of an acceptor, n which is the average refractive index of the matrix/liquid around the donor and I_{D-A} which is the overlap integral between the donor fluorescence spectrum and the acceptor absorption spectrum (see figure 2.7). The Förster radius is widely used in scientific publication in order to classify quantum systems in terms of their ability to perform FRET. Typical values of R_F are in the range of a few nanometres. The dependence of the FRET process on the relative orientation of the donor and acceptor dipoles is easily comprehensible because dipoles that are oriented perpendicularly cannot interact. The quantum efficiency of the donor is a direct measure for its optical activity. If the excitation relaxes to a trap state or an optically inactive state in step two of the FRET process, then the probability for the transfer to happen

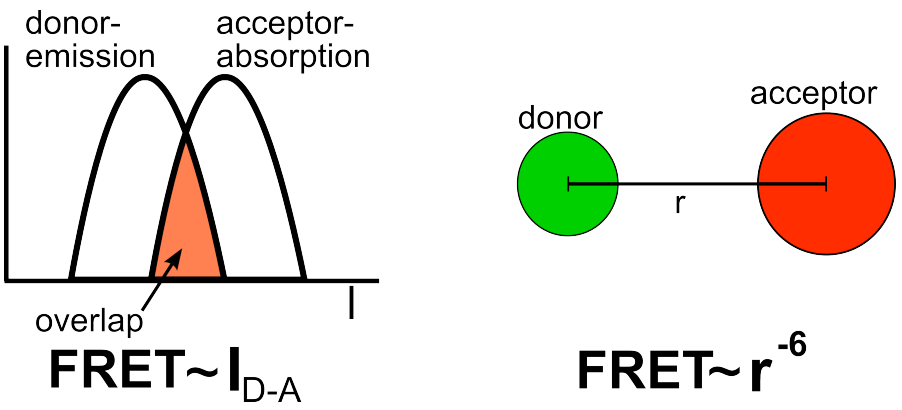

FIGURE 2.7: On the left a schematic depiction of the donor-acceptor spectral overlap and its relation to FRET is shown and on the right the strong dependence of FRET on donor-acceptor separation is indicated.

diminishes. This is due to the fact that higher order terms in the multipole expansion are generally smaller than the quadratic term. The overlap integral between donor and acceptor in formula 2.29 is the overlap only between the respective donor and acceptor involved in the process. Although in general observed in ensembles of emitters, FRET genuinely is a microscopic process.

Given the Förster radius R_F and the fluorescence lifetime of the donor τ_D one can calculate the FRET decay rate k_{FRET} to be:

$$k_{FRET}(r) = \frac{1}{\tau_D}\left(\frac{R_F}{r}\right)^6 \tag{2.30}$$

By appropriate choice of donor and acceptor (e.g. maximising the spectral overlap, the donor's quantum efficiency and minimising the donor's radiative lifetime) and by beneficial design of the donor-acceptor geometry (minimising the donor-acceptor-distance) one can achieve very high FRET efficiencies.

2.2.2 Resonant energy transfer with quantum well donor structures

After the initial treatment of pointlike dipoles much research has been done on different emitting species and different emitter geometries [79; 80; 64; 81; 36]. Experimental [63; 82] and theoretical work [58; 59] has shown that energy transfer rates between excitations in quantum wells and layers of pointlike emitters feature a multitude of

different regimes. In Basko et al. [59] a comprehensive theoretical study of energy transfer with QW donors has been presented. The system investigated in Basko et al. [59] is depicted in figure 2.8. A QW of thickness L_w is confined between two barriers of thickness L_b and the half space on both sides of this structure is considered to be homogeneously filled with an organic emitter. For the calculations presented here this emitter is assumed to possess a continuum of states at the energy of the QW excitation. This can be justified as well for nanocrystals if QW emission wavelength and the NC ground state energy are well enough separated. The dielectric constants of the system are as follows:

$$\varepsilon_{ij}(\mathbf{r}) = \begin{cases} \epsilon_b \delta_{ij} & for \quad |z| < L_w/2 + L_b, \\ \tilde{\epsilon}\delta_{ij} & for \quad |z| > L_w/2 + L_b, \end{cases} \tag{2.31}$$

where $z = 0$ is taken to be at the centre of the QW. ϵ_b is assumed to be real and $\tilde{\epsilon}$ is assumed to have an imaginary part as well. Using a quantum mechanical approach the energy transfer rates from the QW to the organic emitter have been calculated for the case of free excitons, localised excitons and free carriers. For the system in figure 2.8 we

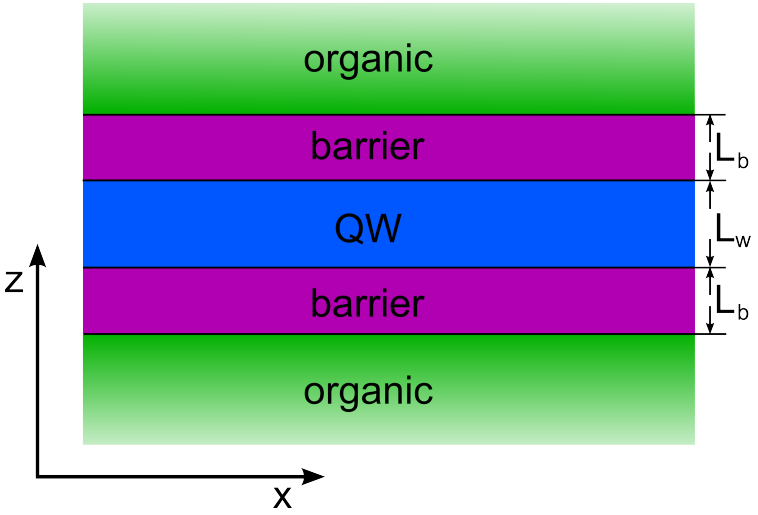

FIGURE 2.8: A schematic depiction of a QW sample with deposited organic fluorescent material is shown. By changing the QW size L_w and the barrier size L_b overlap and donor-acceptor separation can be tuned respectively.

can write the Hamiltonian for the Coulomb dipole-dipole interaction between the QW and the organic medium, which governs the energy transfer process, as

$$\hat{H}_{int} = -\int d^3\mathbf{R}(\hat{\mathbf{P}}^{org}(\mathbf{R}) \cdot \hat{E}(\mathbf{R})), \tag{2.32}$$

here $\hat{E}(\mathbf{R})$ is the operator for the electric field, produced by the QW polarisation operator $\hat{\mathbf{P}}^{QW}(\mathbf{r})$, $\hat{\mathbf{P}}^{org}(\mathbf{R})$ is the operator of the organic medium polarisation (dipole moment per unit volume), finally $\mathbf{r}$ and $\mathbf{R}$ are position vectors for excitons in the QW and the organic emitter respectively. The electric field $\hat{E}(\mathbf{R})$ can be found, just like in classical electrostatics, via the QW polarisation and the appropriate Green's function. With 2.32 one can calculate the energy transfer rate by applying Fermi's Golden Rule [83]:

$$\frac{1}{\tau} = \frac{2\pi}{\hbar} \int d^3\mathbf{R} \int d\nu \left|\mathbf{d}^{\nu}(\mathbf{R}) \cdot E^{vc}(\mathbf{R})\right|^2 \delta(E_\nu - \hbar\omega), \tag{2.33}$$

where ν is a set of quantum numbers describing the excited state in the acceptor molecule, $\mathbf{d}^{\nu}(\mathbf{R})$ is the matrix element of the dipole moment between the acceptor's excited and ground state, $E^{vc}(\mathbf{R})$ signifies the electric field of the QW excitation at the position of the acceptor molecule and E_ν and $\hbar\omega$ are the energies of the acceptor and the QW exciton respectively. Following this recipe the transfer rates of free excitons, localised excitons and free carriers in the QW have been calculated:

- Free excitons extend over many lattice constants in the QW plane and can be seen as 2D bound electron hole pairs. The free exciton can be described using a plane wave. The polarisation in the QW in this case is given by the product of the 1S-wave functions of the relative electron and hole motion at the origin. The energy transfer rate resulting from this is only weakly dependent on L_w but shows an inverse exponential dependence on L_b.

- Localised excitons occur in QW due to the random potential caused by width fluctuations and alloy disorder. In this case the exciton is no longer a plane wave. However the exciton wave function $\Phi_{\mathbf{K}}$ ($\mathbf{K}$ is the exciton wave vector) needs to fulfil the following properties: (i) it should be localised within some distance $L \gtrsim L_w$, (ii) it should be smooth and without nods [84]. By means of the localisation length one can distinguish two important cases:

$$\begin{aligned} &L_b \ll L \quad \text{then the transfer rate becomes:} \frac{1}{\tau} \propto \frac{1}{L} \\ &L_b \gg L \quad \text{implies } L_b \gg L_w, \text{the transfer rate becomes:} \frac{1}{\tau} \propto \frac{|\Phi_{\mathbf{K}=0}|^2}{L_b^3}. \end{aligned} \tag{2.34}$$

This shows how in the same QW system very different energy transfer regimes can occur dictated by the randomness of the confinement potential.

- Free charge carriers form initially upon optical excitation of a QW. Following the same recipe as before it can be derived, that the recombination rate of the free charge carriers depends strongly on their respective concentrations. However, it was shown [59] that the recombination of free carriers is by about 2 orders of magnitude slower than the relaxation to excitons via phonon emission.

The treatment has later been extended to NC acceptors [63]. In this work it was assumed that only a single layer of NCs has been deposited on top of a QW structure. The theoretical treatment of this structure used the quantum mechanical approach employing the Fermi Golden Rule as well. However slightly different dependencies of the transfer rates on the donor-acceptor separation **R** have been found:

$$\frac{1}{\tau} \propto \begin{cases} e^{-2KR} & \text{for free excitons,} \\ \frac{L^2}{(L+R)^4} & \text{for localised excitons with localisation length } L. \end{cases} \tag{2.35}$$

In chapter 6 we will show that these regimes can be investigated within one system by changing the thermal energy of the system.

2.3 Material synthesis

The experiments presented in this work have been performed using three different kinds of nanostructured materials that were not only produced employing very different methods but were as well made of varying materials. The following section introduces the two general methods that were used to fabricate the investigated nanostructures: *Metal-organic Chemical Vapor Deposition* (MOCVD) and *Colloidal Growth*. Then each method is discussed with respect to the respective exact parameters and process steps used. For the case of the colloidal growth, the importance of the crystal structure and how it can be used to grow colloidal structures with heterogeneous confinement of electron and hole will be explained.

2.3.1 Metal-organic Chemical Vapour Deposition

MOCVD is one of the most widely used techniques for epitaxial growth of $III-V$-thin film structures in the semiconductor industry. Since its introduction in the late 1970's it has been adapted by many leading optoelectronic-devices manufacturers to produce devices such as lasers, LEDs, solar cells and photodetectors on a large scale.

2.3.1.1 Principle of operation

The main advantage of MOCVD over *Molecular Beam Epitaxy* (MBE) is that it does not require an *Ultra High Vacuum* (UHV) environment to provide pure ballistic transport of the reagents from the source material to the sample and therefore it is less expensive and less time consuming to operate. However an MOCVD setup needs to be absolutely Oxygen free as contamination with O can degrade the grown structures dramatically. Disadvantages are that the growth is influenced by more independent parameters and that in-situ analysis is not as common and exact as in the case of MBE grown structures.

In MOCVD the source material for the group-III elements is commonly supplied in the form of a liquid or granular organic compound precursor whereas the group-V source material is provided as gaseous hydrides. The hydrides especially pose problems as they need to be stored under high pressure, are explosive and toxic. Therefore to run an MOCVD machine it is essential to keep a relatively expensive safety system in place to dispose of and safely handle the waste material. Recently different group-V precursors (alkyls like tertiary butyls of As or P) have been investigated for the use in MOCVD to circumvent these problems. These alternative source materials however need different growth parameters and lead to different layer properties [85; 86; 87]. The precursor materials are transported by an inert carrier gas (H_2 is used traditionally but because of security concerns can be replaced by N_2) to the reaction chamber. The growth, unlike in MBE where the atomic species travel to the substrate ballistically, is initiated by heating the substrate and cracking the precursor molecules in close proximity of the substrate where they then react. Figure 2.9 shows a simplified schematic of an MOCVD setup.

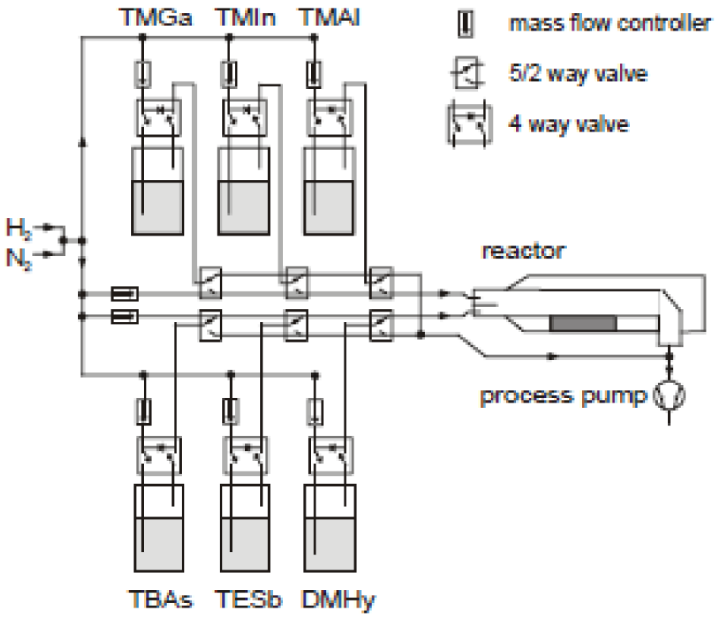

FIGURE 2.9: A simplified drawing of an MOCVD growth setup is shown. The carrier gas is supplied to the system from the left. Organic precursor materials are connected via 4-way valves to the main supply line. 5/2-way valves are used for the admixture of the growth materials and the supply to the reactor.

To be able to precisely tune the growth parameters, one needs to be able to exactly control the material flow of the precursor material to the substrate. For the gaseous source materials this can be obtained by using fast switching valves. In the case of the liquid or fine granular source materials, stainless steel bubblers are used that are held under a constant temperature to keep the vapour pressure fixed. The carrier gas is guided through the bubbler using a *Mass Flow Controller* (MFC) and a *pressure controller* (PC) at the exit controls the admixture of the precursor with the carrier gas (see figure 2.10 for details). The vapour pressure of the precursor material is a very important parameter since it determines the concentration of the source material in the reactor and hence the deposition rate. Too low a vapour pressure makes it difficult to transport the source material and a too large vapour pressure may raise safety concerns.

The carrier gas serves the purpose of transporting the precursor molecules to the reactor and there to help in cracking them so that the respective atoms can react at the surface. For the reactor there exist two common designs where the sample is mounted either parallel or normal to the carrier gas flow. The horizontal reactor design is the most common and hence there exists a lot of experience in its usage. The major advantage is

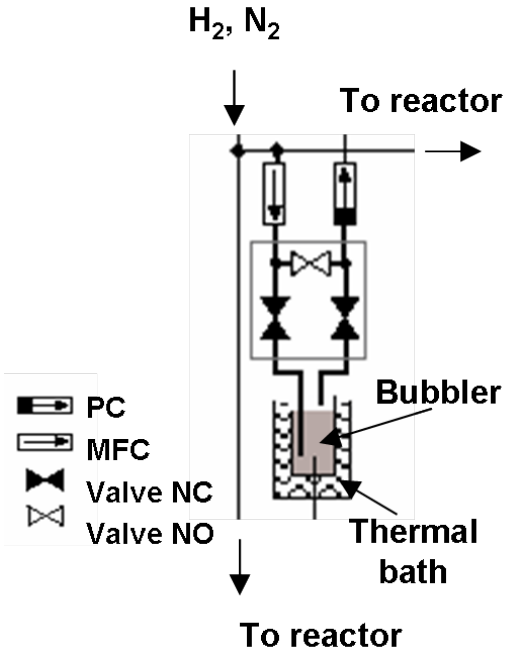

FIGURE 2.10: A detailed schematic of the supply chambers containing the precursor materials is shown. The carrier gas is supplied via a multi function controler (MFC) and an arrangement of valves controls the gas flow. The organic precursor material is desolved in a thermally regulated bath. A pressure control (PC) regulates the back flow of the growth material carrying gas into the system.

of uniform sample growth, provided care is taken that the gas flow occurs in a laminar fashion. In addition a very fast switching between composite materials is possible as the gas flow needs to be very high. However in horizontal reactors it is difficult to implement a high throughput production. This can be achieved by using vertical reactors that allow for a very efficient precursor usage and the growth on large and multiple wafers. Nevertheless vertical reactors are not used as often in research because of the possible memory effects and high rotation speeds needed for the substrate to avoid carrier gas convection.

2.3.2 Fabrication of 0 dimensional nano structures

One generally can discern between two different approaches to produce QDs: the so called *top-down* and the *bottom-up* approaches. In the first, macroscopic objects are being treated and structured using lithographic or etching techniques to produce microscopical samples. The latter approach on the other hand uses self assembly and colloidal

chemistry to synthesise 0 dimensional structures.

Methods like the earlier discussed MOCVD or MBE growth can be used to created self assembled QDs on a substrate. With this method a certain lattice mismatch between two different crystal species is used to create strain in an epitaxially overgrown layer. In order to minimise surface tension insular structures form that provide quantum confinement, so-called epitaxial QDs. The 0 dimensional structures used in this work, on the other hand, were all produced using colloidal chemistry and are generally referred to as *colloidal nano crystals* because they are suspended in a liquid solvent. In this chapter we will describe the general synthesis of NCs and then describe the special species of NC that were used in this work.

2.3.2.1 Synthesis of colloidal nanocrystals

Colloidal NCs are commonly known for their excellent spectral tunability as well as for their flexibility in the usable materials and the achievable geometries. In figure 2.11 examples of these properties are shown. The most widely used and most successful NC synthesis starts with the pyrolysis of metal-organic (e.g. Cadmium dimethyl $Cd(CH_3)_2$ and Trioctylphosphineselen $TOP-Se$) precursor materials in a hot ($300°C-360°C$) coordinating solvent. The approach consists of organic molecules (e.g. *TOP*, Trioctylphosphineoxide *TOPO*, oleic acid, Hexadecylamine *HDA*), that eventually passivate the NC surface, dissolved in a non-polar organic solvent. A quick initial injection of the metal-organic into the hot coordinating solution decomposes the precursor materials and creates a supersaturation of monomers. This supersaturation is initially reduced by the formation of nucleation centres from the monomers. The prior injection of the precursor materials additionally reduces the temperature of the solution far enough in order to stop the formation of nucleation centres. This is the first phase of the NC growth, the so called *size-focusing* regime, where the remaining monomers in the still highly concentrated solution add to the nucleation centres. The name stems from the fact that the NC size distribution does not broaden during this regime and highly monochromatic NC can be extracted. The size focusing phase is characterised by relatively fast growth rates. After further depletion of the monomer concentration the temperature can be

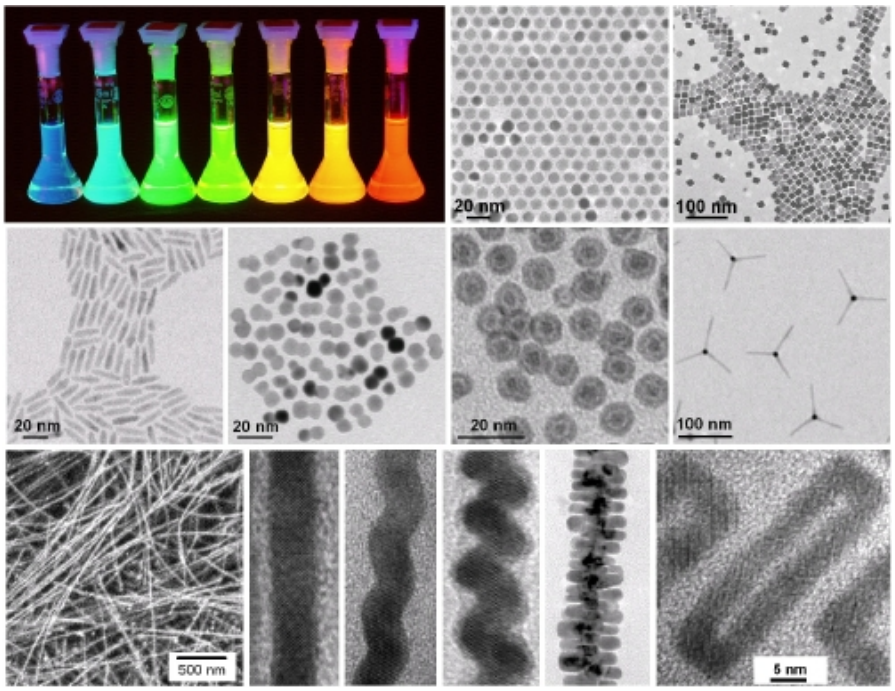

FIGURE 2.11: A selection of nano crystals of different shapes and compound materials is shown. In the top left a size series of *CdS*-NC can be seen luminescing in all colours of the visible spectrum.

reduced and the NC growth becomes dominated by the so called Ostwald ripening. This process is the decomposition of smaller NCs which have a higher surface energy for the benefit of larger NCs which are thermodynamically more stable. Because of the size discriminating nature of this growth regime it is characterised by a broadening of the NC size distribution and hence the emission spectrum widens as well. The peak emission wavelength on the other hand does not change as rapidly as during the size focusing regime. Ostwald ripening first reduces energetically unfavorable surface areas, edges and corners of the NC. Finally, by quickly decreasing the temperature down to room temperature, the growth process is stopped and surface passivated colloidal NCs are obtained.

The so-produced NCs usually show a size dispersion of about $10\% - 15\%$. This is far from representing an ensemble of monochromatic emitters which is of critical importance for many spectroscopic studies. A strong reduction of the NC polydispersity can be achieved by the process of *size selective precipitation*. During this procedure a polar non-solvent, typically Methanol, is added to the prior synthesised colloid. This non-solvent mediates

the precipitation of part of the NCs in solution. The larger NCs preferentially precipitate first due to the fact that they posses a larger surface area and hence the larger NCs become unstable first. Centrifugal separation of the thus-depleted colloid helps to separate the larger precipitated NCs from the remaining solution. The precipitate can then be redissolved in the respective solvent and the size selective precipitation iterated. In this way several sub-ensembles of NCs with increasing mean radii can be produced that have a size dispersion of $\leq 5\%$ rms.

The *quantum efficiency* (QE) of a series of successively precipitated sub-ensembles of NCs follows a Gaussian distribution. This is a direct consequence of the process of Ostwald ripening. During Ostwald ripening smaller particles are deconstructed for the sake of larger ones. Therefore the NC on the flanks of the size distribution are undergoing constant change and this makes their crystal structure the most error-prone which reflects in their lower QE. To ensure a high level of control over the NC growth it is very important to make the right choice in terms of precursor materials, surface stabilisers, solvents and growth parameters used. By varying the material components or the growth conditions one can greatly influence the obtained QE, emission wavelength, full-width-at-half-maximum (FWHM), solubility, material composition and physical shape of the synthesised NC.

In the present work two different kinds of NC were used: nearly spherical Cadmium sulphide (CdS) and heterostructured Cadmium selenide\Cadmium sulphide ($CdSe\backslash CdS$)-NCs. The former were synthesised following the earlier-described procedure with the only difference being that Cadmium oxide (CdO) and Trioctylphosphinesulphide $TOP-S$ were used as precursors instead of $Cd(CH_3)_2$ and $TOP-Se$. The synthesis of the heterostructured NCs requires a more sophisticated approach and will be explained in the following subchapter.

2.3.2.2 Synthesis of heterostructured nanorods

Although bulk $CdSe$ can take on cubic as well as hexagonal crystal structure, one can find that $CdSe$-NCs synthesised following the earlier described route form in a hexagonal crystal structure, the so called wurtzite structure. In figure 2.12 a perfect wurtzite NC

is depicted. The wurtzite crystal structure in figure 2.12 is a close-packing of the Se^{2-}

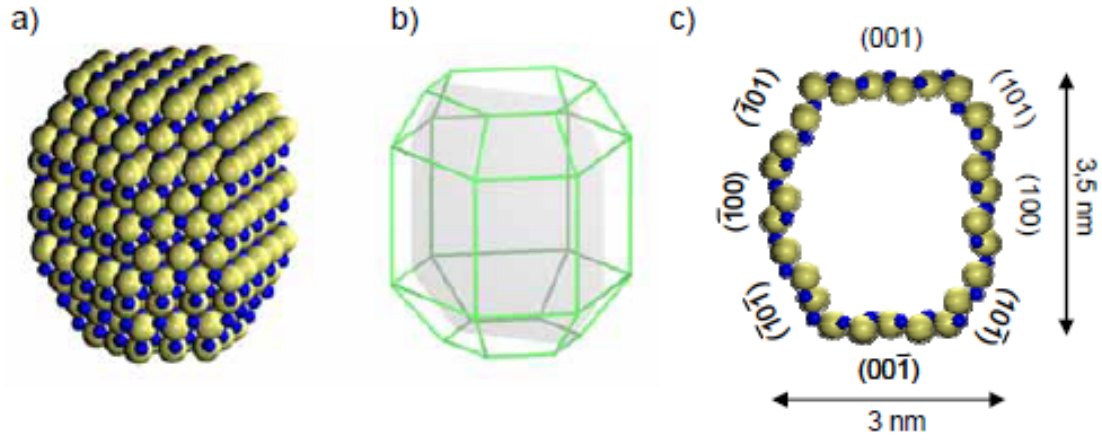

FIGURE 2.12: A perfect embodiment of a wurtzide nano crystal is shown with: a) the atomic arrangement (yellow = Sulphur, blue = Cadmium) and b) the crystal facets. In c) a cross section along the grey plane in b) is shown with the respective Miller indices.

anions (yellow spheres) in ABAB-sequence that is intertwined with the same close-packing of the Cd^{2+} cations (blue spheres). The Cd and Se atoms in the wurtzite structure both have a coordination number of 4 and hence each atom is binding to its four neighbours in a tetrahedron like orientation. Because of the orientational ABAB-stacking the wurtzite NC has a slightly prolate form. The bigger the NC the more elongated along the $\hat{c}$-axis it becomes and so the aspect ratio (AR) can vary from unity to about 1.5 for large ($\approx$ 20 nm) NCs. Figure 2.12c shows a cross section through the wurtzite crystal (the position of which can be seen in 2.12b in light blue) and the respective orientations of the surface planes are denoted using their Miller indices. The $\{001\}$ and $\{00\bar{1}\}$ planes finish with a homo-atomic layer of either Se or Cd. Therefore these facets are charged and possess many dangling bonds (3 dangling bonds and free charges per atom due to the tetrahedron like bonds). The perpendicular $\{100\}$ and $\{\bar{1}00\}$ facets are hetero-atomic and have less dangling bonds and free charges. To counteract this imbalance the $\{101\}$ planes form.

The different surface structures of the NC facets can be used to increase the asymmetry of the NC. The chemical reactivity of the facets is highly dependent on the species of surface ligand used. Using *TOPO* as surface ligand especially stabilises the dangling bonds of Cd-atoms by binding with the Oxygen. This makes the Se terminated $(00\bar{1})$ plane relatively more reactive and opens the path for asymmetric growth along this

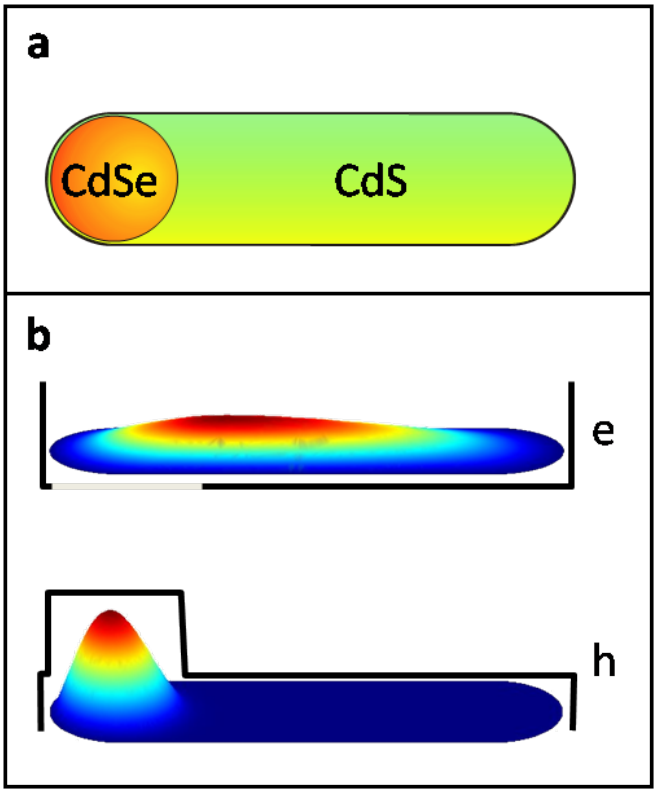

FIGURE 2.13: A schematic drawing of the material composition of heterostructured $CdSe/CdS$-core/shell NR is shown together with a representation of the electron and hole wave functions inside the nano structure.

direction. This can further be enforced by keeping the growth in the size focusing regime by constantly adding monomers to keep their concentration high. Following this procedure $CdSe$-NR of very high aspect ratios can be synthesised.

A similar method can be used to grow heterostructured NR, which are elongated core-shell NC that provide 0-dimensional confinement for the hole whereas the electron wave function can spread over the whole length of the particle (see figure 2.13). The starting point here is as before a colloid of $CdSe$-NCs (as seen in figure 2.12) with a very narrow size dispersion ($\approx 4\% - 7\%$ standard deviation) [88]. By precipitation the NCs are separated from the growth solution and possible remaining monomers. After redispersion in a clean solvent and heating to a relatively low temperature ($\approx 130°C$) a stock solution of $Cd(CH_3)_2$ and $TOP - S$ in the ratio of about $Cd/S = 1:3 - 1:5$ is added. This promotes an asymmetric growth of a CdS shell around the $CdSe$ core along the crystal $\hat{c}$-axis. In 2.14 one can see a TEM image of so-prepared NRs of different AR (up to $AR = 4.1$). Because of the very similar lattice constant of the two different crystalline

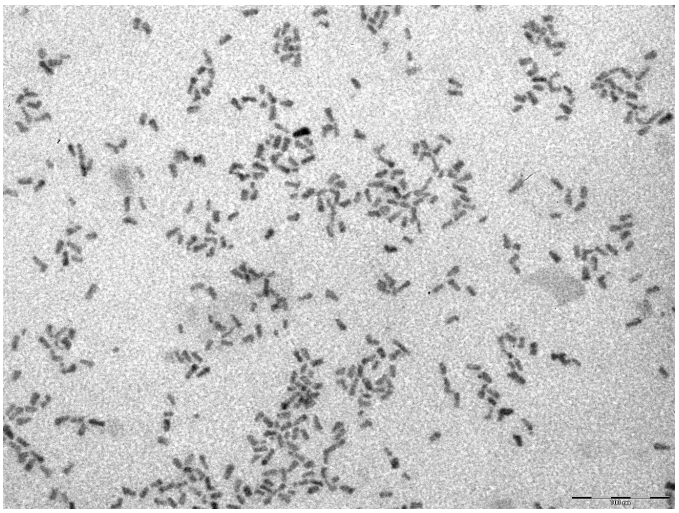

FIGURE 2.14: A low resolution TEM image of the investigated $CdSe/CdS$-NRs, some of which show a higher contrast where the $CdSe$-core is situated. The scale bar indicates a length of 100 nm.

species $CdSe$ and CdS it is difficult to make out the $CdSe$ core in such a low resolution TEM image. It is only visible for some of the NR in the image as a dark shade located at one end of the particle. The asymmetric growth is influenced by three parameters. Firstly an excess of the Sulphur precursor is necessary because it preferentially binds to Cd sites and hence promotes asymmetric shell nucleation on the $(00\bar{1})$ facet. Additionally the mismatch in the lattice constant between the $CdSe$ and the CdS is different along the $\hat{c}$-axis (001) ($\approx 4.2\%$) than along the perpendicular (100) direction ($\approx 3.8\%$). This puts a higher strain on the planes parallel to the $\hat{c}$-axis and therefore favours the shell growth along the $\hat{c}$-axis. Finally it is necessary to keep the colloid at a relatively low temperature during the shell growth in order for the thermal energy not to outperform the lattice strain and the chemical reactivity that promote the asymmetric growth.

Chapter 3

Methodology

The following sections 3.1 and 3.2 are dedicated to the description of the scientific methods used. At first we explain the laboratory setup that was used to perform the time resolved spectroscopic experiments. There we discuss in more detail the laser system and the time-correlated-single-photon-counting (TCSPC) system that we used to record the NC decay data. In the later subchapter we cover the theoretical model and the computational method used to calculate the energy levels in the investigated heterostructured NR.

3.1 Experimental methods

In order to perform ultrafast spectroscopic measurements the colloidal NCs described in 2 were either drop cast on InGaN-QW or dispersed in a polymeric matrix. For this purpose a $30\frac{mg}{ml}$ Polystyrene (PS) in Chloroform solution was prepared with which the colloid was mixed. Generally we used a dilution of 1 : 10 colloid to PS-solution. This mixture was then spin coated at 1000 rpm on a pretreated substrate. In figure 3.1 a top view (left) and a cross section (right) through a typical sample used in this work is shown. These samples were designed to be able to apply an electric field to the heterostructured $CdSe/CdS$-NRs dispersed in the PS-matrix. Square glass substrates (1.8 cm length) with an Indium tin oxide (ITO) layer of $\approx$ 200 nm thickness were purchased. The ITO was etched away on the sides of the substrate using Hydrochloric acid to leave a

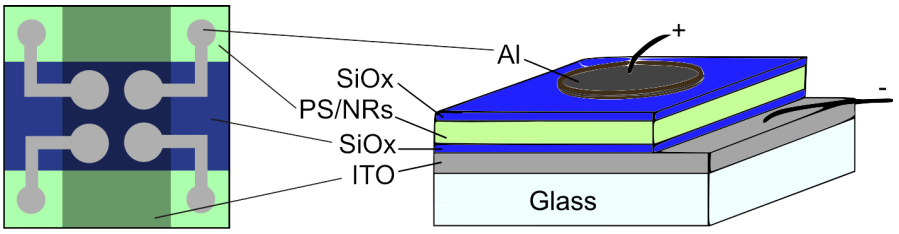

FIGURE 3.1: A drawing of the capacitor sample structure is displayed. An insulating Silica layer is deposited on a glass substrate with an ITO base electrode. On top of that the $CdSe/CdS$-NRs dispersed in a PS matrix are spin coated. The Ag top electrode is separated from that by another insulating silica layer.

1 cm wide area in the middle of the substrate (see figure 3.1). Then the substrates were cleaned from any organic residues to obtain optical grade substrates. On these substrates a ≈ 20 nm thick layer of Silicon dioxide SiO_2 was evaporated perpendicular to the ITO stripe using an electron beam evaporator. Then the sample was transferred

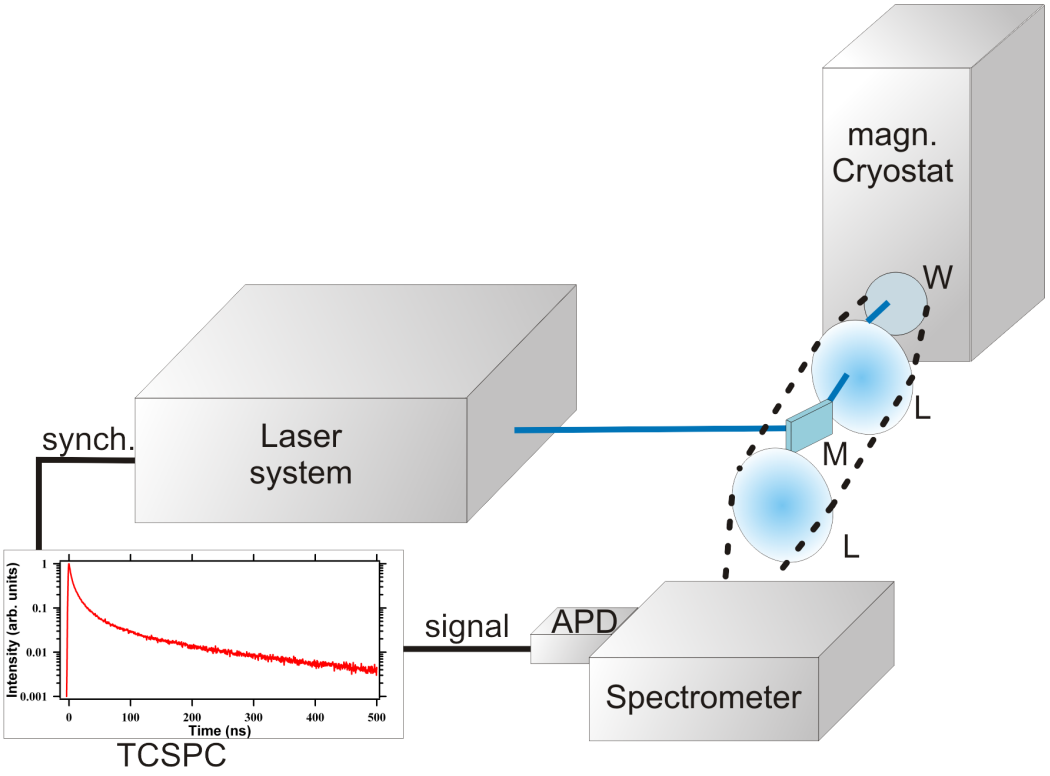

FIGURE 3.2: The time resolved spectroscopic setup is schematically displayed. A mirror (M) is used to direct the exciting laser beam onto the sample and lenses (L) are used in the detection path to collect the NR luminescence through the cryostat window (W). Single photons are detected by an Avalanche Photo Diode (APD) after energy selection through a spectrometer.

onto a spin coater to deposit a $\approx 200 - 300$ nm thick layer of the NRs dispersed in a

PS matrix. After that another layer of SiO_2 of the same thickness was deposited on the sample. The two SiO_2 layers provide electrical insulation for the sandwiched NR layer. To complete the capacitor structure 4 silver electrodes were evaporated on top of the sample.

The sample then was mounted on the sample rod of a *Spectromag* magnetic cryostat from Oxford Instruments where it was immersed in liquid Helium. The split coil design of the magnet allowed for optical access to the sample from two perpendicular directions. Like this it was possible to probe with two different magnetic field (B-field) orientations, the Faraday geometry (B-field parallel to the direction of detection) or the Voigt geometry (B-field perpendicular to the direction of detection). By implementing polarisation elements in the detection path we could investigate the B-field effect on the NR fluorescence decay depending on the relative orientation of B-field to NR $\hat{c}$-axis.

The NR were optically excited using an ultrafast regenerative amplifier system from Coherent, Inc.

3.1.1 Laser system

The laser system used for our work is sketched in figure 3.3. The synchronisation of the whole laser system is provided by the ultrafast optical Titanium:Sapphire (*Ti:Sa*) oscillator (Vitesse^{TM}). The Vitesse^{TM}has an integrated diode pumped solid state (DPSS)

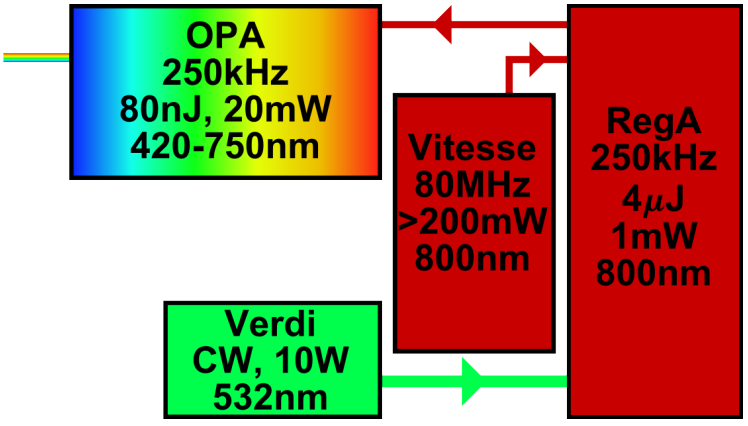

FIGURE 3.3: The laser system used for NR spectroscopy is depicted. A diode pumped solid state Verdi^{TM}pumps a Regenerative Amplifier (RegA) that is seeded by an optical oscillator (Vitesse^{TM}). An optical parametric amplifier (OPA) was used to create a given wavelength of laser emission.

pump laser (Verdi^{TM}V2) that provides up to 2 W intensity at 532 nm. This continuous wave (CW) laser has two diode slabs that provide high intensity laser light at $\approx$ 808 nm. This light is fed into the Verdi^{TM}laser cavity to pump the Neodymium Vanadate ($Nd:YVO_4$) crystal used as the solid state gain medium. The Verdi^{TM}cavity comprises as well of a Lithium triborate (LiB_3O_5, LBO) crystal that has a very high second order susceptibility and is used for second harmonic generation (SHG) which converts the 1064 nm laser light of the Neodymium Vanadate into 532 nm green laser light. The LBO crystal is birefringent and it is kept at a constant temperature of $\sim 150°C$ to match the refractive index of the fundamental and the second harmonic.

The light from the pump laser is fed into the Vitesse^{TM}cavity whose gain medium is a *Ti:Sa* crystal. Without any distortion the Vitesse^{TM}cavity will produce only CW laser light. The gain medium has an intensity dependent refractive index (optical Kerr effect) and the laser light at the centre of the beam experiences a higher refractive index than the light on the periphery of the beam profile. At high enough intensities a graded index lens is formed in the *Ti:Sa* crystal and the laser beam is focused by passing through the crystal. However in undistorted CW operation high enough intensities are not reached. To allow Kerr lensing to occur a "starter" is introduced in the cavity that distorts the laser beam and produces peaks in the light intensity. To separate the intensity peaks focused down by the optical Kerr effect from the remaining CW laser light a slit is introduced after the *Ti:Sa* crystal that blocks (see figure 3.4) the CW sides of the beam profile and lets the distorted part of the light pass. As this intensity peak of the laser light travels through the cavity over and over again more and more intensity builds up and finally only one laser pulse travels through the cavity that takes away all the stimulated emission each time it passes the *Ti:Sa* crystal. For ultrafast spectroscopy this pulse needs to be as short in time as possible and therefore group velocity dispersion needs to be counteracted. Four negative dispersion mirrors in the

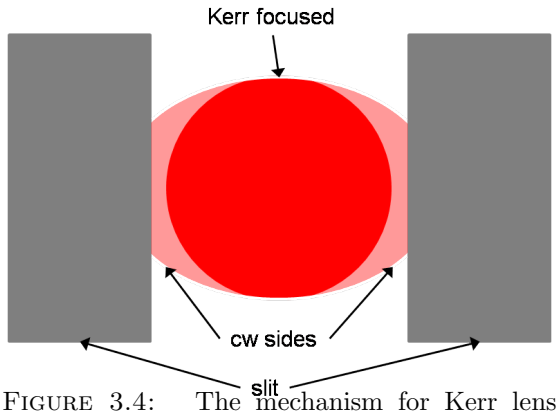

FIGURE 3.4: The mechanism for Kerr lens mode locking is drawn schematically. A slit is used to block the cw-component of the laser beam and therefore amplifies the temporally distorted part of the beam.

Vitesse^{TM}cavity provide for sufficient compensation and pulse durations of less than 100 fs at a repetition rate of 80 MHz can be achieved.

The Vitesse^{TM}pulse train is used to seed the regenerative amplifier (RegA) which itself is pumped by another Verdi with 10 W output. Contrary to the passive Kerr lens mode locking of the Vitesse^{TM}the RegA is actively mode locked using two acousto-optic modulators (AOM). One of the AOM, the so called Q-switch is used to deflect the beam path away from the ideal cavity and therefore it keeps the cavity below lasing threshold. During this time when the cavity is of low 'quality' the whole power from the pump laser can be stored in the *Ti:Sa* gain medium. The second AOM is called the cavity dumper. It is used to insert one pulse from the Vitesse^{TM}pulse train synchronised with the Q-switch modulation of the cavity. This happens when the cavity is brought into the lasing regime by the Q-switch and hence the inserted pulse can harvest all of the stored energy within ≈ 25 round trips in the cavity. The Q-switch also acts as a highly dispersive medium and lengthens the pulse considerably to avoid thermal damage in the gain medium and to increase the amplification. When the pulse in the cavity reaches its maximum amplification the cavity dumper is used again to couple it out. In order to still be usable for ultrafast spectroscopy the pulse however needs to be re-compressed after the strong dispersion induced by the Q-switch. This is provided for by a 4 path grating compressor. This recompresses the pulse to less than 200 fs by providing longer optical paths for the leading edge of the pulse then for the trailing edge. The parameters for a typical RegA pulse train can be seen in figure 3.3.

Because the *Ti:Sa* gain medium in the RegA lases at 800 nm we need to convert this light to lower wavelength to be absorbed by the investigated NRs (absorption for wavelengths less than 550 nm). To do this the RegA pulse train is fed into an Optical Parametric Amplifier (OPA) which uses two non linear crystals to produce laser wavelengths from 420 nm up to 750 nm. One of the nonlinear optical elements in the OPA is simply used for SHG and for the experiments presented in this work we always used this 400 nm laser light to excite the investigated NR.

3.1.2 Time correlated single photon counting

The method of TCSPC was used to record fluorescence decay curves for decays of up to 2 μs duration from the $CdSe/CdS$ NRs. For this purpose an SPC140 photon counting card from Becker&Hickl, a DG535 delay generator from Stanford Research and an avalanche photodiode (PDM from Micro Photonic Devices) have been purchased.
The measurement principle of TCSPC is to detect the time difference between a signal pulse and a reference pulse. This time difference is then digitised and a histogram of arrival times created. The TCSPC card we used has two inputs, one for the signal that starts the measurement and one for the reference from the laser pulse train that is used to stop the measurement. The signal pulse is created when a single photon hits the active area of the avalanche photodiode. The signal pulse can vary significantly in amplitude depending on the kind of detector used. In figure 3.5 the architecture of a classical TCSPC device using 'reversed start-stop', where the signal is used to start a measurement and the constant pulse train to stop the measurement, is shown. Exact triggering

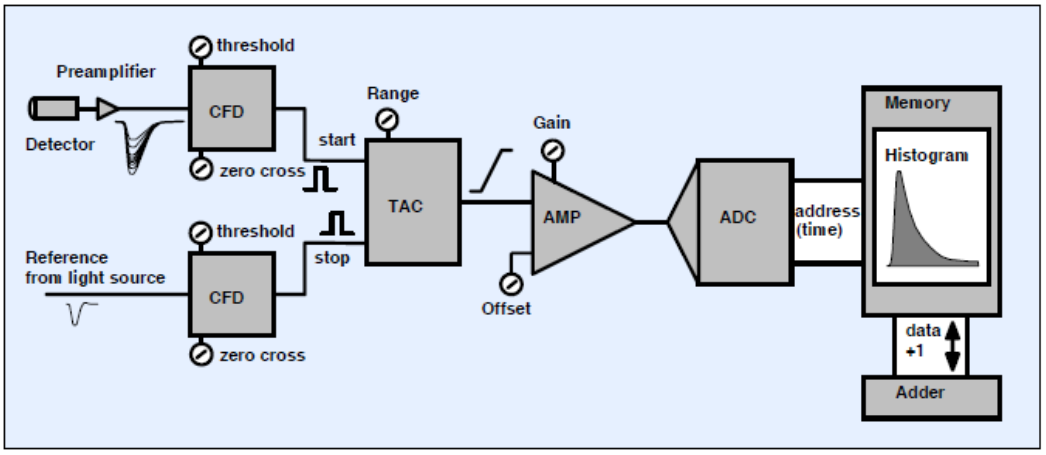

FIGURE 3.5: A schematic representation of the TCSPC method is shown. Start and stop signal from the detector and the laser source respectively are processed in constant fraction discriminators (CFD) and fed to a time to amplitude converter (TAC). Using an amplifier (AMP) and an analog to digital converter (ADC) the signal is further processed and written to the local memory from which it can be displayed in real time.

on the signal and reference pulses is crucial for the accuracy of TCSPC measurements. Leading edge triggering is not sufficient to achieve that and therefore constant fraction discrimination (CFD) is used for both inputs. For CFD a divider is used to produce a copy of the input pulse. This copy is electrically delayed compared to the input pulse

and then these two pulses are subtracted from each other. This eliminates the variation of leading edge arrival time and creates a zero level crossing that is stable in time (see figure 3.6).

After the signal leaves the CFD as a square pulse and is delivered to the time to

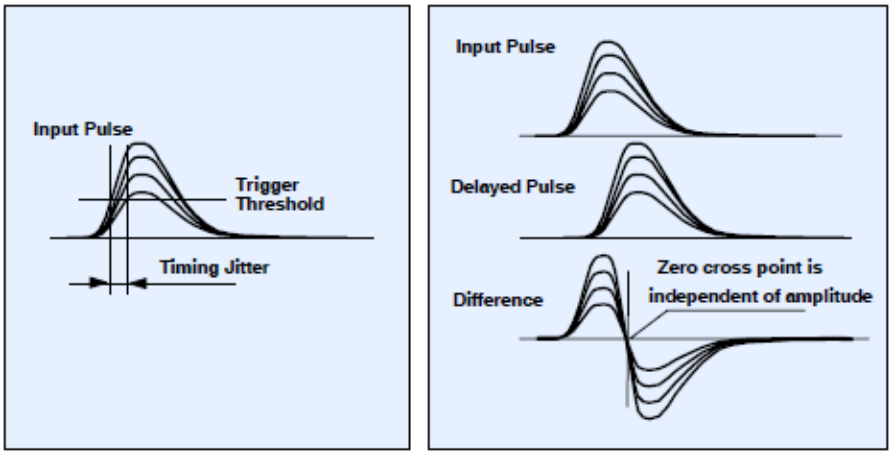

FIGURE 3.6: The principle of a CFD is displayed that allows one to accomodate for different signal amplitudes. The incoming signal is divided into two signals one of which goes through a delay line. The delayed signal is then subtracted from the first signal. The such determined zero amplitude crossing is stable in time independent of signal amplitude variations.

amplitude converter (TAC). The TAC generates an output voltage that is proportional to the time between signal (start) and reference (stop) pulse. When the start pulse arrives a current source is connected to a capacitor and upon arrival of the stop pulse the charging is interrupted. The circuitry of the TCSPC board allows one to correct for the nonlinearities that occur when starting and ending the charging process. The conversion accuracy of this process is in the range of a few picoseconds. Furthermore it is possible to change the slope of the charging ramp to accommodate for a range of detection windows from several nanoseconds up to $2\mu s$. The TAC remains charged until the next signal arrives.

After the TAC, the signal is fed into an amplifier (AMP) with variable gain and offset. The AMP is used to select a shorter time window out of the full conversion range of the TAC. When using a low repetition rate system to trigger very fast processes this principle can be used in order not to loose time resolution.

The analogue to digital converter (ADC) finally digitises the continuously distributed arrival times and addresses them to one of 4096 output channels. Therefore the final

resolution Δt of the measurement is dictated by the length of the detection window T following the equation $\Delta t = T/4096$.

3.2 Theoretical methods

In order to complement the experimental data we used computational methods to calculate wave functions, energy levels and level populations in the investigated colloidal NRs. For the numerical computation we used *FemLab*®, now known as *COMSOL Multiphysics*®, and the program *MATLAB*®. This chapter is devoted to explain the numerical algorithm used and to introduce the finite element method used in FemLab®.

3.2.1 Extended effective mass approximation

In this chapter we discuss an extension of the effective mass approximation 2.1.1.2 discussed earlier. In the following we take the Coulomb potential between electron and hole into account when calculating their wave functions and energy eigenstates.
Although the NRs investigated in this work provide strong confinement of charge carriers, it was shown earlier [18] that spherical NCs of the same diameter show a Coulomb interaction that makes up $\sim 20\%$ of the total exciton energy. For a quantitative comparison between theory and experiment we cannot neglect the Coulomb potential. Starting with the Schrödinger equation one can calculate the exciton energy using an iterative, self-consistent Hartree-Fock method even when the Coulomb interaction is taken into account. The solution of the iterative method using a finite element method allows us to investigate any given geometry. For spherical NC this algorithm has already been applied in a similar fashion earlier [89; 90].
The complete Hamiltonian for an exciton in a NC:

$$H = -\frac{\hbar^2}{2m_e^2}\nabla^2 e - \frac{\hbar^2}{2m_h^2}\nabla^2 h + V_e(\vec{r}_e) + V_h(\vec{r}_h) - \frac{e^2}{4\pi\epsilon\epsilon_0\left|\vec{r}_e - \vec{r}_h\right|} \tag{3.1}$$

consists of separate kinetic and potential ($V_{e,h}(\vec{r}_{e,h})$) terms for electron and hole and the Coulomb potential coupling the two charge carriers. Given that the Coulomb interaction

is small compared to the quantisation energy, so that the wave function for both carriers is dictated mainly by the confinement potential and the geometry of the NC, then one can express the Coulomb attraction that one carrier exerts upon the other as an effective potential. This allows to separate the Hamiltonian 3.1 into the following two decoupled Hamiltonians [91]:

$$H_e = -\frac{\hbar^2}{2m_e^2}\nabla^2 e + V_e(\vec{r}_e) + V_{h,eff}(\vec{r}_e) \tag{3.2}$$

$$H_h = -\frac{\hbar^2}{2m_h^2}\nabla^2 h + V_h(\vec{r}_h) + V_{e,eff}(\vec{r}_h). \tag{3.3}$$

The effective potentials $V_{e/h,eff}$ in equations 3.2, 3.3 are the solutions of the Poisson equation. The charge distribution that is needed to solve the Poisson equation on the other hand is taken from the probability distribution for the charge carriers given by the wave functions:

$$\Delta V_{e/h,eff}(\vec{r}) = -\frac{\rho_{e/h}(\vec{r})}{\epsilon\epsilon_0} = -\frac{\mp e \cdot (\Psi_{e/h}(\vec{r}))^2}{\epsilon\epsilon_0}. \tag{3.4}$$

In figure 3.7 a schematic of the iteration process to solve the separated equations is shown. Because of the strong localisation of the hole within the $CdSe$ core its wave function is less influenced by the presence of the electron than vice versa. For this

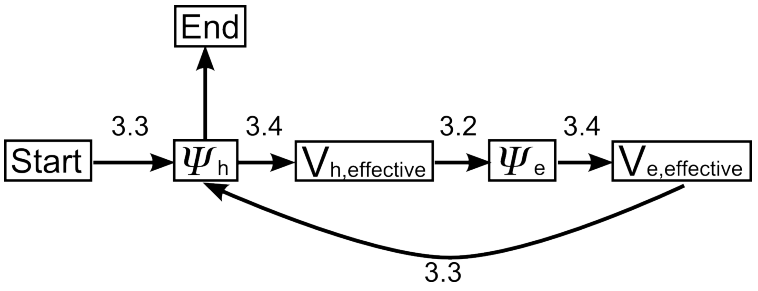

FIGURE 3.7: A flowchart representation of the iteration process pursued in the numerical calculations is shown.

reason the iteration starts with equation 3.3 and the effective potential that the electron exerts on the hole is set to zero. In the next step we calculate the Coulomb potential for the hole (equation 3.4) with the resulting unperturbed wave function of the hole from the earlier calculation. Using this potential we calculate the wave function for the electron using equation 3.2. In the same way as for the hole we can then calculate the electrostatic potential for the electron using equation 3.4. This potential is then entered into equation 3.3 and the next iteration starts by calculating the hole wave function with

$V_{e,eff}$ from the prior step.

This algorithm has been implemented in FemLab® 3.1 using MATLAB® to control the iterations and to extract the wave functions for further processing. Because of the cylindrical symmetry of the problem we could transform equations 3.2 to 3.4 into cylindrical coordinates for faster calculation.

3.2.2 Finite element method

A complete mathematical description of all applied mathematical methods and approximations goes beyond the scope of this work. Therefore the concept of the finite element method is roughly described and we will give an overview of the approximations used. For the implementation of the problem we chose FemLab® which uses the finite element method to solve the problem, employing the numerical algorithm described in 3.2.1.

The finite element method is a powerful numerical technique to solve differential equations or even integrals. It allows for the investigation of arbitrary geometries and assemblies of materials. The general working principle of the finite element method can be broken down into the following steps:

1. The first step in the finite element method is to identify the differential equations governing the system. In our case these are the two Schrödinger equations with

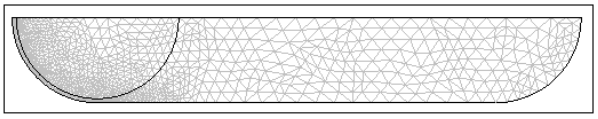

FIGURE 3.8: The meshing of the NR structure used in Femlab is shown. Because of the cylindrical symmetry only the cross section through half of an NR is used in the program. The mesh is more dense around areas where material constants change in order to achieve a highly accurate result and keep calculation time low.

   the Hamiltonians for electron 3.2 and hole 3.3 and two Poisson equations 3.4, again one describing the electron and one the hole.

2. One has then to choose the method of numerical integration. We used the well documented Runge-Kutta method [92] for this purpose.

3. In the next step the geometry object over which the differential equations will be solved needs to be defined. As an approximation we regard the investigated NR as cylinders with a half sphere attached to each end. Within this cylindrical geometry we define a sphere located on one end of the cylinder as the $CdSe$ core. It has been measured using high resolution tunneling electron microscopy that the CdS shell covers the core completely. On the core proximal end of the NR the $CdSe$ is overgrown with a thin layer of CdS. The thickness of this layer scales with the AR [93]. For the sake of computing time we take advantage of the cylindrical symmetry and solve the problem only on a semi cross section along the length of the cylinder.

4. For the well defined geometry objects one then has to define the material constants. In order to solve the Schrödinger and Poisson equations we inserted the values of ΔB (the difference of the band gaps of the two materials), the values for $m_{\{e,h\},eff}$ (the effective masses for electron and hole) for the two materials and the necessary physical constants in the program.

5. In the following step a discretisation of the geometry object is introduced. Therefore the geometry object is divided into an arbitrary mesh of simple geometrical shapes (see figure 3.8). In FemLab® the meshing is produced using triangles.

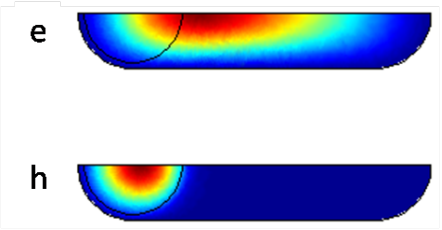

FIGURE 3.9: The electron and hole wave functions are shown as calculated by Femlab. The NR used has a radius of $2nm$ and an aspect ratio of 3.6.

The degree of mesh resolution of this meshing can be varied over the geometry objects. In areas of strong variation of the wave functions the meshing needs to be finer than in areas where the wave functions are not expected to vary very much. After the meshing an appropriate approximation of the field variable (the wave function in our case) over the mesh elements needs to be introduced: e.g.

$\phi(\vec{x}) = N_1(\vec{x})\phi_1 + N_2(\vec{x})\phi_2 + N_3(\vec{x})\phi_3$ with ϕ_i being the nodal values of the field variable and N_i being interpolation functions.

6. In the final step the actual wave functions for electron and hole (see figure 3.9) are calculated and written in the FemLab® data structure.

A more detailed description of the algorithm and the script we used can be found in appendix A and in appendix B we will discuss the addition of an external electric field into the numerical calculation using the extended effective mass approximation.

Chapter 4

Anisotropic magnetic field effects

The outstanding optical properties combined with the easy and versatile method of synthesis of colloidal NCs open up a wide field of possible applications spanning from NC-lasers [94], through energy harvesting in photovoltaic devices [95; 36], to fluorescent labelling [96]. Colloidal NCs are nearly spherical and hence when transferred from the colloidal dispersion onto a substrate the individual NCs will arrange isotropically with randomly oriented symmetry axes. For this reason, it is difficult to utilise the intrinsic polarisation state of the exciton in colloidal NC. The synthesis of elongated nano-structured particles (nanorods) however allowed control of the relative orientation of the emitters by using self assembly [97], polymer [41] or liquid crystal alignment [98]. The microscopic nature of the emitting state and its polarisation however are often not clear and require investigation of the exciton fine structure.

In the current chapter we present a comprehensive investigation of the exciton fine structure of heterostructured colloidal NRs (see chapter 2.1.2.4). Using finite element calculations of the electron and hole wave functions combined with analytical formulae of the exciton fine structure in spherical wurtzite NCs [42] we determine the exciton fine structure of heterostructured $CdSe/CdS$-NRs. Then we introduce the magnetic field effects observed in the NR spectra and fluorescence decay curves. Furthermore we show the dependence of the NR fluorescence decay on the relative orientation of the emitting state within the magnetic field. We show experimental evidence of the angular dependence of the Zeeman splitting in wurtzite NCs for the first time.

4.1 Exciton fine structure

Analytical formulae for the exciton fine structure in spherical wurtzite $CdSe$-NCs can be derived (see equations 2.28) by using first order approximations for the shape asymmetry, the crystal field splitting and the electron hole exchange interaction. For nanorods of high aspect ratio (AR) however these formulae cannot be used because the assumption of a spherical symmetry of the hole wave function can not be upheld. The heterostructured NR investigated in this work however represent a hybrid system between a spherical $CdSe$ core NC and a high AR CdS NR. In figure 2.13a we gave a graphical depiction of the microscopical structure of heterostructured $CdSe/CdS$ NR. The shown NR has an AR of 3.6. On the left side the spherical $CdSe$ core can be seen on which the elongated asymmetric CdS shell is grown epitaxially. The numerically calculated (see chapter 3.2.2 for a description of the finite element method used) wave functions of electron and hole are displayed in figure 2.13b. The conduction band transition from $CdSe$ to CdS is flat [54] and therefore the electron wave function can spread over the whole length of the NR. The hole wave function however is confined to the $CdSe$ core because of a valence band offset of $\Delta E = 0.78eV$ between the two materials [99; 54]. The electrostatic interaction between the electron and hole prevents the electron wave function from stretching symmetrically along the NR length. In figure 2.13 it can be seen that the electron wave function's symmetry is broken and that it is inclined towards the $CdSe$ core in which the hole wave function is confined. The low temperature synthesis of the investigated NRs [41] prevents an alloying of $CdSe$ and CdS at the core/shell interface and provides for the strong spherical confinement of the hole. Because of this we can use the analytical expressions from equation 2.28 to calculate the exciton fine structure in said heterostructured $CdSe/CdS$ NRs.

However in order to calculate the contribution of the electron/hole exchange interaction $\eta = \alpha \int (\psi^*_{s_z})^2(\vec{r}_e)\psi^2_M(\vec{r}_h)d\vec{r}$ the wave function overlap for the two carriers is needed. In addition to that $E_{3/2}(\beta)$ the ground state energy of the $1S_{3/2}$ hole state is required to calculate the shape asymmetry splitting induced by the not perfectly spherical $CdSe$ core. The different confinement regimes of electron and hole and the finite energy barrier between the $CdSe$ core and the CdS shell require us to resort to numerical methods

for these tasks (see chapter 3.2.2). To test the viability of our semi-numerical approach

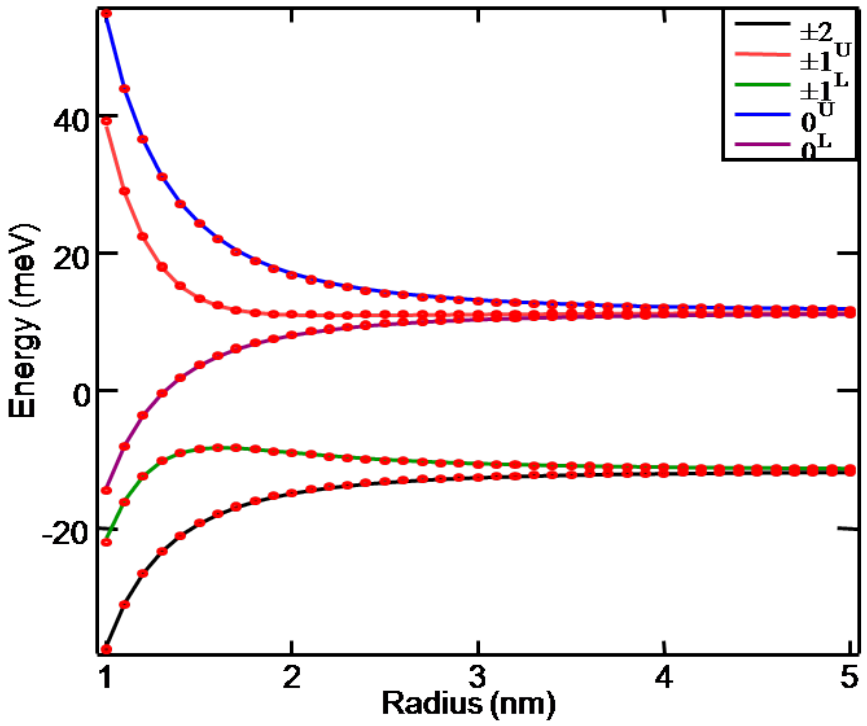

FIGURE 4.1: A comparison between the analytical solution (continuous line) and our semi-numerical model (dots) is shown for the exciton fine structure of spherical $CdSe/CdS$-NC.

we calculated the exciton fine structure of spherical $CdSe$ NC and compared it with the analytical result as attained by Efros et al. [42] in order to validate the model. In figure 4.1 the analytical result is plotted as continuous lines against the NC radius. The individual excitonic levels are labeled by their total angular momentum projection $|F|$. At very large radii the influence of the shape asymmetry splitting and the exchange interaction becomes very small and the manifold of excitonic levels merges to two 4-fold degenerate exciton states that are separated by the crystal field splitting $\Delta_{cr} = 25meV$. In addition we display the numerically obtained values in figure 4.1 as red open dots against the NC radius. The agreement between the analytical and the numerical calculations is very good and for this reason we will use the numerical approach to calculate the exciton fine structure for heterostructured NRs.

The theoretical treatment of spherical NCs by Efros et al. [42] focuses on core NCs that consist of one single material. For quantum efficiency and stability [28; 29] reasons however these core NC have widely been replaced by core/shell NC where a second higher

band-gap material is epitaxially grown onto the so-called core. In this core/shell case

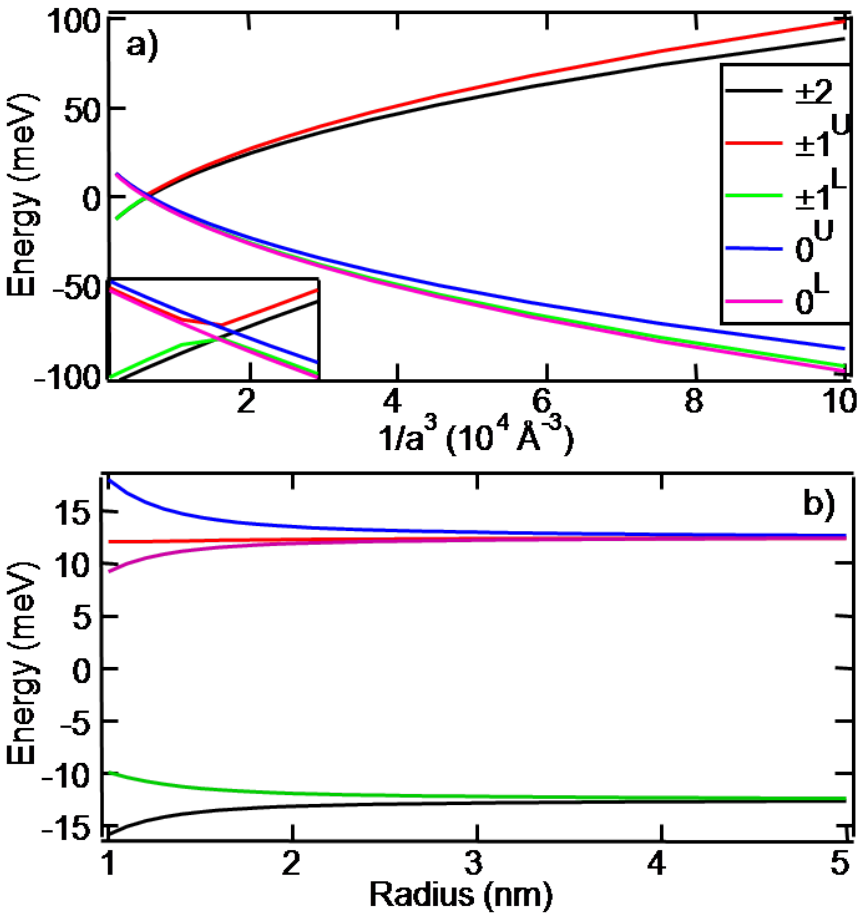

FIGURE 4.2: The results of the excitonic fine structure for a) a $CdSe$-NR and b) a heterostructured $CdSe/CdS$-NR using the semi-numerical method.

the carrier wave functions are not confined by an infinite potential barrier but rather by the finite potential step between the valence ΔE_v or conduction ΔE_c band levels of the two materials. Depending on the respective differences in energy, the carrier wave functions can leak into the shell material as well. Therefore the carrier confinement as well as the wave function overlap are different to the core NC case. This affects the exciton energy fine structure, however only for small NC radii where the part of the carrier wave function leaking from the core into the surrounding shell material is not a negligible proportion of the total carrier wave function.

As in the case of spherical NCs the same material composition (simple core and core/shell) can be synthesised in the form of nanorods as well. Wurtzite semiconductor NRs are elongated along the $\hat{c}$-axis of the crystal lattice and can achieve very high aspect ratios

of greater than 20 : 1 [100]. The semi-analytical method for calculating the exciton fine structure in NCs however breaks down in the case of simple core NR. This is because the spherical approximation of the hole wave function cannot be maintained.

In figure 4.2a we show the results of our semi-analytical calculation of the exciton fine structure of bare $CdSe$-NR with an aspect ratio of 3.5 with respect to the inverse volume of a NC of equivalent radius. This relation has been chosen to make it easier to compare the results to earlier literature [101]. For reasons of clarity we show the level-crossing blown up in an inset. At high radii $> 3.5\ nm$ the numerical evaluation of the hole energy and the electron hole wave function overlap becomes divergent and no results could be obtained. But already the results for the exciton fine structure shown in figure 4.2 are not correct because of the non-spherical shape of the hole wave function and comparison with Le Thomas et al. [101] shows this. Nevertheless the energy fine structure does qualitatively reproduce the result for elongated $CdSe$-NC as shown by Efros et al. [42]. This can be seen in particular in the inset where the $|\pm 2\rangle$ and the $\left|0^L\right\rangle$ level are crossing at a radius of 2.5 nm. For the whole range of radii the lowest exciton level is optically passive. In figure 4.2b we show the exciton fine structure for a heterostructured NR whose microscopic structure can be seen in figure 2.13. For this species of nanocrystal the semi analytical approach described earlier is fully justified because of the strong spherical confinement of the hole wave function in the $CdSe$ core [54]. The order of the individual fine structure levels in figure 4.2b is the same as in the spherical core/shell-NC case (see figure 4.1). However the exciton levels vary less and their energy splitting is smaller than for the spherical case. This is due to the greatly reduced wave function overlap in the heterostructured NR where the electron wave function diffuses over the length of the NR. However for both cases the optically inactive $|\pm 2\rangle$ state is the lowest excitonic state for all considered radii. Angular momentum conservation prevents this state from decaying to the ground state by emitting a single photon of spin ± 1. The lowest excitonic state of a core $CdSe$-NC therefore possesses theoretically an infinite lifetime. Thermal energy is necessary to lift the exciton from the optically inactive ground state to the optically active $\left|\pm 1^L\right\rangle$ state. Because of an energy splitting of 3 meV for a core/shell NC of 2 nm radius thermal activation from the ground state is very weak at low temperatures. For this reason very long decay times

have been reported for these NC [102]. For heterostructured NR however this splitting for the same NR radius is only 1.2 meV which leads to a much shorter decay time of 20 ns [54]. However this short thermally activated decay is accompanied by a much

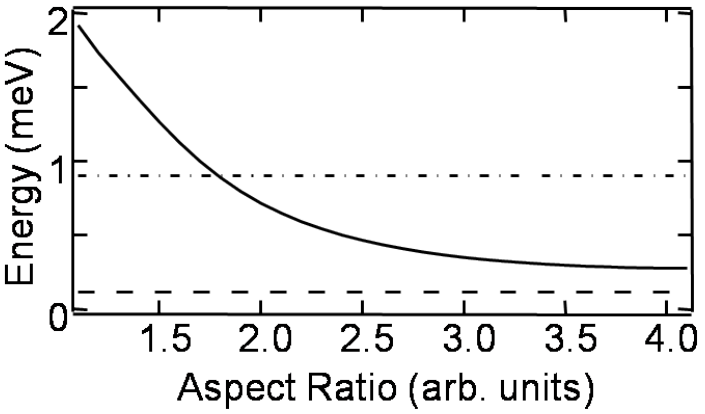

FIGURE 4.3: The short-range exchange strength vs. aspect ratio for core/shell nanorods of 4 nm diameter. The dashed and dash-dotted lines correspond to the bulk strength of the short-range exchange interaction and the long-range exchange strength respectively.

slower and weaker fluorescence transient extending over hundreds of nanoseconds that originates from the optically inert ground state [102; 42; 103]. From the excitonic fine structure we calculated for these asymmetrical $CdSe/CdS$ nanorods it is not possible to understand why close to 100% linear polarised emission [41; 101] has been shown in micro-photoluminescence measurements of single NRs, because the identified lowest optical active states will emit circular polarised light.

For symmetrical $CdSe/ZnS$-NR with high aspect ratios between 8 and 10 single particle spectra with a circular and a linear polarized component have been reported [101]. The exciton fine structure for these symmetrical NR has been calculated combining a variational calculation [104] to obtain the electron-hole pair energy and the earlier mentioned approach of invariants [42] to calculate the electron hole exchange interaction. Through this investigation it has been shown that the optically forbidden $\left|0^L\right\rangle$ ground state and the two optically allowed $\left|0^U\right\rangle$ and $|\pm 1\rangle$ states thermally mix even at low temperatures of 15 K [101]. The two active states account for the linear and circular component of the $CdSe/ZnS$-NR emission.

In the case of the asymmetric $CdSe/CdS$-NR used in our research however the active linear $\left|0^U\right\rangle$ exciton state is split by 26.7 meV from the $|\pm 2\rangle$ ground state and efficient

thermal mixing does not occur, even at room temperature. However as has been shown first in single self assembled quantum dots [105; 106; 107] and theoretically described earlier [108; 109; 110] the long range exchange interaction leads to a mixing of the $|\pm 1\rangle$ states to form two linearly and orthogonally oriented dipoles $|X, Y\rangle = (|+1\rangle \pm |-1\rangle)\sqrt{2}$, this has later been demonstrated in single colloidal $CdSe/CdS$-NCs as well [47; 48]. In figure 4.3 we show the bulk value for the short range exchange interaction $\approx 0.13\ meV$ [111; 112] as dashed line and the long range value $0.9\ meV$ [112] as dashed-dotted line. In comparison we display the short range exchange interaction which we calculated in heterostructured $CdSe/CdS$-NR of 4 nm diameter for different aspect ratios in figure 4.3 as well (solid line). For nearly spherical NR the strong confinement of the electron and hole wave function enhances the short range exchange interaction strongly so that it becomes larger than the non-analytical term. However as the AR increases the electron wave function is permitted to diffuse out into the CdS shell which efficiently reduces the carrier wave function overlap and leads to a reduction of the analytical term of the exchange interaction. At aspect ratios above $AR = 2$ the long range exchange term clearly dominates over the short range exchange interaction. As the heterostructured

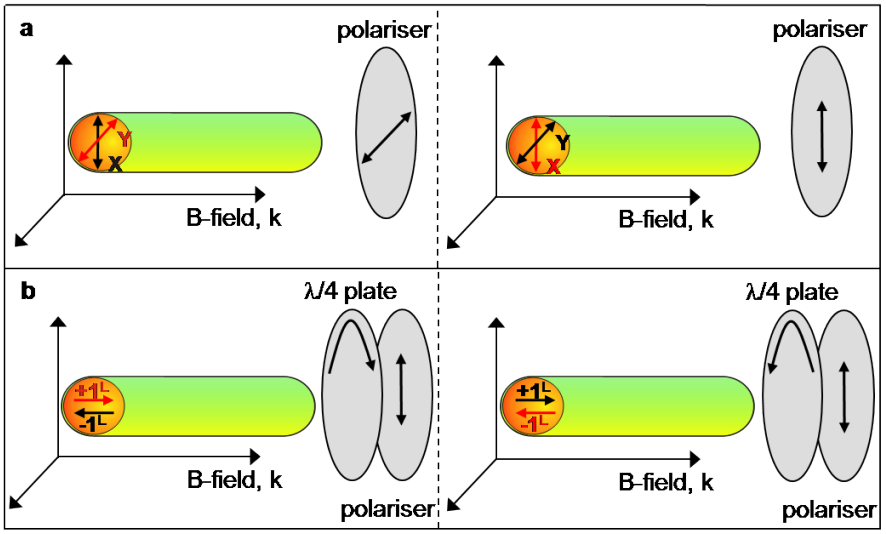

FIGURE 4.4: The detailed setups for detecting a) the linear $|X, Y\rangle$ and b) the circular exctionic polarisations in Faraday geometry are shown.

$CdSe/CdS$-NR we investigated in this work all have aspect ratios of $AR = 2.5$ and above we can ascertain that these linear mixed states are the predominant excitonic

states in all the studied samples. The two mixed states

$$|X,Y\rangle = \left(\left|+1^L\right\rangle \pm \left|-1^L\right\rangle\right)\sqrt{2} \tag{4.1}$$

are created by the long range exchange interaction in heterostructured NR that exhibit a significant asymmetry in the plane perpendicular to the $\hat{c}$-axis of the NR. The two constituent states $\left|\pm 1^L\right\rangle$ of these composite fine structure states emit left and right circular photons respectively. Hence the composite states $|X,Y\rangle$ exhibit linear polarised emission with the polarisation direction effectively perpendicular to the $\hat{c}$-axis of the NR. Other than the circular $\left|\pm 1^L\right\rangle$ states the linear composite $|X,Y\rangle$ states have therefore zero spin projection along the major $\hat{c}$-axis of the colloidal NR. In order to establish this richness of fine structure states single particle measurements with very fine spectral resolution are typically employed. However by using an optical magnetic cryostat with two perpendicular detection axes and by performing polarisation sensitive and time resolved measurements we can show that it is possible to distinguish between the single states of this manifold of optically active states even in the ensemble.

In figures 4.4 and 4.5 we show a schematic depiction of the polarisation sensitive setups

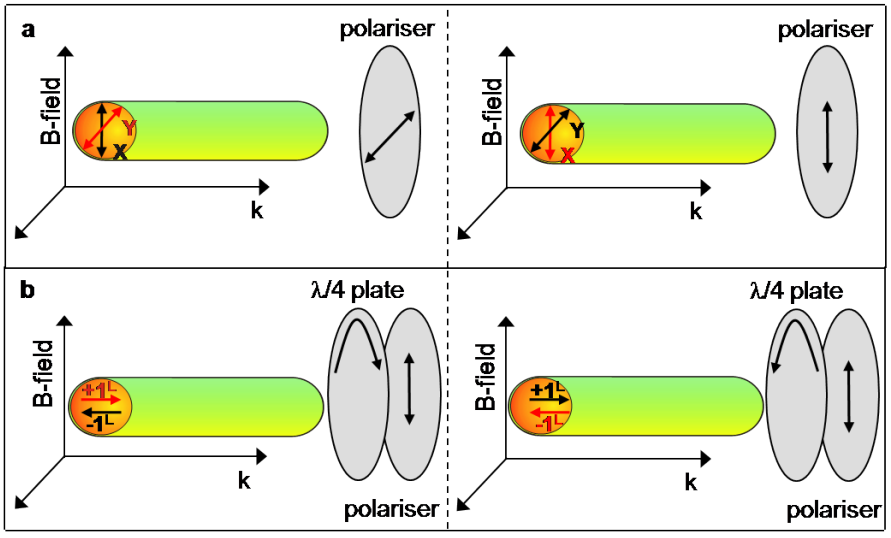

FIGURE 4.5: The detailed setups for detecting a) the linear $|X,Y\rangle$ and b) the circular exctionic polarisations in Voigt geometry are shown.

we used both for Faraday geometry (figure 4.4), where the direction of detection is parallel to the direction of the magnetic field, and for Voigt geometry (figure 4.5), where the

direction of detection and the direction of the magnetic field are perpendicular to each other. We display the orientations of the spin projections of the linear $|X, Y\rangle$ states and the circular $\left|\pm 1^L\right\rangle$ states as they would appear in an arbitrary NR within the sample. In figure 4.4a the detection scheme for the two linear states is shown in Faraday geometry and the same scheme in Voigt geometry can be seen in figure 4.5a. The circular states have been measured using a $\frac{\lambda}{4}$-plate in combination with a linear polariser and the schematic setups can be seen in figure 4.4b for Faraday geometry and in figure 4.5b for Voigt geometry.

In this section we have described a semi-numerical procedure to calculate the exciton fine structure for complicated semiconductor nanostructures like the heterostructured $CdSe/CdS$-NRs we investigated. We have proven the accuracy of this approach by comparing our results with the fully analytical solution of spherical $CdSe$-NCs and we have shown the semi-numerical solution for the colloidal NRs we studied. Furthermore we have shown that these heterostructured NR consistently have an additional linear excitonic substructure that is dependent on the asymmetry of the crystal in the plane perpendicular to its $\hat{c}$-axis. Because of the strongly reduced analytical term of the exchange interaction in these heterostructured NR these linear excitonic states $|X, Y\rangle$ are the dominant emitting states. Finally we have described a scheme that will allow us to selectively probe the different optically active excitonic states $\left|X, Y, \pm 1^L\right\rangle$ even in the ensemble.

4.2 Magnetic field effects

In this section we detail our findings of the effects of magnetic fields on the luminescence spectra, exciton dynamics and fine structure in heterostructured NRs. We furthermore introduce a quantitative measure that allows us to compare the strongly non-exponential luminescence decays of different size patches of NRs.

In figure 4.6a we show the integrated luminescence spectrum of a sample of heterostructured NRs having an aspect ratio of 3.6 and a $CdSe$-core radius of 2 nm. This sample was immersed in liquid Helium in a split coil magnet and spectra were taken at field

strengths of 0 T and 8 T. The emission of the sample at 8 T seems to be stronger than the emission without a magnetic field. However this result could not be systematically verified. The intensity signal noise due to liquid Helium bubbles inside the sample space that vary the excitation as well as the collection path ($n_{liquidHe} = 1.026$) is bigger than a possible increase of the emitted light intensity. However this signal noise does not have an effect on the time resolved spectroscopic measurements we will discuss later. The maximum length of 1 μs of the time interval we investigated and the statistical accumulation of single photon measurements eliminate the influence of variations in the boiling rate of the liquid Helium on the measured luminescence decay.

Because of the intensity variations we analyse the emission spectra rather with respect to their spectral position and width than with respect to their integrated intensity. In figure 4.6b we show the normalised spectra from figure 4.6a. All luminescence spectra have been fitted using a Gaussian and the fits are displayed over the spectra in a yellow (0 T) and a blue (8 T) dashed line. A slight spectral blue shift can be seen as the magnetic field is applied. This move to higher emission energies can be understood as a diamagnetic shift [113]. It has been shown earlier [114] that the diamagnetic coefficient in semiconductor nanostructures is proportional to the exciton size. However because the hole wavefunction extends very far into the shell of the investigated heterostructured $CdSe/CdS$-NR the diamagnetic shift of 6 meV very close to the bulk value [113] is justified. On the high energy side of the two spectra without magnetic field and with 8 T applied the Gaussian fit is very accurate and closely follows the measured spectra. In figure 4.6c we show that for the low energy flank of the emission spectra the Gaussian fit is not as good as for the high energy flank. But a fit using a Lorentz distribution very closely follows the spectra of the NR without magnetic field and with 8 T applied as can be seen in figure 4.6d. This different behaviour for the high energy side and the low energy flank of the spectrum can be explained with the different growth mechanisms for the used $CdSe$ core NCs that results from the addition of another coordinating component hexadecylamine (HDA) in addition to the conventionally used trioctylphosphine oxide-trioctylphosphine (TOPO-TOP) [88]. This additional coordinating component changes the growth dynamics of the spherical $CdSe$ core NC drastically and removes the very slow diffusive growth mechanism of Oswald ripening that depletes the small

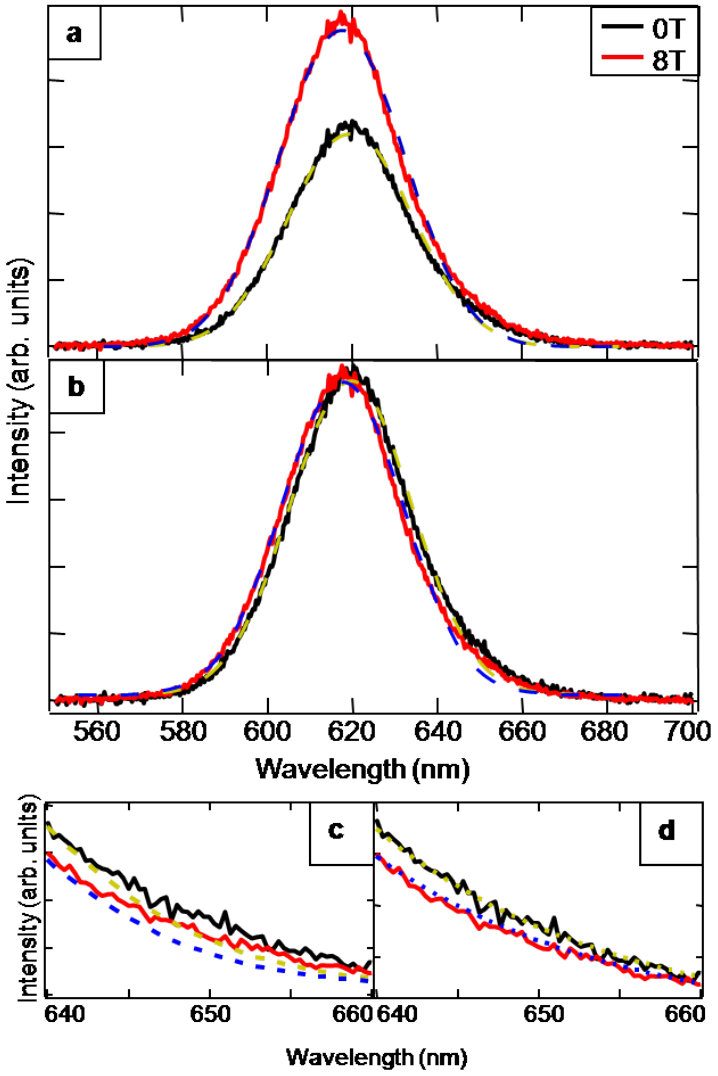

FIGURE 4.6: The spectrum of a sample of heterostructured $CdSe/CdS$-NRs is shown at zero magnetic field (black continuous line) and at $B = 8\ T$ (red continuous line) a) with the recorded intensities and b) normalised. Both spectra were fitted using a Gaussian distribution function. c) shows the Gaussian fit not accurately following the spectra at the high wavelength flank whereas d) shows that a Lorentzian fit can be used for this spectral range instead.

NC for the benefit of large NC from the synthesis. Instead of that the complete growth of the colloidal NC is governed by the so called 'size focusing' regime where small NCs immediately after nucleation grow quickly in size whereas the growth of larger NCs remains comparatively slow [115]. This quickly 'focuses' the size distribution of the NC in the size range of the larger slowly growing NCs. For this reason the high energy side of the spectrum is dominated by small NCs that are changing quickly in size and the collective emission from these NCs is well fitted by a smooth normal distribution. This function describes the inhomogeneous broadening of the small NCs that have a strong

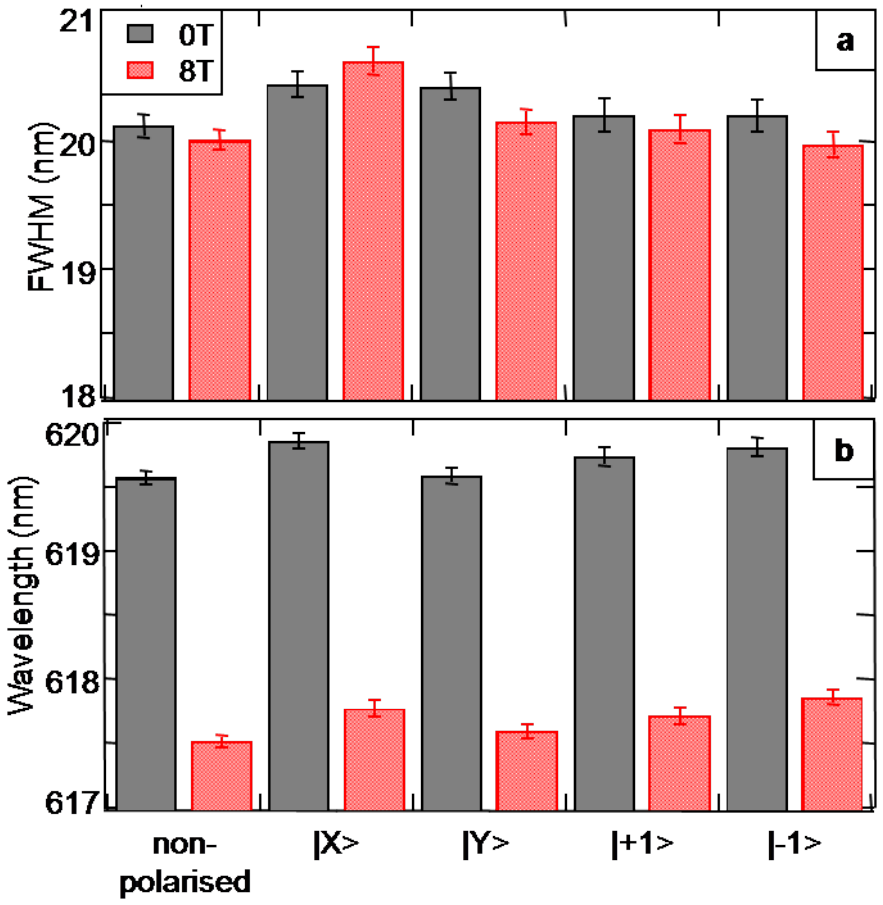

FIGURE 4.7: In a) the FWHM for the emission spectrum of heterostructured *CdSe/CdS*-NRs is shown for non-polarised detection, for two orthogonal linear and two circular polarisations. b) shows the centre wavelength for the emission spectra for non-polarised detection, for two orthogonal linear and two circular polarisations.

size variation. On the other hand the large NCs on the low energy side change their size very slowly during the synthesis. Therefore the variation of size for these NCs is smaller. The emission spectrum at the low energy side is therefore accurately fitted by the Lorentz distribution. This function describes well the nearly homogeneous broadening of the uniformly sized core NCs in the red flank of the emission spectrum.

In figure 4.7a we show the full width at half maximum (FWHM) of the heterostructured NR emission spectra for non-polarised detection as well as for two linear and two circular polarisations for magnetic field strengths of 0 T and 8 T. It can be seen that the FWHM varies inconsistently with different polarisations and different magnetic field strengths. This cannot be explained entirely by a statistical variation of the Gaussian fitting procedure as can be seen by the error bars. However we think that this variation

is not an effect that is related to either the fine structure of the excitonic levels within the $CdSe$-NRs or the application of a magnetic field but rather the influence of variations in the experimental setup. Figure 4.7b however shows a very consistent shift of the central emission wavelength with the application of a magnetic field. We ascribe this move of the spectrum to higher energies to a diamagnetic shift of the energy levels. It has been shown earlier that the diamagnetic coefficient follows a size dependence and decreases for nano structures [116; 117; 113]. This would lead to the conclusion that the diamagnetic shift decreases with decreasing size of semiconductor nanostructures. However the diamagnetic shift we found in the heterostructured $CdSe/CdS$-NR is approximately 6.5 meV which very close to the bulk value [113]. This discrepancy between the earlier findings and our results can be explained on the basis of the theoretical work of Reinecke et al. [114]. Their work established a theoretical description of the diamagnetic coefficient depending on the size of the exciton which depends both on the confinement of the charge carriers in the nanostructure and the Coulomb interaction between them. The investigated heterostructured $CdSe/CdS$-NR provide strong confinement for the hole in the $CdSe$ core with a diameter of 4 nm which is smaller than the bulk exciton Bohr radius of 6 nm [69]. The electron wavefunction however can freely spread over the whole length of the nanostructure and is bound to the hole through the electrostatic interaction. The extension of the exciton within the core/shell NR is therefore much closer to the bulk value and this reflects in the comparatively large diamagnetic shift in these nanostructures. We have to mention that our choice of bulk exciton Bohr radius is somewhat arbitrary as there are many different values for it to be found in the literature: 4.8 nm[118], 5.3 nm[119], 5.7 nm[120] (this is an incomplete list).

We have now introduced the effect of the external magnetic field on the spectrum of the $CdSe/CdS$-NR. However much more information can be drawn from the luminescence decay of the NR emission when applying a magnetic field. In figure 4.8 we show the effect an external magnetic field of varying strength has on the luminescence decay curve of the $CdSe/CdS$-NR sample. The black data points represent the luminescence decay without applied magnetic field and the red data points show the luminescence decay at maximum field strength of 8 T. It can be seen that the two decay curves clearly cross after a certain time. This crossing time τ_{cross} takes on smaller values for higher field

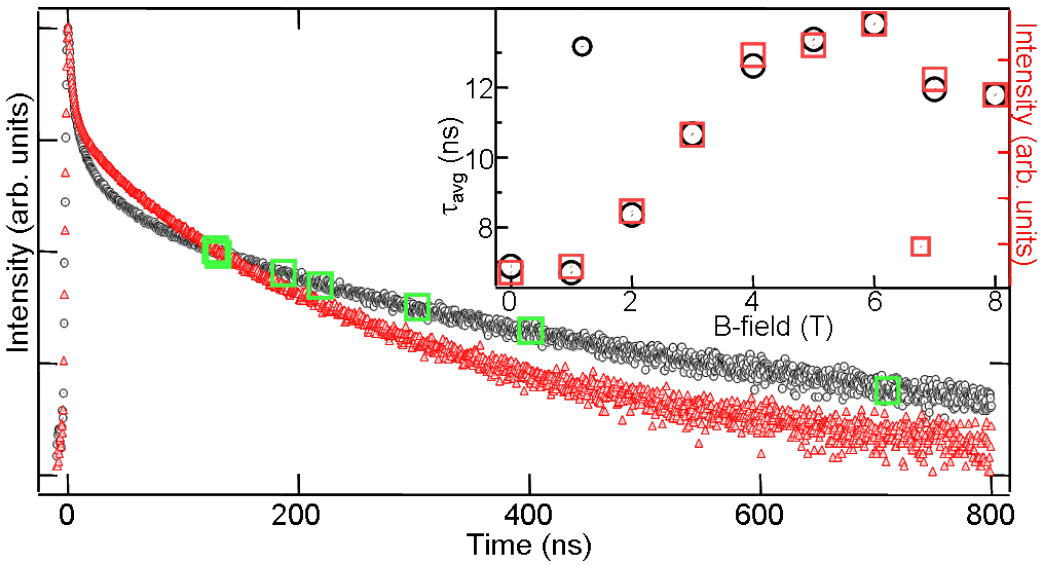

FIGURE 4.8: We show the luminescence decay at 0 T (black) and 8 T (red) of NR with $AR = 3.6$ at the centre of the luminescence spectrum. The green points signify the crossing time τ_{cross} of the luminescence decay with increasing field strength $B = 2\ T,\ ...\ 8\ T$ with the luminescence decay at zero magnetic field. The inset shows the average decay time τ_{avg} calculated using stretched exponential fits of the luminescence decays of different field strengths $B = 0\ T,\ ...\ 8\ T$ compared to the integrated luminscence intensity of these luminescence decays.

strengths which shows that a stronger magnetic field effect is represented by an earlier τ_{cross}. The green squares in figure 4.8 represent the point of crossing for field strengths from 2 T to 8 T in steps of 1 T. The values for the crossing time are given in table 4.1. The decay curves depicted in figure 4.8 have been recorded within a 10 nm wide

B-field strength $[T]$	τ_{cross} $[ns]$
2	709.9
3	401.0
4	302.7
5	218.6
6	187.0
7	130.3
8	127.7

TABLE 4.1: The value for τ_{cross} is shown as determined from luminescence decays at different field strengths.

spectral window at the centre of the NR emission distribution using a spectrometer. No polarisation sensitive elements have been employed during this measurement. Although τ_{cross} is a very intuitive measure of the crossing behaviour of the luminescence decay curve for different magnetic field strengths it is a measure that is difficult to qualify

and does not represent the luminescence decay time τ_{lum} that is commonly used in the literature. To solve this dilemma we have applied a fitting procedure to the NR luminescence decay. As can be seen in figure 4.8 the luminescence decay curves follow a highly multi-exponential behaviour. This complex luminescence decay behaviour arises from a continuous distribution of decay rates that results from effects such as the distribution of aspect ratios and shell thicknesses of the sample, surface charge migration of the electron [121; 122] and a manifold of trap states [123] that interact with the optically allowed excitonic states and add to the non-radiative rate. For these reasons we used the stretched exponential or Kohlrausch function:

$$I(t) = I_0 \cdot \exp\left(-\left(\frac{t}{\tau_s}\right)^{\beta}\right) \tag{4.2}$$

to characterise the luminescence decay curves. Here I_0 is the initial luminescence intensity, τ_s and β are fitting parameters. The function 4.2 was first used in 1854 to describe the discharge of a Leyden jar capacitor [124] and has since been used to describe the decay of disordered systems. Its application to luminescence decay phenomena however has been controversial because it is only a phenomenological description of the system. However several publications have used and investigated the stretched exponential function for the use in luminescence decays [125; 126; 127]. It has even been found that equation 4.2 can be used to describe the decay of a single colloidal nanocrystal emitter [128]. It has been shown by van Driel et al. [129] that the use of the stretched exponential function to describe a luminescence decay can be well justified as long as the integrated intensity of the luminescence decay is proportional to an average decay time τ_{avg} that can be calculated using the fitting parameters β and τ_s from equation 4.2 with the following relation:

$$\tau_{avg} = \frac{\tau_s}{\beta} \cdot \bar{\Gamma}\left(\frac{1}{\beta}\right) \tag{4.3}$$

where $\bar{\Gamma}$ is the mathematical Gamma function. In the inset in figure 4.8 the average decay time τ_{avg} calculated using this formula is plotted against the magnetic field strength together with the integrated luminescence intensity. It can clearly be seen that the two values are proportional. For this reason we argue that the use of the stretched exponential function 4.2 to describe the luminescence decay of the ensemble of heterostructured

CdSe/CdS-NR is well justified.

The magnetic field effect on the luminescence decay described above is dependent on the size of the NR. In figure 4.9 this dependence can be observed. We selected three

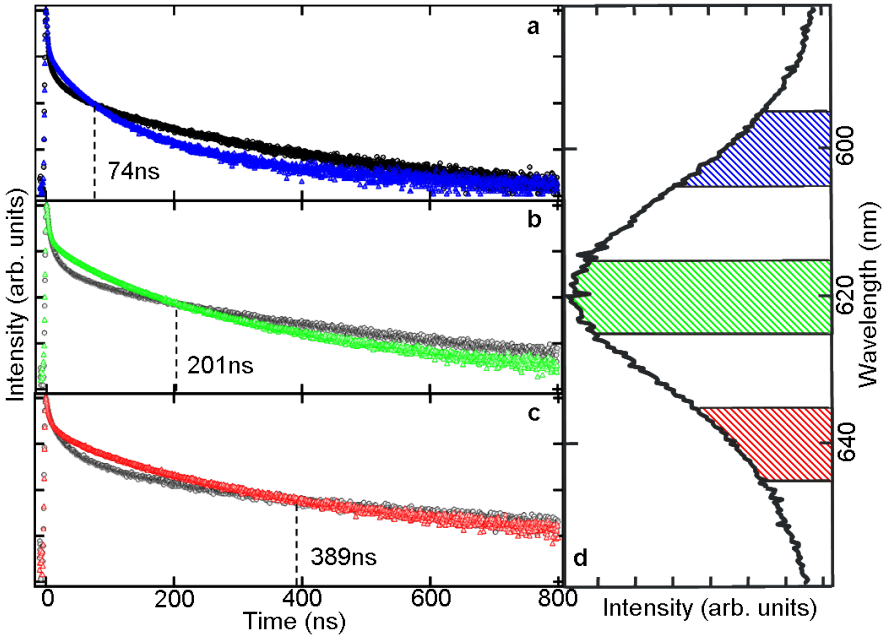

FIGURE 4.9: a), b) and c) show the luminescence decay of *CdSe/CdS*-NRs of $AR = 3.6$ at the high energy flank, the centre wavelength and the low energy flank respectively. The values for the crossing time are displayed. In d) we show the luminescence spectrum for these NRs and we colour code the respective spectral areas that have been used to take the data in a), b) and c).

well separated spectral regions of the *CdSe/CdS*-NR ensemble spectrum and performed non-polarisation sensitive luminescence decay measurements for each of these regions under application of an external magnetic field. In figure 4.9d we can see the ensemble spectrum with the three relevant spectral windows depicted as blue, green and red shaded areas. The width of these spectral regions is approximately 10 nm and the two spectral windows at the periphery of the spectrum are located 20 nm separated from the central wavelength. The figures 4.9a, b, c each show the luminescence decay curves for one respective spectral region laid out in figure 4.9d. Because of the quantum confinement effect described in chapter 2.1.2 the luminescence decay of the NR located at the blue flank of the spectrum represents a sub-ensemble of the NR with a comparatively smaller radius and size than the NR sub-ensemble that emitted the photons making up the luminescence decay at the red flank of the spectrum. This in turn suggests that the magnetic field effect is stronger for smaller excitons because the crossing time τ_{cross}

takes on a smaller value for the NR on the high energy side of the spectrum then for the larger NR in the centre and the low energy side of the spectrum. The same as for τ_{cross}

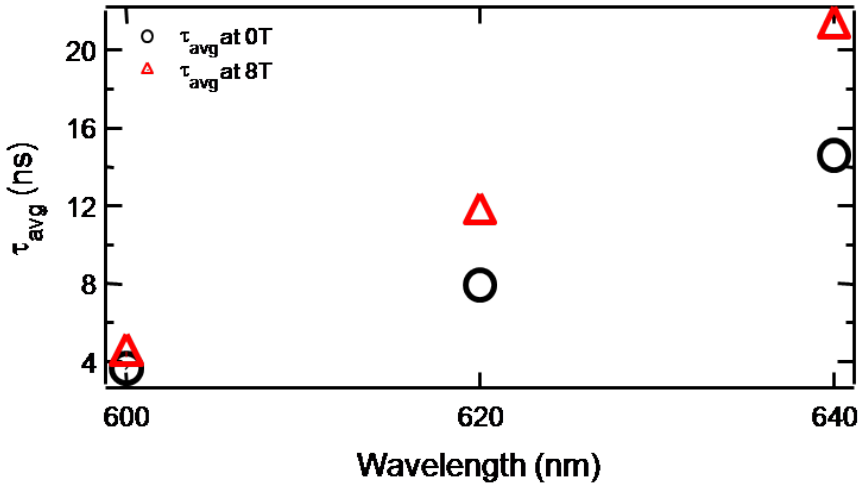

FIGURE 4.10: τ_{avg} for $CdSe/CdS$-NR with $AR = 3.6$ is shown for $B = 0\ T$ (black open squares) and $B = 8\ T$ (red open triangles).

is also true for τ_{avg} that has been calculated from the parameters β and τ_s obtained from fitting the luminescence decays in figure 4.9 using a stretched exponential function 4.2 and equation 4.3. In figure 4.10 we have plotted the calculated values for τ_{avg} over the spectral centre position of the luminescence decays. The black open circles in figure 4.10 represent the values for the three spectral positions for τ_{avg} without applied magnetic field. These values behave very similar to the values for τ_{cross} insofar as τ_{avg} does increase with the size of the NR. However when one compares the values of τ_{avg} in the absence of a magnetic field with the values for τ_{avg} when a magnetic field of $8\ T$ is applied we see that for larger NR the change of τ_{avg} when applying a magnetic field is stronger than for the smaller NR. The implication that the magnetic field effect is stronger for smaller particles taken from our observation of the change in τ_{cross} is misleading. Using τ_{avg} as an observable allows us to directly compare single luminescence decays and is much more reliable than the somewhat phenomenological parameter τ_{cross}.

The change of the average decay time τ_{avg} is governed by two different mechanisms. The well known Zeeman effect [65; 66] splits up the lowest bright $\left|\pm 1^L\right\rangle$ and dark $|\pm 2\rangle$ excitonic states with respect to the sign of their total angular momentum projection. In figure 4.11a, b, c we can see this splitting for the two lowest excitonic levels as they were calculated in figure 4.2. The Zeeman splitting has been calculated using exciton g-factors

of $g_{ex,bright} = 1.5$ [43; 49] for the bright excitonic states and $g_{ex,dark} = 4$ [42; 130] for the dark excitonic states. It can be seen that for larger NR sizes the Zeeman split levels come closer and even cross for the highest magnetic field strength. Figure 4.11a, b, c show the Zeeman-splitting for NR-radii of 1.8 nm, 2.0 nm and 2.2 nm respectively. The

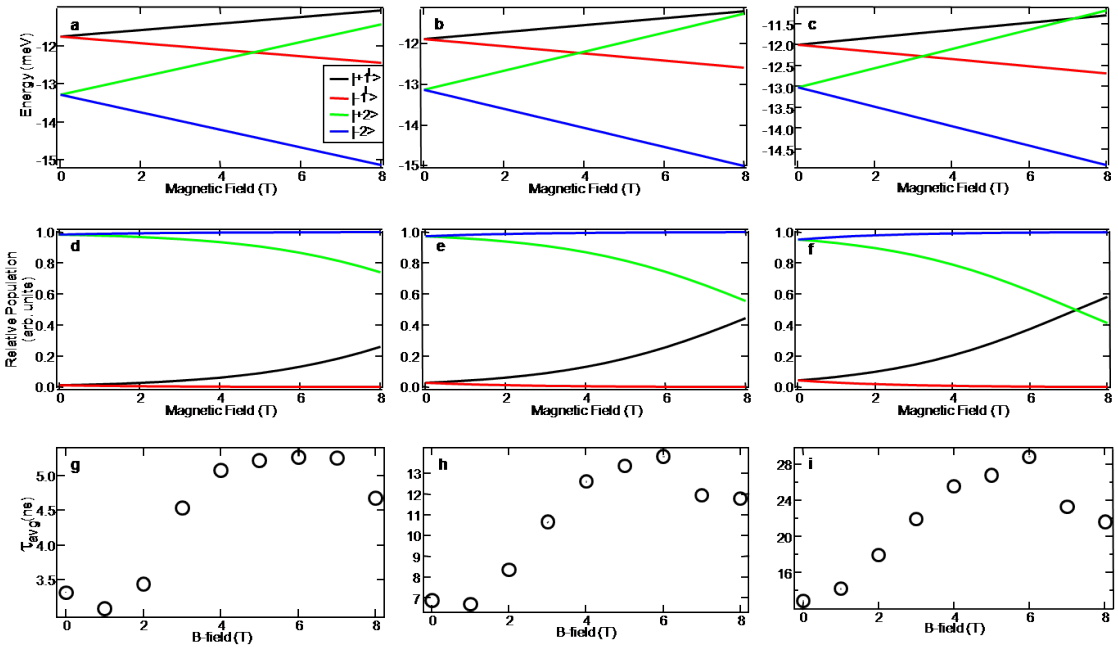

FIGURE 4.11: a, b and c show the Zeeman splitting for the investigated magnetic fields for the lowest two excitonic levels for the blue flank, the centre wavelength and the red flank of the NR emission spectrum respectively. d, e and f show the relative excitonic populations in the thermally linked states $|\pm 2\rangle$ and $\left|\pm 1^L\right\rangle$ in dependence of the magnetic field strength. g, h and i display τ_{avg} over the range of investigated magnetic fields.

$|+2\rangle$ and $\left|+1^L\right\rangle$ states for the smallest size NR come as close to each other as 0.36 meV for the highest magnetic field strength which is close enough to allow thermal coupling ($k_B \cdot 4\ K = 0.34\ meV$). For the largest NR (figure 4.11c) we even observe a crossing of the $|+2\rangle$ and $\left|+1^L\right\rangle$ states for high enough magnetic fields. This size dependent coupling strength is due to the difference in energy splitting of the $|+2\rangle$ and $\left|+1^L\right\rangle$ states between the different NR sizes as can be seen in figure 4.2. Using the energy splitting from figures 4.11a, b, c we can calculate the relative populations applying the formula used in Klimov et al. [131]. This method assumes a Boltzmann distribution and uses the following formulae:

$$n_d = \frac{N}{1 + e^{-\Delta/k_b T}},\ n_b = e^{-\Delta/k_b T} \cdot n_d \tag{4.4}$$

to calculate the number of dark n_d and bright n_b excitons respectively. Here N is the total number of excitons which we set to 1. Furthermore Δ is the energy splitting between the $|+2\rangle$ and $\left|+1^L\right\rangle$ states and between the $|-2\rangle$ and $\left|-1^L\right\rangle$ states respectively, k_b is the Boltzmann constant and T is the temperature in Kelvin. In figures 4.11d, e, f we can see the relative populations we calculated using these formulae and the Zeeman splitting from figure 4.11a, b, c. For the smallest NR and the smallest magnetic fields (see figure 4.11d) all the excitons populate the lower bright excitonic states $|\pm2\rangle$. With increasing magnetic field the $|+2\rangle$ and $\left|+1^L\right\rangle$ states couple thermally and the higher lying bright state starts to become populated with excitons. For the larger NR sizes the dark and bright excitonic states are intrinsically close enough to allow for thermal coupling even without Zeeman splitting at $B = 0\ T$ (see figures 4.11e, f). However with increasing magnetic field strength the population of the $\left|-1^L\right\rangle$ state depletes for the benefit of the $\left|+1^L\right\rangle$ state which happens again through thermal coupling. The intrinsic energy splitting of the largest NR is small enough for a partial population inversion to occur at a magnetic field of $B \approx 7\ T$ as can be seen in figure 4.11f. The effect of the thermal coupling of Zeeman split states has a direct influence on the average decay time τ_{avg} which we can clearly observe in figures 4.11g, h, i. The average decay time τ_{avg} increases with increasing magnetic field up to a certain point after which τ_{avg} starts to decrease again. This tip over point happens at earlier times for larger NR. However thermal coupling alone does not allow us to explain the increase of τ_{avg} as one would expect the opposite to happen as more excitons are allowed to decay through the significantly shorter lived bright excitonic states. Therefore a second mechanism must be at play that depends on the external magnetic field applied. Efros et al. [42] identified such a process in 1996 in their comprehensive work on the exciton fine structure of colloidal $CdSe$-NCs. This second mechanism that shifts the average decay time τ_{avg} to higher values with increasing magnetic field strength is the admixture of the lowest bright $\left|\pm1^L\right\rangle$ and dark $|\pm2\rangle$ excitonic states [132; 133; 45]. This admixture happens in NR that are oriented within the external magnetic field in a way so that the magnetic field has a component perpendicular to the orientation of the spin quantisation axis of the excitons. For these excitons this axis no longer is a valid spin quantisation axis and the dark $|\pm2\rangle$ excitons gain optically active $\left|\pm1^L\right\rangle$ character. On the other hand however, the $\left|\pm1^L\right\rangle$ state will

become less optically active and acquire an overall lower radiative rate Γ_{rad}. For zero magnetic field the excitons that are mainly located in the optically inactive $|\pm 2\rangle$ states decay over the bright excitonic states via an LO phonon assisted transition [131]. The radiative rate Γ_{rad} for this case will be shorter than the inherent $\Gamma_{rad,|\pm 2\rangle} = \infty$ of the dark excitonic states but much longer than $\Gamma_{rad,|\pm 1^L\rangle}$ of the bright excitonic states. As now the dark excitonic states $|\pm 2\rangle$ gain dipole moment through spin mixing with the $\left|\pm 1^L\right\rangle$ sates the average decay time τ_{avg} will become longer because the 'dark' character still dominates and the majority of excitons remain located in the dark excitonic states. For very high magnetic fields however the $|\pm 2\rangle$ states achieve enough dipole moment and the exciton population significantly shifts towards the bright excitonic states so that this trend is stopped and even reversed as can be seen in figures 4.11g, h, i.

In this section we have shown that the diamagnetic shift of the luminescence in heterostructured $CdSe/CdS$-NR is of the same magnitude as for the bulk crystal because of the electron wave function extending into the CdS-shell. After this we established the magnetic field effect on the luminescence decay of the NR and we introduced the concept of τ_{avg} that describes a distribution of decay times as in other stretched exponential decays. Finally we explained a trade off between the Zeeman splitting and the state mixing in an external magnetic field that leads to a non-monotonic behaviour of the average decay time τ_{avg} with increasing magnetic field. In the following sections we explore the specific behaviour of the NR luminescence decay under the influence of either the Zeeman splitting or the spin admixture.

4.3 Polarisation resolved magnetic field effects

This section describes the dependence of the luminescence decay of the heterostructured NR ensemble on the relative orientation of the external magnetic field and the spin of the emitting excitonic states. In figure 4.12 we can see the average decay time τ_{avg} for different polarisation detection schemes plotted against the spectral position of the NR luminescence without external magnetic field applied. In figure 4.12a the decay for the linear states $|X, Y\rangle$ is shown for the three different NR size samples without external

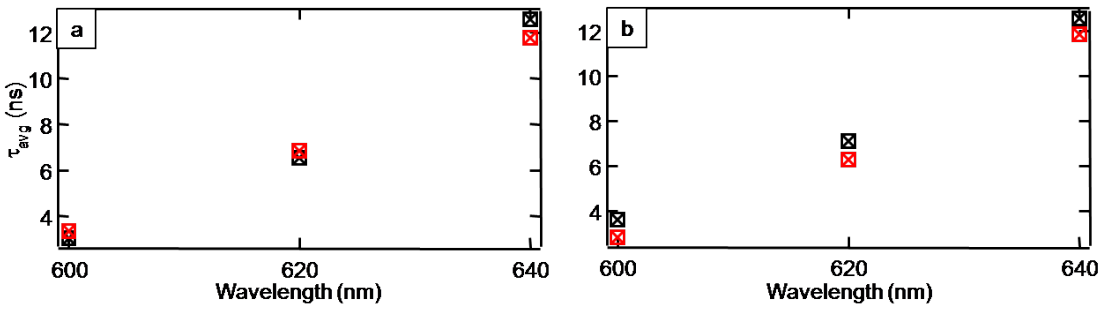

FIGURE 4.12: We show the average decay time τ_{avg} for a) the two linear excitonic states $|X, Y\rangle$ and b) the circular states $\left|-1^L\right\rangle$ (black symbols) and $\left|+1^L\right\rangle$ (red symbols).

magnetic field applied. As in figure 4.10 the average decay time gets longer for larger NRs, as is expected because of the greater separation of the carrier wave functions. The two orthogonal linear polarisations shown as red and black squares in figure 4.12a have the same τ_{avg}. This holds true as well for the two circular states whose average decay time is shown in figure 4.12b. This shows that at zero magnetic field strength there is no inherent splitting of the $\left|\pm 2, \pm 1^L\right\rangle$ states that could be resolved with the methods we used.

For zero magnetic field the direction of detection $\vec{k}$ is isotropic. When applying a non-zero magnetic field however this isotropy is broken and it is important to define the direction of detection with respect to the magnetic field direction. In general two main geometries are used:

1. the Faraday geometry where $\vec{k}||\vec{B}$
2. the Voigt geometry where $\vec{k}\perp\vec{B}$.

In the following we describe the effect of the magnetic field on the NR luminescence decay in Faraday and Voigt geometry.

4.3.1 Faraday geometry

In figure 4.13 we can see the luminescence decays of the NRs for magnetic field strengths $B = 0\ T$ and $B = 8\ T$ as measured at the centre of the ensemble spectrum for the two different circular states $\left|\pm 1^L\right\rangle$. These decays have been measured as shown in figure

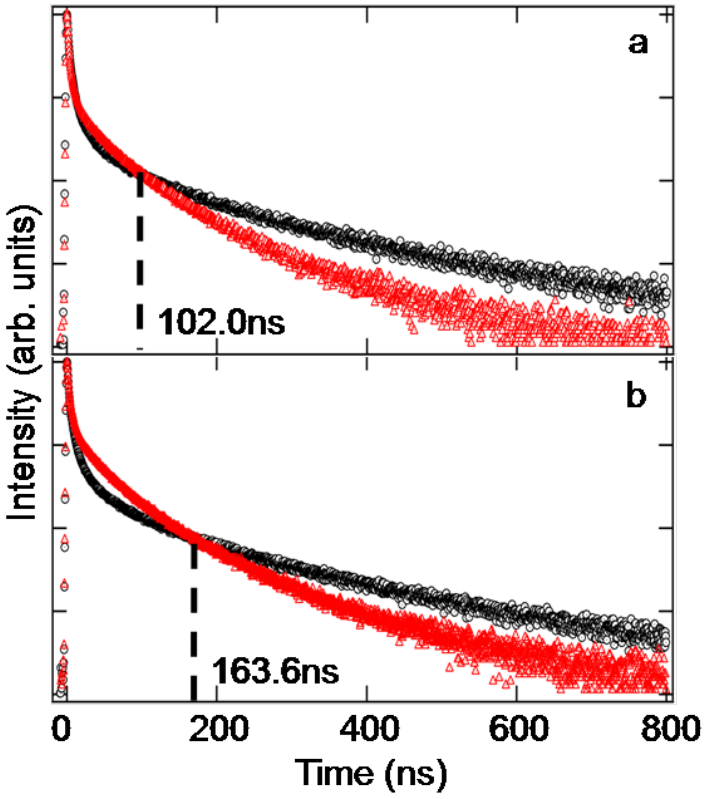

FIGURE 4.13: The luminescence decay curve taken in Faraday geometry without magnetic field (black) and at $B = 8\ T$ (red) is shown for a) the $|-1^L\rangle$ state and b) the $|+1^L\rangle$ state. The crossing time τ_{cross} is displayed for both decays.

4.4b. Figure 4.13a shows the decay for the $|-1^L\rangle$ state without external magnetic field in black triangles and with magnetic field strength $B = 8\ T$ in red triangles. The phenomenological crossing time $\tau_{cross} = 102.0\ ns$ has been shown with a dashed line. Below that in figure 4.13b we show the same for the second circular state $|+1^L\rangle$. In this case the crossing time is much larger with $\tau_{cross} = 163.6\ ns$. As was pointed out before this parameter is only used to illustrate the effect of the magnetic field but has no physical significance. In order to make quantitative comparisons we use the average decay time τ_{avg} that has been extracted from the luminescence decays of different NR size patches. We plotted the average decay time τ_{avg} for the two linear $|X, Y\rangle$ and the two circular states $|\pm 1^L\rangle$ at $B = 8\ T$ in figure 4.14. On the left in figure 4.14a the effect of the magnetic field on the decay of the two linear $|X, Y\rangle$ states is shown. The setup is used in Faraday geometry (see figure 4.4a) so that the two linear states are accessibly by using linear polarisation elements in the detection path. Both linear states are perpendicular to the magnetic field direction $\vec{B}$ and so these states are not subject

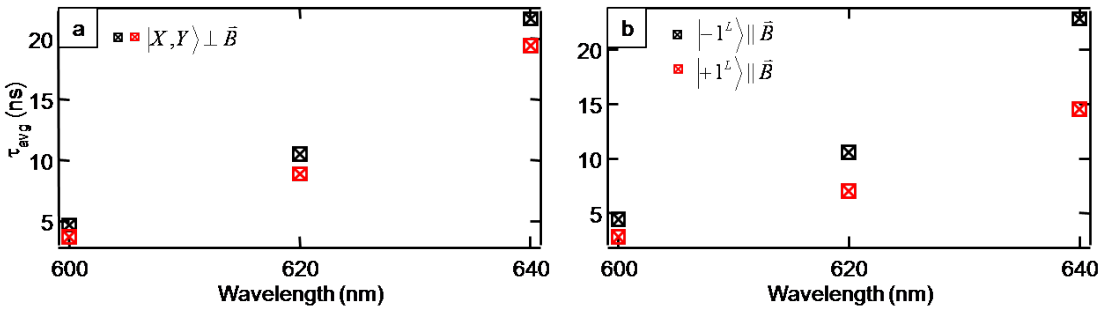

FIGURE 4.14: τ_{avg} is shown for three spectral positions in Faraday geometry for a) the two linear $|X,Y\rangle$ and b) the two circular states $\left|\pm 1^L\right\rangle$.

to the Zeeman splitting. Rather these states will experience a spin admixture where the dipole moment of the constituent $\left|\pm 1^L\right\rangle$ states will be transferred to the dark $|\pm 2\rangle$ states. Although τ_{avg} for the two linear states is the same for the different NR size patches it is very different to the average decay time of the linear state without external magnetic field applied (see figure 4.12a for comparison). This is the effect of the spin admixture because dipole moment of the optical active states is mixed with the dark states and therefore the overall decay becomes slower as more excitons decay directly out of the long lived $|\pm 2\rangle$ states.

In figure 4.14b we show the average decay times for the two bright circular states at $B = 8\ T$ in Faraday geometry (see figure 4.4b). Unlike for the two linear states we can see that τ_{avg} is very different for the two circular states. This comes to pass because of the parallel orientation of the $\left|\pm 1^L\right\rangle$ states' spin projection to the direction of the magnetic field in Faraday geometry. As we have discussed earlier in this case the Zeeman effect splits the two states up due to the sign of their spin projection along the NR $\hat{c}$-axis. As can be seen in figure 4.11a, b, c the Zeeman splitting brings the $|+2\rangle$-state and $\left|+1^L\right\rangle$-state closer together whereas the $|-2\rangle$-state and $\left|-1^L\right\rangle$-state move further apart. This larger energetic distance between the dark $|-2\rangle$-state and the bright $\left|-1^L\right\rangle$-state makes it less likely for the excitons to thermally or via an LO-phonon mediated process [131] be lifted into the optical active state and decay from there. For this reason the average decay time for the circular $\left|-1^L\right\rangle$-state moves to longer times at magnetic field strengths of $B = 8\ T$. The average decay time for the circular $\left|+1^L\right\rangle$-state however remains greatly unchanged as compared to the average decay time for the circular states without external magnetic field applied (see figure 4.12b). We address this to the fact

that the process of LO-phonon mediated activation is already very effective even for the larger energy separations between the $|\pm 2\rangle$ and $\left|\pm 1^L\right\rangle$ states at $B = 0\ T$.

The decays for the different linear and circular polarisations obtained in Faraday geometry allow us to disentangle the two different effects of Zeeman splitting for the spins quantised parallel to the direction of the magnetic field $\vec{B}$ and the spin-admixture for those quantised perpendicular to $\vec{B}$. Although the overall effect for the spin-admixed states represented in figure 4.14a is of the same order of magnitude as the effect for the Zeeman split $\left|-1^L\right\rangle$-state shown in figure 4.14b the difference between the two effects can clearly be seen by the anisotropy of the two Zeeman split states that does not occur for the spin-admixed states.

4.3.2 Voigt geometry

In contrast to the polarisation dependent measurements we showed in section 4.3.1, when performing polarisation sensitive measurements in Voigt geometry different relative orientations of the heterostructured NR and the magnetic field can be accessed. As can be seen in figure 4.5a by detecting two perpendicular linear polarisation states we can distinguish directly between states with spin projection parallel and perpendicular to the magnetic field. In figure 4.15 we show the luminescence decay curves for these two orthogonal linear $|X, Y\rangle$-states. In figure 4.15a the luminescence decay at $B = 0\ T$ in black and at $B = 8\ T$ in red is shown for the linear states whose spin quantisation is parallel to the magnetic field direction. The crossing time $\tau_{cross} = 132.6\ ns$ is emphasised by a dashed line. This τ_{cross} is significantly shorter than for the orthogonal states that are aligned perpendicular to the magnetic field direction where $\tau_{cross} = 260.7\ ns$. This is because for the first the Zeeman splitting brings the $\left|+1^L\right\rangle$-state and the $|+2\rangle$-state closer together and the population of the $\left|-1^L\right\rangle$-state is depleted for the benefit of the $\left|+1^L\right\rangle$-state as can be seen in figure 4.11d, e, f.

However as mentioned earlier τ_{cross} is not a parameter with real physical meaning and therefore it is necessary to extract the average decay time τ_{avg} using equations 4.2 and 4.3. We have conducted luminescence decay measurements for the two orthogonal linear polarisations for magnetic field strengths from $B = 0\ T$ to $B = 8\ T$ in steps of

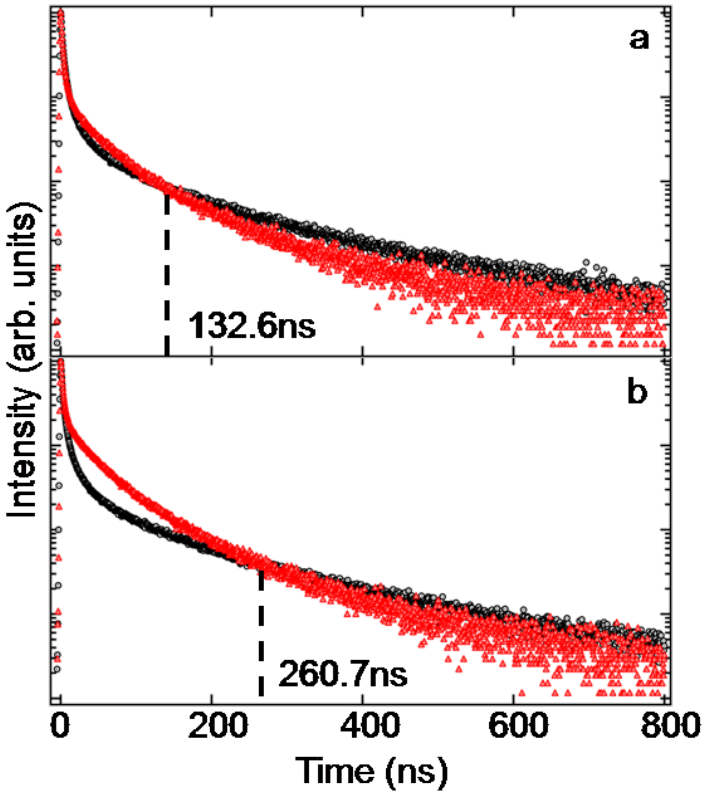

FIGURE 4.15: The luminescence decay curve taken in Voigt geometry without magnetic field (black) and at $B = 8\ T$ (red) is shown for a) the $|-1^L\rangle$ state and b) the $|+1^L\rangle$ state. The crossing time τ_{cross} is displayed for both decays.

$\Delta B = 1\ T$. The average decay times for these decays have been calculated and we normalised the obtained $\tau_{avg}\,(x\ T)$ for non-vanishing magnetic field strengths $B = x\ T$ by the average decay time $\tau_{avg}\,(0\ T)$ at zero magnetic field. Figure 4.16 shows these results. The black circles represent the linear $|X, Y\rangle$-states that are subject to the Zeeman splitting. As indicated earlier the average luminescence decay time for these states does not change very strongly with increasing magnetic field and increases only by a factor of 1.5 even for the strongest external magnetic fields we applied. This is due to the strong LO-phonon activation already at zero magnetic field strength. In addition it can be observed that the change of τ_{avg} for the Zeeman split states trails off already for magnetic field strengths of $B = 5\ T$ and after that asymptotically approaches a value of ≈ 1.5. The red triangles on the other hand represent the linear $|X, Y\rangle$-states that experience a spin-admixture with the lower lying optically inactive states. It can be observed that the change of the average decay time for these states is much stronger than for the case of the Zeeman splitting. Over the complete range of magnetic field

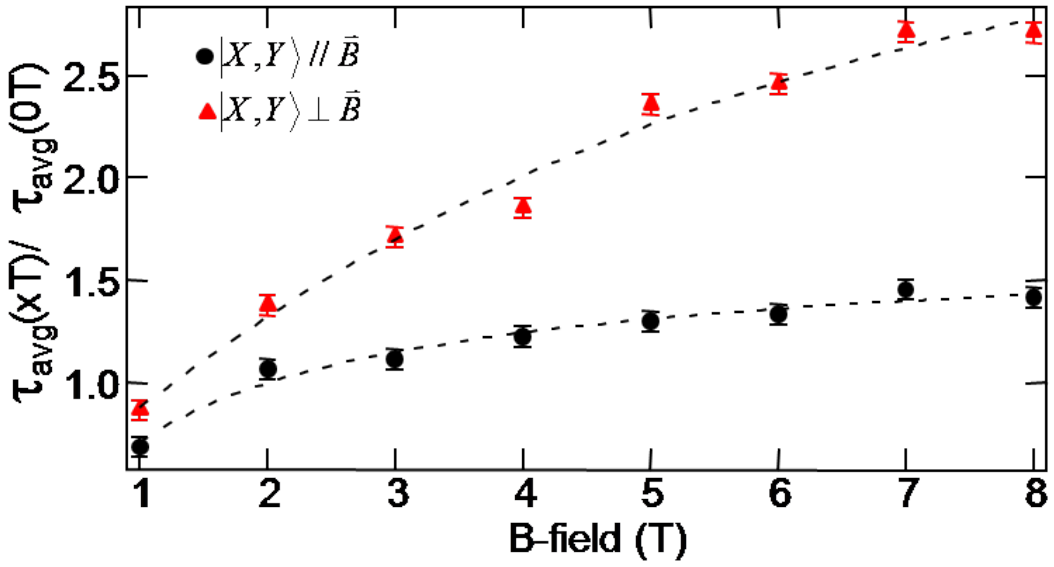

FIGURE 4.16: The graph shows the relative increase compared to the case of $B = 0\ T$ of τ_{avg} for the linear excitonic states aligned parallel (black) and perpendicular (red) to the magnetic field in Voigt geometry.

strengths τ_{avg} for the spin-admixed states increases by a factor of 2.7. In addition to that, the change in average luminescence decay time does not trail off as for the Zeeman split states. This leads us to the assumption that the process of spin-admixture does by no means saturate at magnetic fields up to $B = 8\ T$.

Not only can we investigate the magnetic field effects in dependence of the magnetic field strength but also, as with the measurements performed in Faraday geometry, of the different size patches of heterostructured $CdSe/CdS$-NR. In figure 4.17 we show the

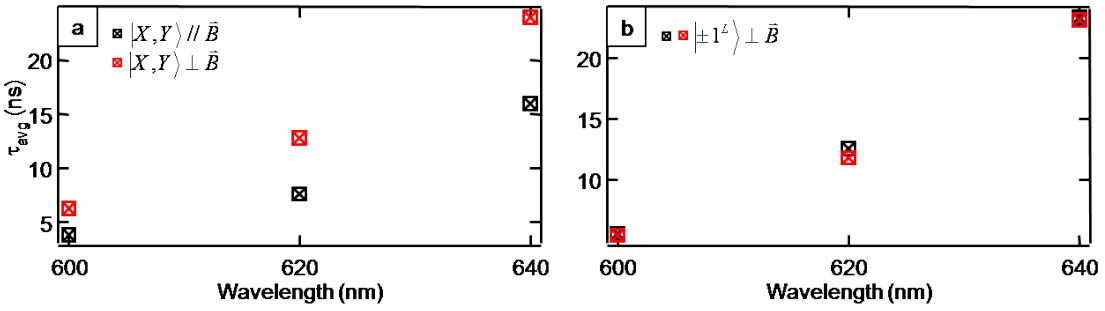

FIGURE 4.17: τ_{avg} is shown for three spectral positions in Voigt geometry for a) the two linear $|X,Y\rangle$ and b) the two circular states $|\pm 1^L\rangle$.

average decay time for two orthogonal linear polarisation states (figure 4.17a) and for the two different circular states (figure 4.17b). As we have already observed in figure 4.16 the

average decay time for the $|X,Y\rangle$-states subject to Zeeman splitting (black open squares in figure 4.17a) changes little compared to the zero magnetic field case (compare to figure 4.12). For the orthogonal linear states that are subject to spin-admixture however the change of τ_{avg} is much stronger. In figure 4.17a one can see as well that the average decay time changes more for larger NR on the red side of the luminescence spectrum than for the smaller NR on the high energy side. This effect is due to the dependence of the spin admixture on the exchange interaction [102] which for heterostructured NR is strongly dependent on their size. On the right in figure 4.17b τ_{avg} is plotted for the circular polarisation states $\left|\pm 1^L\right\rangle$. The average decay time for both of these states behaves essentially the same for the different NR size patches. This is because the relative orientation to the magnetic field direction $\vec{B}$ of the spin projection for the $\left|\pm 1^L\right\rangle$-states is the same. Both of them are subject to spin-admixture as can be seen in figure 4.5b.

We have shown in this section that by employing polarisation sensitive detection in Faraday and Voigt geometry different excitonic fine structure levels are accessible even in the ensemble without high resolution spectroscopic methods. The different excitonic energy levels are apparent in the evolution of their decay characteristics with increasing magnetic field strength. We could demonstrate that with our setup in Faraday geometry the composite linear states $|X,Y\rangle$ are both subject to bright/dark state spin admixture. The circular $\left|\pm 1^L\right\rangle$ states however experience Zeeman splitting and an uneven change of thermal coupling to the optically forbidden and equally Zeeman split $|\pm 2\rangle$ ground states. In Voigt geometry however the setup allows us to directly distinguish between the Zeeman effect and the spin admixture in the linear $|X,Y\rangle$ states. Detection of two perpendicular linear luminescence polarisations permitted to select linear states aligned parallel and orthogonal to the magnetic field direction. The spin admixed states showed a significant increase of τ_{avg} due to more photons being directly emitted from the originally optically inactive $|\pm 2\rangle$ states.

Chapter 5

Electric field mediated carrier separation in heterostructured nanorods

This chapter explains our findings on the effect of an external electric field on the luminescence decay of a sample of heterostructured $CdSe/CdS$-NRs. We support our findings with semi-analytical calculations of the exciton energy levels and numerical calculations of the carrier overlap in these semiconductor nanostructures with mixed dimensionality [41].

Electric fields have been used for a long time in self assembled semiconductor quantum dots to change the carrier wave function overlap, the oscillator strength and the radiative rates [134; 135; 136]. The application of electric fields to epitaxially grown QD is comparatively easy because the growth process of these nanostructures allows macroscopic alignment of the microscopic QD crystal structure within the setup. For colloidal nanoparticles however the isotropic orientation of the individual particles within the ensemble renders the microscopic alignment within a spectroscopic setup more difficult. The advent of single particle spectroscopy allowed the access of single NCs within a highly diluted ensemble sample [52] but alignment still remained elusive. Semiconductor NRs and especially heterostructured NRs however allow one to distinguish different

relative alignments of individual NR within a capacitor structure [54; 53; 57]. This technique even facilitates the electrical control of fluorescent resonant energy transfer from heterostructured NRs [56].

The investigated $CdSe/CdS$-NRs earn a special place with respect to electric field controlled spectroscopy as they provide strong confinement for the hole only whereas the electron can diffuse into the extended CdS-shell. In figure 5.1 we show a sketch of

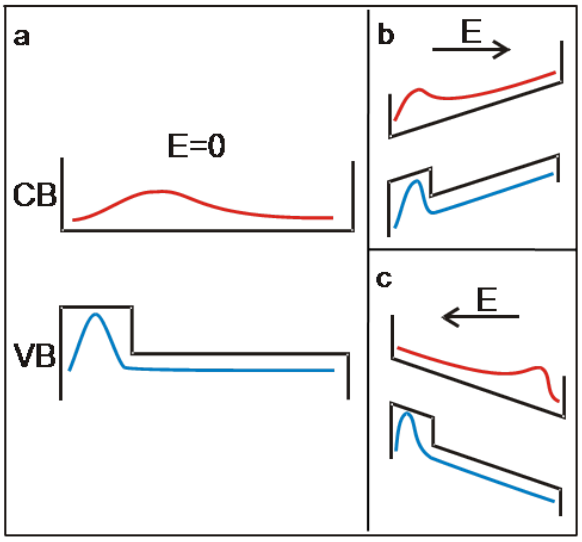

FIGURE 5.1: A schematic representation of the electron and hole wavefunctions in heterostructured $CdSe/CdS$-NRs for the case of a) no external electric field, b) an external electric field parallel to the NR's $\hat{c}$-axis and c) an external electric field antiparallel to the $\hat{c}$-axis applied.

the effect an applied electric field has on the carrier wave functions for two distinctive orientations of the electric field with respect to the NR. Figure 5.1a shows the case of zero applied electric field. The conduction band (CB) and the valence band (VB) are undistorted and flat. The hole is confined wholly in the $CdSe$-core due to the VB offset between the core and shell materials. The CB offset between $CdSe$ and CdS in this nanostructure however is vanishingly small [54] and the electron wave function therefore is permitted to diffuse out into the CdS-shell. The Coulomb interaction between electron and hole alone distorts the electron wave function towards the $CdSe$-core. In figures 5.1b, c we can see the cases of an electric field $\vec{E}$ aligned parallel and anti-parallel to the $\hat{c}$-axis of the NR. In the first case the electron wave function is drawn strongly towards the $CdSe$-core and consequently towards the hole wave function. For this case

the exchange interaction as well as the radiative rate of the exciton is expected to increase. This in turn will affect the excitonic energy levels. The latter case shows that an anti-parallel arrangement between $\vec{E}$ and the NR $\hat{c}$-axis results in the opposite effect where the electron is pulled away from the $CdSe$-core. Hence the carrier wave function overlap should decrease in this arrangement. We now describe the results of our numerical calculations of the electric field effect on the $CdSe/CdS$-NRs.

5.1 Numerical calculations of carrier separation

In section 3.2 we described a numerical approach to calculate the wave functions and energy levels of excitons in strongly non-spherical NCs. We can apply the same method

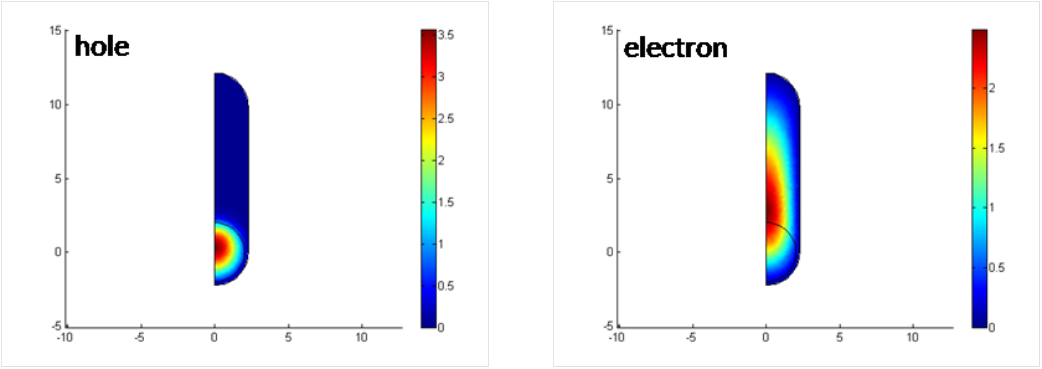

FIGURE 5.2: Colour coded diagram of the electron and hole wavefunctions in the investigated NR with $AR = 3.6$ without external electric field applied. For symmetry reasons only one half section through the NR along the $\hat{c}$-axis was used for the calculations.

to investigate the effect of an external electric field. In figure 5.2 we show a graphical representation of the hole and electron wave function as we calculated them using said method. The external electric field in this case was zero. In the left picture the hole wave function can be seen to be completely confined within the $CdSe$-core. It experiences a slight deformation towards the extended CdS-shell due to electrostatic interaction. The right picture shows the electron wave function that, as predicted, extends far into the elongated CdS-shell because the CB of the core and shell material are equal. The electron wave function can be seen to be slightly distorted due to the Coulomb interaction. In figure 5.3 the carrier wave functions are shown with an electric field of $E = 300\ \frac{kV}{cm}$

applied along the $\hat{c}$-axis of the NR. In the left picture the strongly confined hole wave

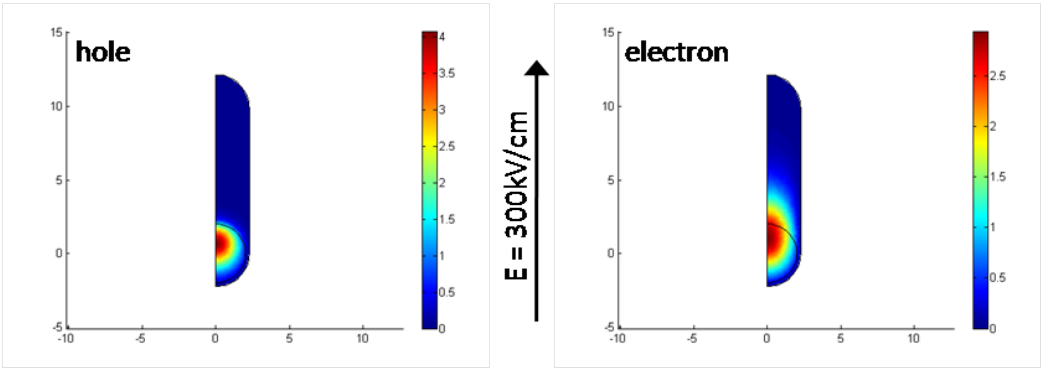

FIGURE 5.3: Colour coded diagram of the electron and hole wavefunctions in the investigated NR with $AR = 3.6$ with an external electric field of $E = 300\ \frac{kV}{cm}$ applied parallel to the crystal's $\hat{c}$-axis.

function can be seen to be deformed stronger than in the case of zero electric field. This deformation results from the enhanced overlap with the electron wave function as can be seen in the picture on right. The electron wave function is pulled towards the hole wave function residing in the $CdSe$-core. This increases the carrier wave function overlap strongly. It can clearly be seen in figure 5.3 on the right that the electron wave function is much stronger confined when a parallel electric field is applied than for zero electric field strength. In figure 5.4 we show the results for the opposite case where an electric field of $E = 300\ \frac{kV}{cm}$ is applied anti-parallel to the NR $\hat{c}$-axis. In the left picture the wave function of the hole can be seen to be confined in the core as it is for the earlier two cases. However the hole wave function in figure 5.4 is more symmetric than

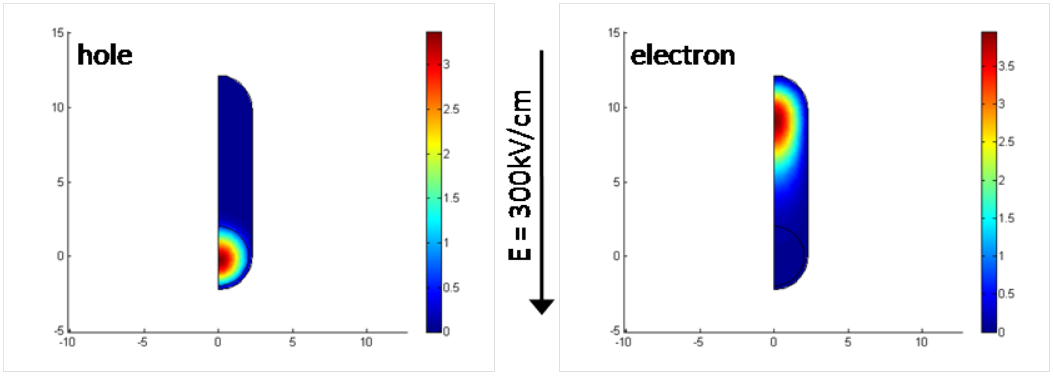

FIGURE 5.4: Colour coded diagram of the electron and hole wavefunctions in the investigated NR with $AR = 3.6$ with an external electric field of $E = 300\ \frac{kV}{cm}$ applied antiparallel to the crystal's $\hat{c}$-axis.

for the earlier cases because the separation to the electron wave function is much larger and therefore the effect of the electrostatic interaction is diminishing. On the right in figure 5.4 the electron wave function is shown to be located at the opposite end of the heterostructured NR and it is less extended than in the case of $E = 0\ \frac{kV}{cm}$.

As figures 5.2, 5.3 and 5.4 suggest we can tune the overlap between electron and hole wave functions by applying an external electric field along the $\hat{c}$-axis of the heterostructured $CdSe/CdS$-NR. In figure 5.5 we show the change of the wave function overlap with electric field strength. The electric field in this case is taken to be aligned in paral-

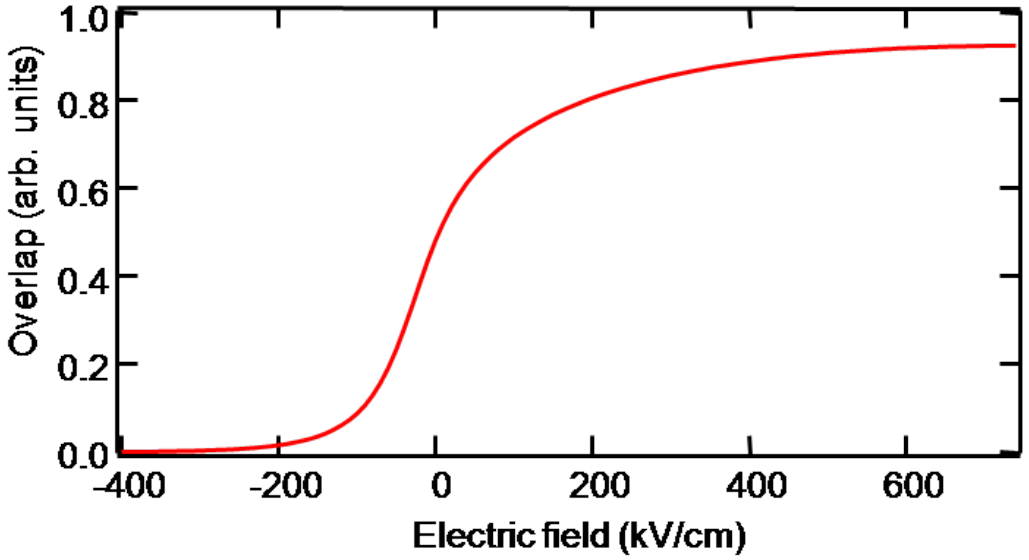

FIGURE 5.5: The carrier wave function overlap in heterostructured $CdSe/CdS$-NR with $AR = 3.6$ is shown for different electric field strengths applied parallel to the crystal's $\hat{c}$-axis.

lel with the wurtzite $\hat{c}$-axis of the NR. The electric field strength used in the numerical calculations was changed from $E = -1\frac{MV}{cm}$ to $E = 1\ \frac{MV}{cm}$. However for electric field strengths higher than $E = 740\ \frac{kV}{cm}$ the numerical solution of the Schrödinger equation broke down and no solutions for these field strengths were obtained. For negative electric field strengths the wave function overlap decreases quickly from the zero field value $Overlap_{E=0\ \frac{kV}{cm}} = 0.48$ and asymptotically approaches zero. For this reason we do not plot the overlap for electric field strengths less than $E = -400\ \frac{kV}{cm}$ in figure 5.5. For positive field strengths the wave function overlap increases quickly at first but starts to flatten out at an electric field strength of $E = 100\ \frac{kV}{cm}$. The overlap does not reach unity even for the highest positive electric field strength at which the numerical calculation

produced a result. The highest overlap achieved is $Overlap_{E=740\ \frac{kV}{cm}} = 0.92$ and we take this to be an indication that the overlap is limited by electron diffusion into the CdS-shell even at very high external electric fields.

We have shown in section 2.1.3 that the exciton energy depends on the exchange interaction $\hat{H}_{exch}$ (see formula 2.28). Within the numerical calculations we can obtain the energy for the electron E_e and the hole E_h and add them together to give the energy of the exciton $E_{exciton} = E_e + E_h + E_{g,CdSe}$, with $E_{g,CdSe}$ being the energy gap of $CdSe$. In figure 5.6 we plot E_e and E_h versus the external electric field strength. It can clearly be seen that E_h does not vary as strongly as E_e over the whole range of

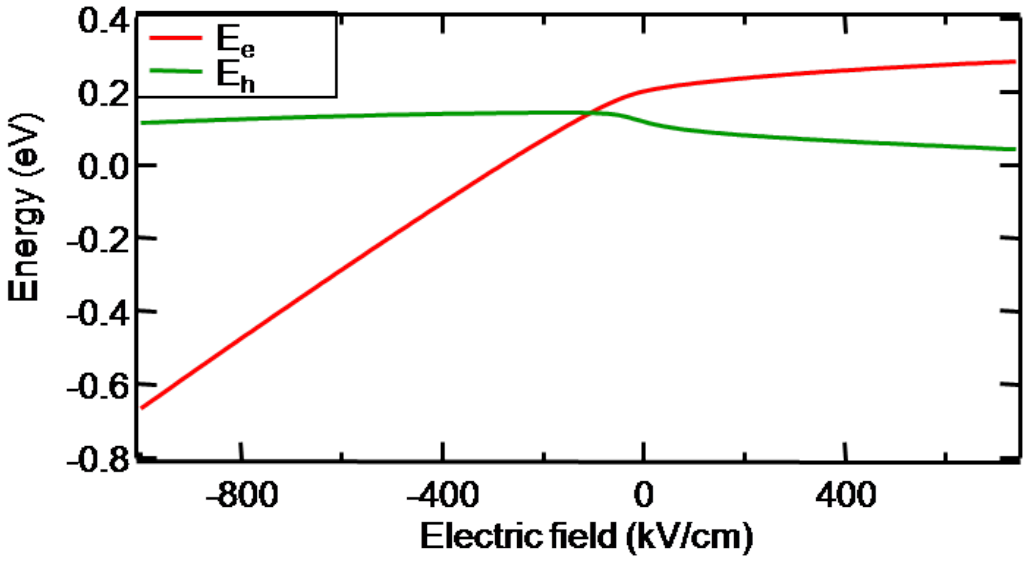

FIGURE 5.6: The electron and hole energy (E_e and E_h respectively) in the investigated NRs are displayed over the applied electric field oriented parallel to the NR $\hat{c}$-axis.

electric field strengths. From the strongest negative electric field strength E_h increases by 24% and reaches its maximum at $E_{h,E=-160\ kV/cm} = 0.1448\ eV$. By changing the electric field strengths to positive values E_h decreases again and reaches it lowest value at $E_{h,E=740\ kV/cm} = 0.0437\ eV$. The dependence of the hole energy on the electric field strength can be understood as a combination of a change in the Coulomb interaction as the electron-hole-separation increases and a change of the kinetic energy of the hole as the overlap with electron wave function increases. However these changes are relatively small as the confinement of the hole wave function in the $CdSe$-core dominates. The electron energy E_e on the contrary changes much more strongly with electric field

strength. The behaviour of E_e for negative field strengths can be explained in the context of a quantum confined Stark effect (QCSE) [137; 138; 54]. For positive electric field strengths however no QCSE can be observed. This is direct evidence of the non-symmetrical structure of the hole confinement and so applying stronger and stronger positive electric fields does not change the overlap of the carrier wave functions any more.

With the data obtained so far (wave function overlap and E_h) we can calculate the exciton fine structure levels in the heterostructured NR in dependence on the external electric field strength (see formulae 2.28). In figure 5.7 we display the exciton fine structure calculated in this manner. For negative values of the electric field the different fine

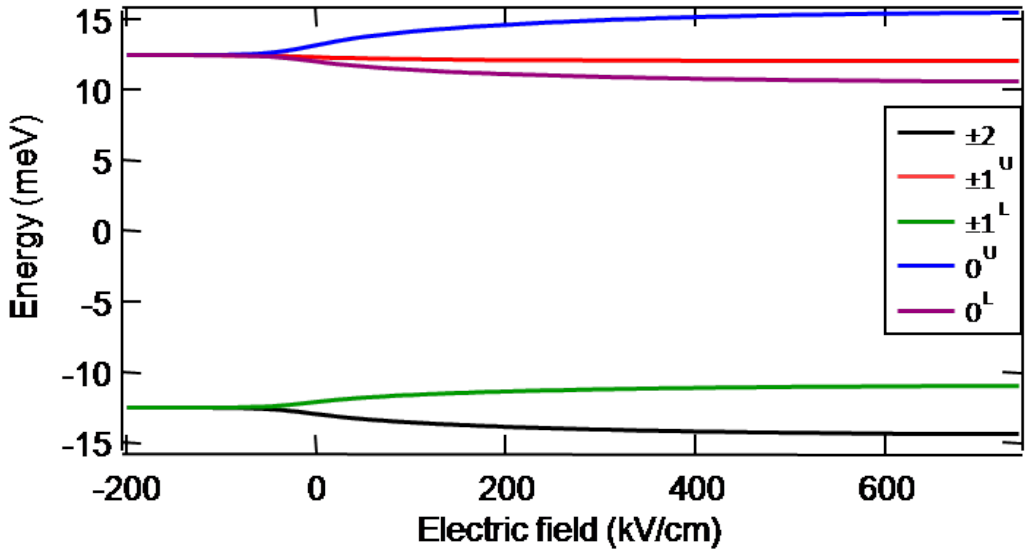

FIGURE 5.7: The excitonic fine structure levels are displayed over an external electric field applied parallel to the NR $\hat{c}$-axis.

structure levels move towards each other and finally become degenerate at an electric field strength of $E = -200\ \frac{kV}{cm}$. This is an effect of the reduction of the wave function overlap and the resulting vanishing exchange interaction that splits up the otherwise degenerate exciton levels. Positive external electric fields have a similar effect as reducing the radius of the NR would have (compare to figure 4.2b) as it increases the energy splitting between the otherwise degenerate exciton levels. This similar effect to reducing the NC radius happens because it confines the carrier wave functions to a smaller space and in this way increases the quantum confinement. The applied electric field however

does barely change the confinement for the hole whereas the electron wave function experiences a very strong potential gradient towards the $CdSe$-core due to the electric field (compare figure 5.3) that increases the confinement.

5.2 Luminescence decay resolved luminescence quenching in heterostructured nanorods

After having provided the theoretical background of electric field effects on excitons in heterostructured $CdSe/CdS$-NR in section 5.1 we will now detail our experimental findings. In figure 3.1 we can see the structure of the capacitor sample containing the investigated $CdSe/CdS$-NRs in a polystyrene matrix. This sample architecture allows us to apply electric fields to the NRs and in the same experiment perform time resolved spectroscopy on them. In figure 5.8 we show the effect of an applied electric field on the luminescence decay of the investigated sample. Figure 5.8a shows the luminescence decay at different electric field strengths but without an external magnetic field applied. For increasing electric field strength the decays become faster which in turn points towards an electric field induced quenching as well because the intensity of the decay curve relates directly to the decay time τ_{avg}. The increase in fluorescence decay rate is due to the increased overlap in suitably aligned heterostructured $CdSe/CdS$-NRs. For the data in figure 5.8 no polarisation sensitive setup was used and we will see in due course that, unlike the case of external magnetic fields, no polarisation sensitive effect for external electric fields is expected. In figure 5.8b we can see the case for both an external electric and magnetic field applied to the sample. The effect of the electric field is the same as for $B = 0\ T$ because the influence of the electric field is independent from the Zeeman splitting and the spin admixture induced by the external magnetic field. We have labelled the decay curves in figure 5.8 by the voltage we applied to the sample. However it is difficult to know exactly the strength of the resulting electric field as the sample was mounted inside a cryostat filled with liquid He and no direct measurement of the actual voltage at the sample was possible.

We now investigate the effect of the electric field on different sizes of NR. In figure 5.9 we show the electric field quenching for three different spectral windows of the ensemble

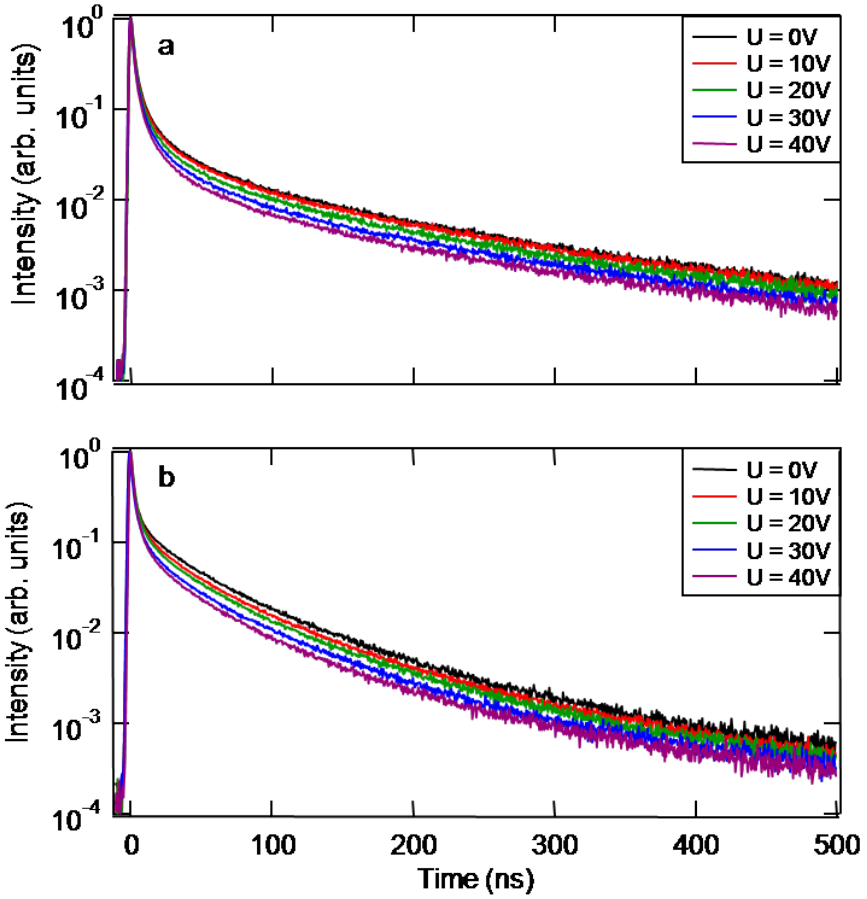

FIGURE 5.8: The luminescence decay of the investigated NR is shown for different external electric field strengths a) without a magnetic field and b) with a magnetic field of $B = 8\ T$ applied.

luminescence (see figure 4.9) which, due to the quantum confinement effect, represents three different size distributions of NR. The NR size distributions are centred around median radii of 1.8 nm (figure 5.9a), 2 nm (figure 5.9b) and 2.2 nm (figure 5.9c). Intuitively it seems as if the luminescence decay with an external electric field applied (red curves) are changed very similarly for the different NR sizes as compared to the initial luminescence decay (black curves). In order to make a quantitative comparison we used the stretched exponential decay function 4.2 in order to fit the luminescence decays and function 4.3 for the average decay time τ_{avg} to obtain a quantitative decay parameter that is proportional to the decayed intensity of light. In the inset in figure 5.9c we show the results for τ_{avg} for all the decays shown in figure 5.9. One can see that the absolute change of τ_{avg} under an electric field increases with increasing NR size.

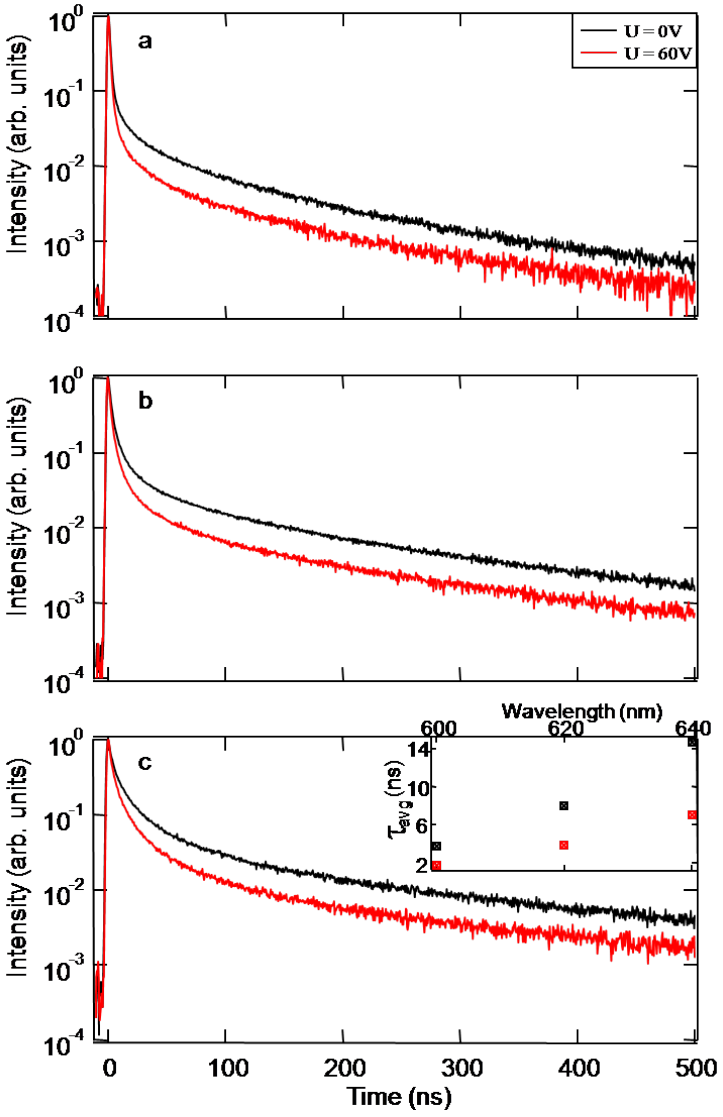

FIGURE 5.9: a), b) and c) show the NR's luminescence decay without external electric field (black) and with external electric field (red) applied for the three spectrally selected *CdS*-core radii of 1.8 *nm*, 2 *nm* and 2.2 *nm* respectively. The inset in c) shows τ_{avg} for all the decays shown.

However if one uses the following equation:

$$Q_{x\ V} = \frac{\tau_{avg,0\ V} - \tau_{avg,x\ V}}{\tau_{avg,0\ V} + \tau_{avg,x\ V}} \tag{5.1}$$

in order to calculate the decay quenching produced by the electric field the picture changes. The values of quenching obtained for the three different NR sizes are:

$$Q_{60\ V} = \begin{cases} 0.367 & for \quad r = 1.8\ nm, \\ 0.351 & for \quad r = 2\ nm, \\ 0.349 & for \quad r = 2.2\ nm. \end{cases} \tag{5.2}$$

One can see that the quenching is marginally stronger for smaller NR contrary to intuition. However this effect is very small and could indeed only be a statistical variation or error introduced by the fitting. In conclusion we can see that the electric field quenching is independent of NR size for small variations of it.

The luminescence decays we have presented so far have been measured without using polarisation sensitive setups. In chapter 4 we have seen that by resolving the luminescence decay of the NR ensemble we are able to discern different fine structure levels. However we will argue that the effect of the electric field is the same for all these cases. In figure 5.10 we show the average decay time obtained with different polarisation sensitive setups. Figures 5.10a and b show two perpendicular linear polarisations and figures

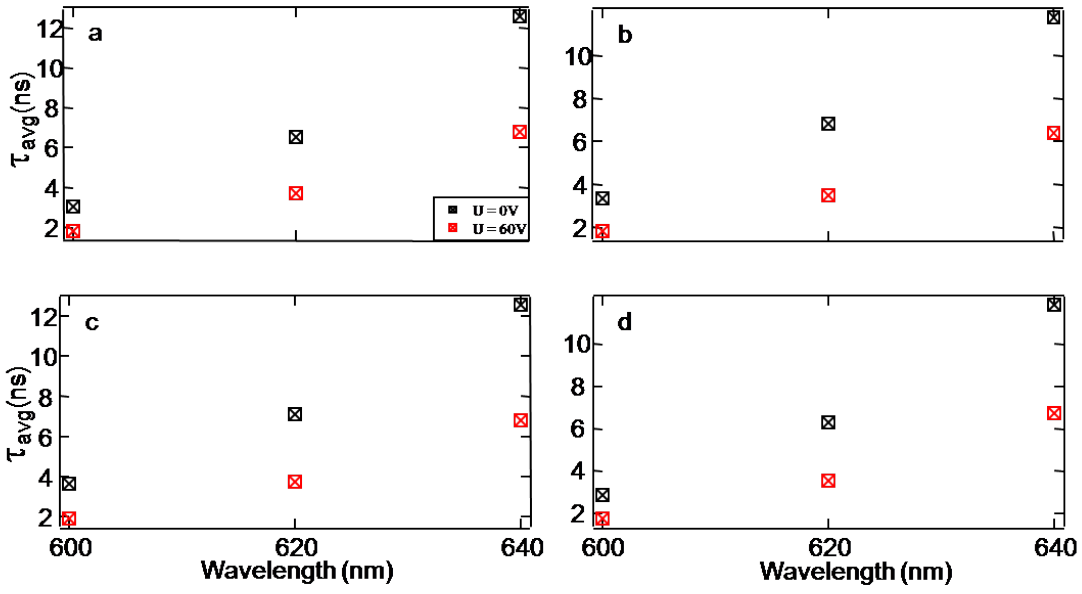

FIGURE 5.10: a) and b) show τ_{avg} for the linear excitonic states $|X, Y\rangle$ without electric field (black) and with electric field (red) applied. c) and d) show τ_{avg} for the circular excitonic states $|\pm 1_L\rangle$ without electric field (black) and with electric field (red) applied.

5.10c and d show two circular polarisations. It can be seen that for these four different

polarisations the quenching effect of the electric field seems to be very similar as the range for τ_{avg} does not change considerably between the different cases. An analysis of the values of quenching gives an average value of $\bar{Q}_{60\ V} = 0.289$ for the four different polarisations and standard deviation of $\sigma(Q_{60\ V}) = 0.024$. We know that the quenching is independent of NR size and no complete set of sizes for a single polarisation deviates from $\sigma(Q_{60\ V})$ and so we can conclude that the electric field effect does not seem to change for different polarisations of the NR ensemble emission. When we treated the magnetic field effect in chapter 4 we could discern the two different effects of Zeeman splitting and spin admixture by selectively measuring different light polarisations that depend on the orientation of the spin quantisation axis within the magnetic field. In the case of the electric field however the physical orientation of the NR within the electric field is the relevant parameter rather than the spin. However one defined alignment of the spin quantisation axis within the electric field can be fulfilled by both parallel as well as anti-parallel orientations of the respective $CdSe/CdS$-NR. For this reason we cannot distinguish using polarisation sensitive detection the difference between a NR oriented parallel or anti-parallel to the electric field direction.

5.3 Luminescence decay resolved exciton storage in heterostructured nanorods

We have shown that the average decay time of heterostructured $CdSe/CdS$-NRs can be modulated using external electric fields in section 5.2. We could explain these results on the basis of a modulation of the electron-hole separation and hence the wave function overlap as shown in section 5.1. Now we demonstrate that this can be used to store excitons in these core-shell NR for several hundred nanoseconds.

In order to store excitons in the heterostructured NR an electric field $\vec{E}$ can be applied anti-parallel to the NR $\hat{c}$-axis (see figure 5.4). This electric field represents a potential energy gradient that pulls the electron and hole wave functions apart and hence increases the exciton decay time which is proportional to the wave function overlap. When the carrier wave function overlap is equal to zero at all times the decay time essentially becomes infinitely long. In the earlier data in section 5.2 we could observe a luminescence

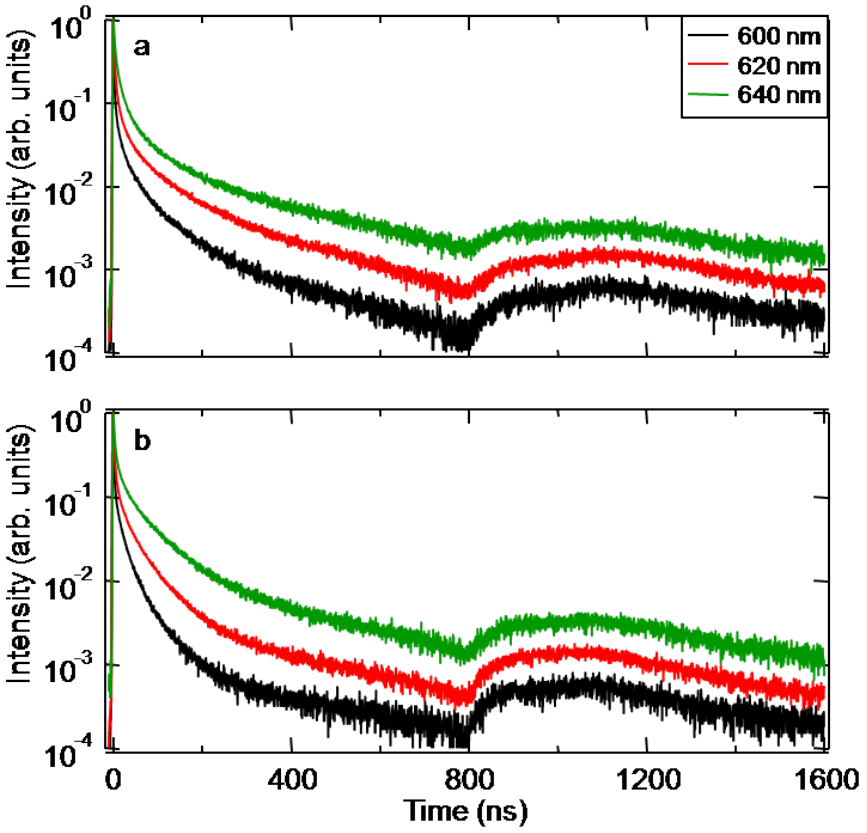

FIGURE 5.11: The luminescence decay of the investigated NRs is shown for different sections of the NR luminescence spectrum with an electric field pulse applied until 800 ns after the onset of the decay a) without a magnetic field and b) with a magnetic field of $B = 8\ T$ applied.

quenching in the decay curves. This is due to the part of the excitons, for NRs aligned suitably in the electric field, that are separated by the electric field for longer than the recorded decay window lasts. By applying a constant electric field to the NR sample and switching off the field during the duration of the luminescence decay recorded we can retrieve these excitons as can be seen in figure 5.11. We show luminescence decays for $B = 0\ T$ in figure 5.11a and for $B = 8\ T$ in figure 5.11b for all three wavelength ranges we investigated. The voltage we applied during the duration of the pulse was $U = 100\ V$. After 800 ns of the luminescence decay we switched off the electric field. This could accurately be controlled using a delay generator (*DG535* from Stanford Research Systems) to trigger both the card for the time correlated single photon counting (*SPC140* from Becker & Hickl GmbH) and the pulse generator (*AV-1011B1-B* from Avtech Electrosystems Ltd.). The delay generator allowed for convenient shifting of the relative start and stop times of the TCSPC detection window and the voltage pulse duration

to achieve an adequate time overlap. It can clearly be seen that when the electric field on the capacitor sample is switched off the luminescence intensity starts to rise again as the formerly separated carriers are drawn together by the electrostatic interaction. The rise of the luminescence after the voltage pulse happens on a time scale of $\approx 50\ ns$ which is much longer than any microscopic processes that occur in the $CdSe/CdS$-NR and is attributed to the discharging of the capacitor sample as the fall time of the pulse generator is $t_{fall} \leq 2\ ns$. The recuperation of excitons is the same for the three different NR sizes because the variation in NR length is too small to show a significant difference in the delayed luminescence decays. As already seen in section 5.2 the application of a magnetic field does not change the electronic field effect for the reasons illustrated in section 5.2.

In order to verify if this assertion is true we directly compare the luminescence decay of each respective spectral region we investigated for the cases of zero magnetic field and $B = 8\ T$ applied. In figure 5.12a, b and c we plot the results for the spectral regions 600 nm, 620 nm and 640 nm respectively. The luminescence decays for all three different size distributions of $CdSe/CdS$-NR proceed in the same manner as they would under the influence of a magnetic field (compare figure 4.9a, b, c) before the electric field is switched off after 800 ns with the exception that the quenching of the electric field accelerates the luminescence decay. After the electric field is switched of the luminescence decay curve starts rising again because of the recuperated excitons. Although the luminescence decays for $B = 0\ T$ and $B = 8\ T$ are very different from each other during the length of the electric field pulse applied, when the electric field is switched off however the luminescence decays for $B = 0\ T$ and $B = 8\ T$ behave in a same manner. It is not clear if this is a real physical effect or due to the poor statistics of the luminescence decay at such late times. However there is no reason to believe that the excitons after being released from the electric field would not resume to behave in the manner we have described in chapter 4 and so we are inclined to assume that the seemingly parallel luminescence decay in figure 5.12 after the voltage pulse is due to the poor signal to noise ratio.

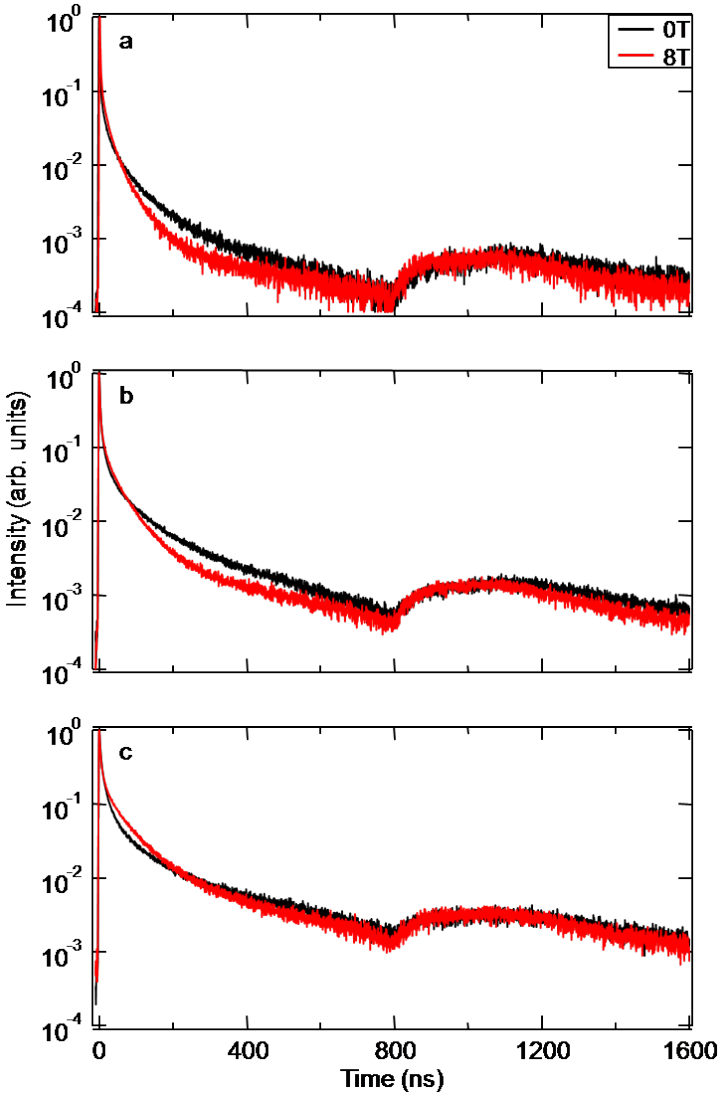

FIGURE 5.12: a), b) and c) show the NR's luminescence decay with an electric field pulse applied until 800 ns after the onset of the decay without magnetic field (black) and with external magnetic field $B = 8\ T$ (red) applied for the three spectrally selected CdS-core radii of 1.8 nm, 2 nm and 2.2 nm respectively.

In this chapter we have described the findings of the numerical calculations of the electron and hole wave functions under the application of an external electric field. We have further described how this influences the excitonic fine structure in the heterostructured $CdSe/CdS$-NR. After that we discussed the results of the time resolved spectroscopic measurements and explained the quenching mechanism of the electric field on the sample. Finally we have demonstrated that by applying an electric field pulse the electrically quenched excitons can be regained by switching off the electric pulse during the luminescence decay.

Chapter 6

Hetero dimensional fluorescence resonance energy transfer

Ever since their invention in the early 1980's [15; 16] colloidal NCs have attracted massive interest in the scientific community because of their excellent emission tunability, high quantum yield, low cost synthesis and easy processability [22; 9; 139]. However the injection of carriers into colloidal NCs always posed a problem. This is mainly due to the surface passivation using organic molecules with very low electron mobility. These passivating molecules help to increase the NC's quantum efficiency and long term stability. In this chapter we present the work we performed to explore the possibility to contact-free inject carriers into colloidal NCs.

It has recently been proposed to use FRET in order to inject carriers into colloidal NCs using an electrically contactable QW [58; 59] and experimental work has confirmed this effect [61; 62]. This process has been shown to be highly dependent on the exciton localisation in the donor and on the distance between donor and acceptor (see 2.2). In the work presented here we vary those two parameters in hybrid QW-NC samples.

6.1 Hybrid energy transfer samples

For our investigation we used $InGaN/GaN$ single QW samples that were grown using metal organic chemical vapor deposition at the University of Strathclyde [85; 140]. The samples all have a QW thickness of 2.5 ± 0.5 nm to feature an emission in the near ultraviolet region. We used three different QW samples that are distinguished only in their capping layer thickness (see figure 6.1 a). The capping layer, similar as in

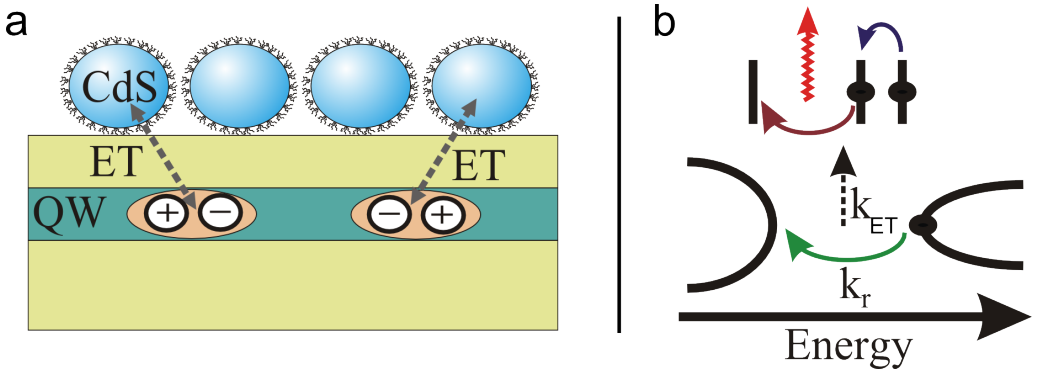

FIGURE 6.1: a) shows a schematic of the investigated samples with CdS-NC drop cast on top of the capping layer of the QW samples. b) shows a Jablonski diagram of the FRET process between a QW and an NC.

the shell material of colloidal NCs, provides finite potential confinement, passivation of the surface and prevents oxidation of the QW. Especially in the case of the $InGaN$ QW under investigation oxidation can pose a serious problem as the QW material is an alloy and without proper surface passivation this can easily oxidise. The capping layer thicknesses of the samples as well as the QW thickness have been measured post-manufacture using a Rutherford backscattering spectrometer. We used capping layers of 1.9 ± 0.5 nm, 3.2 ± 0.5 nm and 11.8 ± 0.5 nm thickness. This allows one to investigate energy transfer at donor-acceptor separations below, comparable with and above the Förster radius.

On top of the capping layer we deposited CdS-NCs. These were brought on via drop casting of a concentrated colloid, and subsequent drying on the capping layer. This produced a thick, closely-packed highly absorbing layer of CdS-NCs (see figure 6.1 a). The CdS-NC were synthesised using the procedure illustrated in [141; 71] with the single difference that an oleic acid:CdO ratio of $19:1$ was used.

In figure 6.2 the emission spectra of the QW sample with a capping layer thickness of $3.2 \pm 0.5\ nm$ is shown before deposition of the NCs (solid black line) and after a layer of NCs had been deposited (dotted black line). The former as well as the latter feature phonon replicas on the lower energy side of the spectra, however the latter alone shows a clear NC emission at around 460 nm. The QW emission for all three different capping

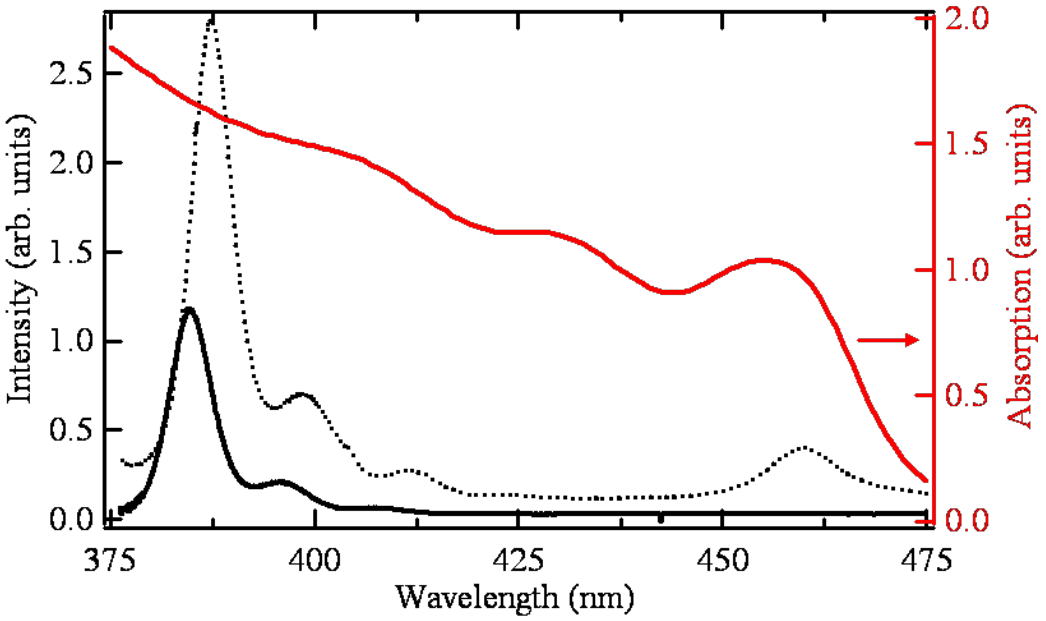

FIGURE 6.2: The emission spectrum of the bare QW sample (black continuous line) and the QW sample with the NCs (black dotted line). The latter clearly shows NC emission that is Stokes shifted from the NC absorption (red line).

layer thicknesses is centred around $387 \pm 5\ nm$. This short wavelength emission allows us to choose CdS as the semiconductor material for the colloidal NCs used. CdS is a wide band gap semiconductor and features both a smoothly varying density of states at the QW emission and an emission wavelength not far from the QW emission in order not to lose excitons to non radiative decay channels when relaxing to an optically active state [142; 143; 144] (see step 4 in figure 2.6). In figure 6.2 the absorption spectrum of the CdS-NCs is displayed (solid red line) together with the QW emission. On the low energy side the first and second exciton level can clearly be discerned. At the wavelength of the QW emission however the NC absorption is smooth. This indicates that the absorbing excitonic levels at that energy are so close together that they form a quasi-continuum of states. This assures the microscopic overlap condition for energy transfer to be satisfied in a maximum number of NCs (see 2.2).

6.2 Temperature dependence of exciton transfer in QW-NC hybrid structures

The QW samples (see chapter 6.1) were mounted on the cold finger of a closed cycle cryostat. This works following the principle a commercial fridge uses. It compresses

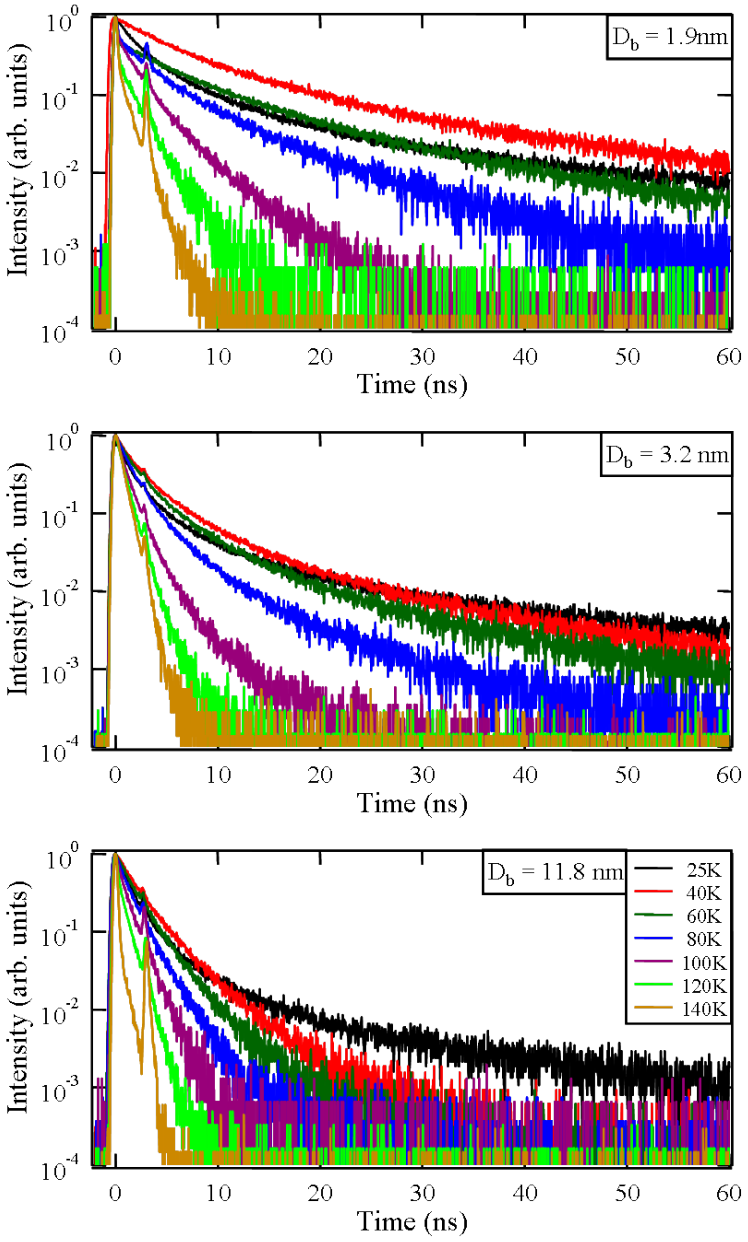

FIGURE 6.3: The fluorescence decay of the three bare QW samples with different capping layer thicknesses for increasing temperature.

a refrigerant, in this case Helium, then transports the compressed gas to an expansion chamber that is connected to the cryo-space. Upon re-expansion the gas rapidly cools

and hence cools down the cryo-space as well. A thermocouple was mounted inside the cold finger to enable us to monitor the actual sample temperature. Using this device we were able to accurately control the sample temperature in the range from 25 K up to room temperature. Optical excitation of the quantum wells was provided by an OPA laser system pumped by a RegA (see chapter 3.1.1). The OPA was tuned to emit laser light with a wavelength of 730 nm that then was coupled through another non-linear crystal in order to produce the second harmonic that peaked at 365 nm. The inherent limitations of the laser system prevented us from tuning the OPA to a shorter emission wavelength. For this reason it was difficult to separate the excitation light from the sample emission. Figure 6.3 shows a series of decay curves that were recorded from the bare QW samples at different temperatures using TCSPC (see chapter 3.1.2). Decays at more temperature values than shown have been recorded but are omitted in the figure for clarity reasons. A monochromator was used to separate the QW emission from the excitation light and from the NC emission in the composite samples. However, the excitation light was spectrally very close to the QW emission and so some stray light was detected as well and can be seen in figure 6.3 in some curves as a second peak after around 3 ns. It can be observed that the decay curves deviate from perfect single exponential behaviour which would be the case for an isolated two level system. This results from fluctuations in the QW confinement potential. This is expected from a thin alloy QW as it does not grow completely homogeneously but will form small domains of the different constituents. Because of the statistical nature of the TCSPC method each decay curve is made up of single photons from many subsequent excitations. These photons come from different points within the laser spot on the sample and so variations in the confinement potential are reflected in the non-mono exponential decays. As the temperature increases this effect becomes less dominant because additional thermal energy lifts the excitons above the confinement potential fluctuations. In addition we can observe from figure 6.3 that with increasing temperature the fluorescence decay becomes at first slower and as the temperature passes 40 K it starts to become faster again. This non-monotonous behaviour of the fluorescence decay is influenced at lower temperatures ($25\ K - 40\ K$) by the increase in thermal energy that elevates the excitons above the potential fluctuations and then at higher temperatures by non-radiative decay channels

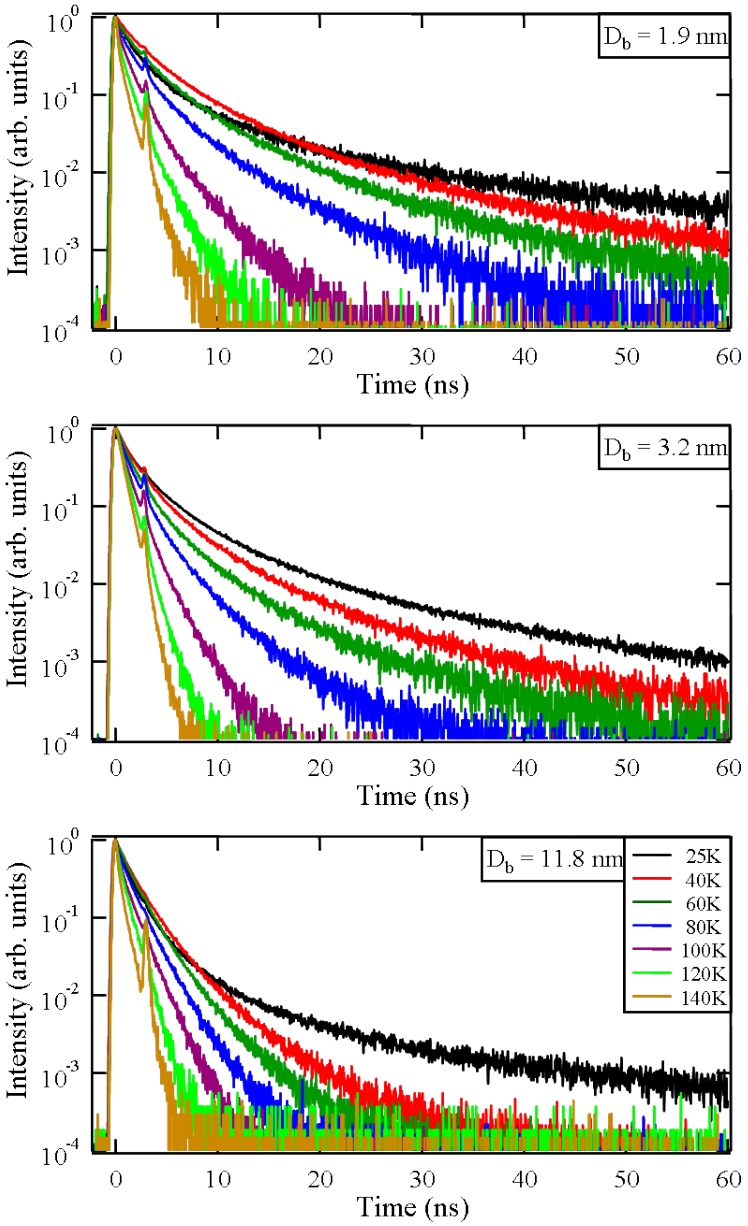

FIGURE 6.4: The fluorescence decay of the three QW samples with different capping layer thicknesses and *CdS*-NCs drop cast on top of them for increasing temperature.

that start to dominate the decay. At very high temperatures ($> 140\ K$) the decays are governed completely by these non-radiative decay channels. It is evident from figure 6.3 that the fluorescence decay becomes faster with increasing barrier thickness D_b and this holds true for all temperatures. In the samples with the thin barrier the confinement of excitons is not very homogeneous and carriers can get trapped at confinement potential fluctuations or leak out of the QW. This multitude of effects decreases the exciton coherence volume and hence lengthens the fluorescence decay. For the sample with the

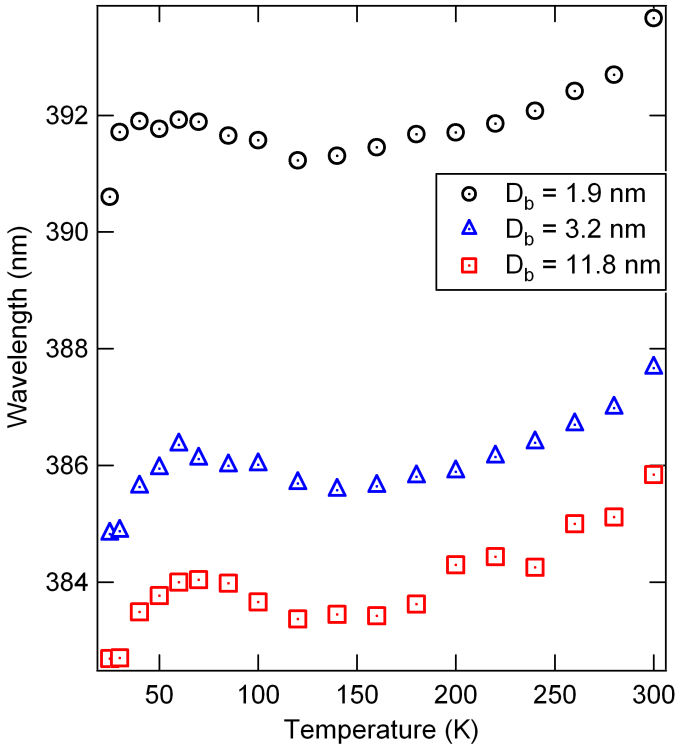

FIGURE 6.5: The temperature induced emission wavelength shift is shown for the three QW samples with different capping layer thickness.

thick barrier on the other hand the confinement is much more homogeneous and interfacial effects are greatly reduced. In figure 6.4 one can see the equivalent temperature dependences for the QW emission after a layer of NC has been deposited on top of the samples. It is clear from simple comparison that the QW's fluorescence decays become faster in the vicinity of a highly absorbing layer of NC.

An additional influence of the random potential and the thermal energy can be seen at the spectral positions of the QW emission which undergo a significant wavelength shift with temperature. The decays shown in figures 6.3 and 6.4 were always taken at the wavelength of the maximum of the QW emission spectrum at the respective temperatures. In figure 6.5 the spectral positions of these maxima are plotted versus temperature for all three barrier thicknesses. Independent of temperature the emission wavelength is highest for the QW with the thin barrier and it moves to shorter wavelengths with increasing barrier thickness. This effect is understood as a consequence of the leaking of the exciton wave function out of the QW through the passivating barrier layer. The amplitude of the exciton wave function decreases exponentially with penetration depth

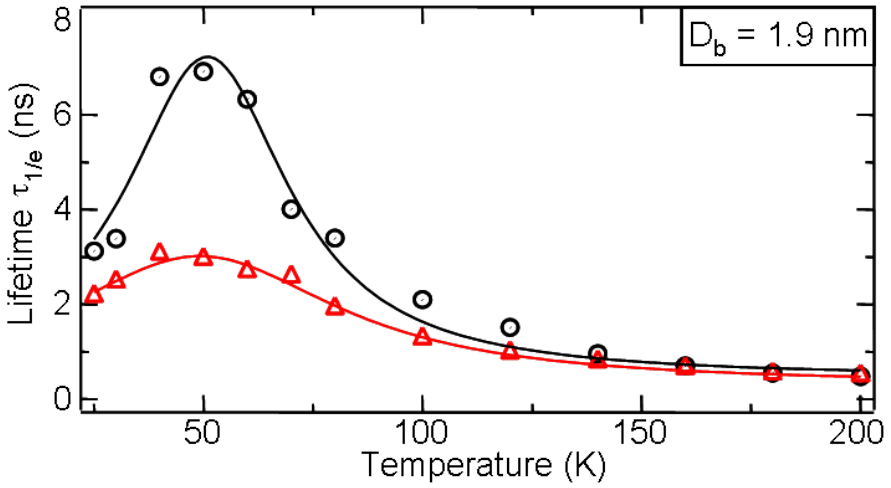

FIGURE 6.6: The decay time of the QW fluorescence decay is displayed over temperature for the bare QW (black open circles) and the QW with NC (red open triangles) sample with a 1.9 nm thick capping layer.

into the barrier and hence leaking of excitons out of the QW does have less influence in QW with thicker barriers. Apart from the inherent shift in emission energy between the different QW samples one can observe in figure 6.5 that the emission maximum changes in the same way with temperature for the three different samples. The non-monotonous change of the fluorescence spectra with increasing thermal energy is attributed to an increase in delocalisation of the QW excitons. At very low temperatures the excitons are frozen out at randomly distributed locally confining potential minima due to the lack of thermal energy. This localisation increases the kinetic energy of the exciton in the same way as quantum confinement does. As the temperature increases the system gains thermal energy and hence the excitons get increasingly delocalised. This increase in the exciton coherence volume decreases their kinetic energy and hence the emitted light shifts to higher wavelength. As the temperature increases even further localisation effects become weak and the shift to higher wavelengths for $T > 150\ K$ in figure 6.5 can be attributed to the change of the band gap with temperature.

In order to quantitatively compare the different decays from figures 6.3 and 6.4 we extracted the decay times τ_{QW} for the bare QW and τ_H for the hybrid structure. We decided to use the so called $1/e$-time for this purpose which is the length of the time period after the onset of the decay after which the fluorescence intensity decreased by a factor of $1/e$, with e being Euler's number, compared to its initial intensity. This

choice of decay time is justified by the fact that the distribution of decay times changes strongly with temperature and barrier thickness. This makes it difficult to use one fitting function consistently for all decays. In figure 6.6 the decay time versus temperature is plotted for the bare QW sample (black open circles) and the hybrid structure (red open triangles) for the thinnest barrier width investigated. At low temperatures, between 25 K and 50 K, τ_{QW} is increasing with temperature, which suggests that within this temperature range exciton recombination in the QW is dominated by radiative channels (increasing exciton coherence volume). As the temperature is increased fur-

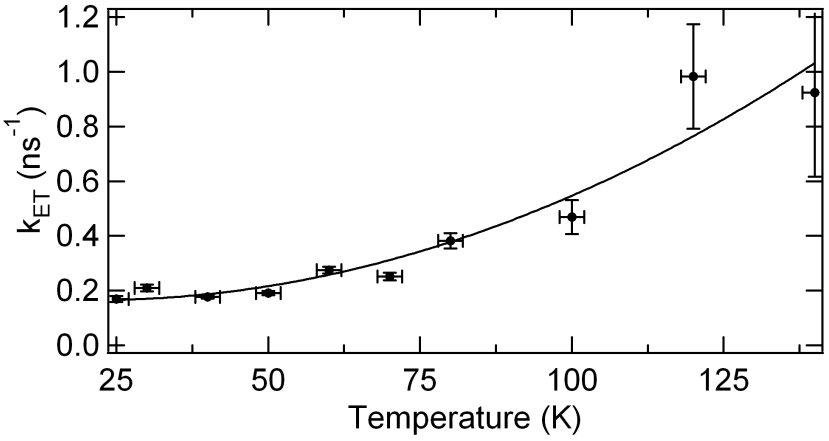

FIGURE 6.7: The energy transfer rate between the QW sample with a 1.9 nm thick capping layer and the CdS-NC is displayed over temperature.

ther, the fluorescence decay acquires an increasingly non-radiative character and τ_{QW} decreases again. Comparing the fluorescence decay of the bare QW samples and the hybrid structure shows that for the thin barrier $D_b = 1.9\ nm$ the dependence of the decay time of the hybrid structure is following a similar trend to the case of the bare QW. However τ_H does not change as rapidly in the hybrid structure in the temperature range of $25\ K - 80\ K$. This shows that the FRET process in the hybrid structure is not primarily affected by the exciton coherence volume in the quantum well but as we will argue by the exciton localisation due to the QW potential disorder. It has been shown earlier, that in thin $InGaN/GaN$ single QW the intrinsic recombination dynamics are governed by the electron-hole pair localisation [145]. The localisation of the exciton on the confinement potential disorder can influence the dimensionality of the exciton from pointlike dipoles, this is the case when the localisation length is smaller than the exciton

Bohr radius $L < a_B$, to free excitons that occur in an ideal QW. With increasing thermal energy the degree of exciton localisation becomes reduced by elevating the carriers above the QW potential disorder, thereby the energy transfer rate is increasing due to the reduced exciton localisation, for localisation lengths that are small compared to the donor-acceptor distance. This dependence can be seen in figure 6.7 where we plotted the energy transfer rate over temperature. The transfer rate was calculated using the fluorescence decay rates of the bare QW k_{QW} and the hybrid structure k_H following the formula: $k_H = k_{QW} + k_{ET}$. For temperatures $T > 140\ K$ the recombination dynamics are dominated by non-radiative decay channels intrinsic to the QW that obscure the dynamics of the energy transfer. The optimum pumping efficiency of NC via energy transfer from a QW is obtained at 60 K, with $\eta_{ET} = 65\%$, where $\eta_{ET} = \frac{k_{ET}}{k_{ET}+k_{QW}}$.

6.3 Donor-acceptor separation dependence in hetero dimensional energy transfer

In section 6.2 we described how the FRET between a QW and a layer of semiconductor NCs depends on exciton localisation in the donor. In this section we will present how this effect scales with the donor-acceptor separation distance R. In figure 6.8 the decay time for the bare QW (black open circles) and the hybrid structure (red open triangles) is plotted over temperature for the QW with the barrier widths $D_b = 3.2\ nm$ and $D_b = 11.8\ nm$. The data for τ_{QW} and τ_H for the sample with $D_b = 11.9\ nm$ breaks off at $T = 140\ K$ because for temperatures higher than 140 K the fluorescence decays became too fast to reliably extract a decay time $\tau_{1/e}$. The decay time τ_{QW} for the sample with $D_b = 3.2\ nm$ (see figure 6.8 a) follows the same trend as has been observed for the sample with $D_b = 1.9\ nm$ (see figure 6.6). Hence we can conclude that at low temperatures ($25\ K - 50\ K$) the fluorescence decay is governed by radiative recombination of the QW exciton and at higher temperatures non-radiative decay channels take over the emission. However the curve of τ_H over temperature does not follow the same trend as observed earlier (see figure 6.6). We can however again associate this behaviour with the degree of exciton localisation in the QW. As shown in chapter 2.2.2 the rate of energy transfer does critically depend on the dimensionality of the donor

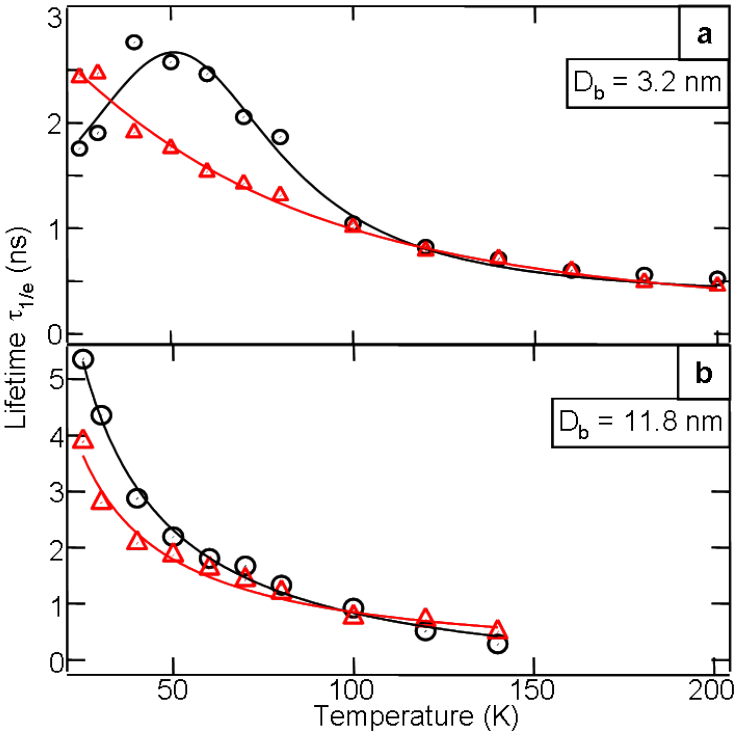

FIGURE 6.8: The decay time of the QW fluorescence decay is displayed over temperature for the bare QW (black open circles) and the QW with NC (red open triangles) sample with a) a 3.2 nm and b) a 11.8 nm thick capping layer.

dipole. For the sample with $D_b = 1.9\ nm$ we have shown that the exciton is strongly localised for very low temperatures and as the temperature increases the exciton localisation decreases. The QW with $D_b = 3.2\ nm$ however features less random potential disorder at which the exciton wave function can get localised. The excitons' centre of mass motion wave function in this sample can be described as a plane wave. This is the case of a free exciton and the energy transfer rate has an exponential dependence on the donor-acceptor separation (see chapter 2.2.2). This exponential relation is much more effective in suppressing the inherent decay behaviour of the QW exciton than the R^{-4} dependence for localised excitons. Therefore the plot of τ_H against temperature does not show the non-monotonous characteristic of τ_{QW} (see figures 6.6 and 6.8 a). If the barrier width is increased even more ($D_b = 11.8\ nm$ in figure 6.8 b) the recombination dynamics observed for the two thinner barriers vanishes completely. The barrier with $D_b = 11.8\ nm$ provides, contrary to the two samples with thinner barriers, a smooth enough confinement potential, that even at temperatures as low as $T = 25\ K$ the available thermal energy is enough to lift the excitons above the random potential disorder.

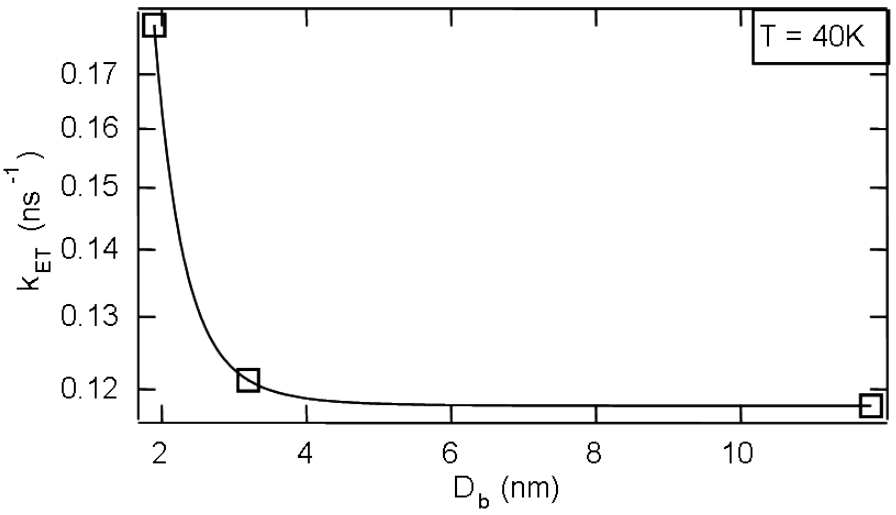

FIGURE 6.9: The energy transfer rate for the three different capping layer thicknesses is shown.

The $\frac{d\tau_{QW}}{dT} < 0$ behaviour of the fluorescence decay indicates that the exciton coherence volume is thermally limited for low temperatures. For temperatures $> 50\ K$ the slope of the curve decreases which marks the point where increasingly non radiative channels are dominating the fluorescence decay. The behaviour of τ_H follows the same trend as τ_{QW}, only at low temperatures $T < 40\ K$ can a slight increase in the decay time compared with the bare QW be observed. This is due to the fact that the energy transfer at a donor-acceptor separation of $R = D_b = 11.8\ nm$ only plays a minor role and can only have an impact on the decay time when not rivalled by fast non-radiative relaxation channels.

Due to the different degrees of exciton localisation in the three samples we investigated it is difficult to fit an unambiguous formula for the energy transfer rate to the separation dependence. In figure 6.9 we show the energy transfer rate for the three different donor-acceptor separations at $T = 40\ K$. We fitted a power law to the data and extracted a dependence of $\frac{1}{\tau_{ET}} \propto R^{-5.5}$. This deviates strongly from the expected R^{-4} dependence for localised excitons in QW. This divergence from the theory can be attributed to the different degrees of exciton localisation in the studied QW samples. The dependence of the transfer time on D_b is not shown for any other temperature because the divergence from theory is even stronger in those cases.

In this chapter we have described the hybrid QW-NC samples with a range of separation distances to probe the distance dependence of FRET in these structures. Integrated and time resolved fluorescence data has been shown to exemplify the effect of the FRET on the QW fluorescence at different temperatures. A non-monotonic wavelength shift in the QW samples could be attributed to the exciton localisation. This localisation at the confinement potential disorder could be observed in the fluorescence lifetime of the bare QW and the hybrid structure with short separation distance. Different dependences of the exciton lifetime have been observed for different separation distances and therefore no conclusive separation dependence of the FRET process could be shown.

Chapter 7

Conclusions

In this thesis, time integrated and time resolved spectroscopic studies of excitons in heterostructured colloidal $CdSe/CdS$ nanorods under the influence of external magnetic and electric fields were presented. Time integrated spectra have shown that an external magnetic field induces a diamagnetic shift of the same order of magnitude as in bulk crystals which was attributed to the expansion of the electron over the whole nanorod. A semi-numerical approach to solving the exciton fine structure in colloidal nanocrystals was presented and justified by comparison with analytical calculations. This method was used to calculate the exciton fine structure of nanorods providing heterodimensional confinement for electron and hole. Time and polarisation resolved measurements of the exciton dynamic in Faraday and Voigt geometry allowed to distinguish between the Zeeman effect and the magnetic field induced spin admixture of bright and dark states in colloidal nanorods for the first time.

Heterodimensional confinement of the electron and hole allowed for manipulation of their wave function overlap by application of an external electric field. Numerical methods have been used to calculate the wave function overlap, the electron and hole energy as well as the exciton fine structure in dependence of the electric field strength. Time resolved spectroscopic measurements have shown that overall a quenching of the luminescence in nanorod ensembles is achieved by application of an electric field. This quenching process however was shown to be reversible for up to 800 ns after the onset of the luminescence by turning off the electric field applied to the ensemble.

Fluorescence resonant energy transfer between an $InGaN$ quantum well and colloidal CdS nanocrystals has been investigated. The temperature dependence of this process revealed a change of the exciton dimensionality within the quantum well induce by thermal energy. This change was shown to influence the energy transfer rate to the colloidal nanocrystals over a temperature range from 25 K to $\approx$ 140 K. Three different capping layer thicknesses of the quantum well have been used to explore the dependence of energy transfer rate on the donor-acceptor separation R. This dependence however has been demonstrated to be dominated by the change in exciton confinement induced by the different degrees of quantum well passivation which made it difficult to observe the predicted R^{-4} dependence. A maximum transfer efficiency of $\eta_{ET} = 60\%$ has been obtained.

Future work

Following the work presented in chapter 4 a high resolution spectroscopic investigation of single heterostructured $CdSe/CdS$ nanorods in external magnetic fields can give direct access to the excitonic fine structure levels and allows comparison to the calculated results. Single particle experiments with colloidal nanoparticles are performed by strongly diluting the colloidal solution and bringing the obtained colloid onto a very clean substrate with a very small fluorescence of its own. Nevertheless this does not allow one to actively orient the nanocrystal which is needed to produce unambiguous results with magnetic fields. For alignment a suitably cleaved epitaxial substrate [146], a liquid crystal [147; 148], a polymer matrix [149] or an optical trap could be used. However all these methods can make it difficult to provide for single particle separation. A further challenge would be the macroscopic orientation of the microscopically aligned nanorods within an external magnetic field. In the optical detection system polarisation elements will need to be introduced to verify the polarisations of the fine structure states. Performing the single particle experiment within a strong magnetic field will provide considerable challenges for the detection system that can be solved by using a fibre coupled detection scheme [47].

Additionally the possibility of applying an external electric field to the aligned nanorods

could open up a highly versatile means of actively manipulating the electron and hole wave functions in a single heterostructured $CdSe/CdS$ nanorod. This would allow one to investigate the influence of an electric field on the Zeeman split fine structure levels directly. More than that, by applying an electric field pulse rather than a constant electric field the magnetic field effects on separated electrons and holes can be studied upon release of the electric field potential gradient. Because of their strong separation electron and hole for this case can not be seen as bound pairs or excitons but rather are two separate particles. This could provide a tool to directly investigate electron and hole separately in these nanorods.

Further investigations regarding fluorescence resonant energy transfer can be performed by employing different species of donors and acceptors. Instead of changing the dimensionality of the donor exciton by changing the temperature of the containing quantum well, nanostructures that inherently possess a certain geometry that favours specific shapes of exciton coherence volumes could be used. Nanowires which provide 1 dimensionally elongated excitons or tetrapods that allow the exciton to diffuse into their four elongated arms could be used together with ideal 0 dimensional nanocrystals.

Appendix A

MATLAB code for the numerical calculation of the exciton parameters in heterostructured NR

The numerical algorithm for the solution of the extended effective mass model was implemented in the finite element software FemLab®. This is a very complex software and a detailed description of all the steps of the algorithm and the associated commands is beyond the scope of this work. All the used functions are well documented in the manual of the software and we will concentrate on giving an overview of the algorithm used and the major functions employed.

The algorithm we used requires the solution of 4 differential equations (the Schrödinger and the Poisson equation for both electron and hole) over a common geometry. For this case FemLab® offers the so called multiphysics concept. Within this concept a geometry is defined over which then a number of varying differential equations with different material constants can be solved. Because FemLab® does not offer the possibility to iteratively solve this problem within the software itself we used a script in MATLAB® to control FemLab® remotely and implement an iterative solution. In addition this

allows to automatically vary several parameters over a range of values and output the generated data into a file for further analysis. This is particularly useful given the fact that a single calculation for one set of parameters can take several minutes to finish.

The algorithm we used calculates the energy eigenvalues for electron and hole, their wave function overlap and their wave functions in 2-dimensional cylinder coordinates over a half cross section along the length of the heterostructured $CdSe/CdS$-NR. For this we transformed the equations 3.2, 3.3 and 3.4 into cylinder coordinates. This dimensional reduction of the problem improves the time needed greatly and no loss in accuracy is incurred. By using this the parameter space can be extended which permits us to investigate external fields and band gap differences between the core and shell materials.
The main functions of the algorithm were implemented in a single MATLAB® function:

```
function [Chi, EElec, EHole, EExc, Ovl, femE, femH] = ...
CalNanorodsJosef_OvlvsEfield(Rad, AR, LBOffset, NbrIter, Efield)
```

In this function we enter the values of the radius of the $CdSe$-core (`Rad`), the aspect ratio of the NR (`AR`), the potential difference of the conduction band of $CdSe$ and CdS (`LBOffset`), the external electric field applied (`Efield`) and the number of iterations (`NbrIter`). The function outputs as solutions the short range exchange interaction (`Chi`), the energies for electron, hole and exciton (`EElec, EHole, EExc`), the wave function overlap (`Ovl`) and the complete solution of the electron and hole wave functions in FemLab® data structure (`femE, femH`).
Within this main function 4 sub-functions are called:

- `MakeGeom`

  Creation of the 2-dimensional geometry over which the problem is solved.

- `SetMaterConst`

  Define the material constants.

- `SetEquations` Implementation of the Schrödinger and Poisson equations for electron and hole.

- `SolveEqu`

  Iterative solution of the extended effective mass model.

This script is very versatile and can easily be changed to accommodate for additional potentials or surface charges on the NR. These changes can be implemented in the sub-function `SetEquations`.

In the following we present the MATLAB® script we used:

```
function [Chi, EElec, EHole, EExc, Ovl, femE, femH] = CalNanorodsJosef_...
        OvlvsEfield(Rad, AR, LBOffset, Efield, NbrIter)
  % CalNanorods: Extended effective mass model (EeMm)
  % Parameter: Rad: Radius of the CdSe-core
  %            AR: Aspectratio of the nanorod
  %            LBOffset: Conduction band offset
  %            NbrIter: Number of iterations for the EeMm
  % Return:    EElec: Energy eigenvalue electron
  %            EHole: Energy eigenvalue hole
  %            Ovl: Wavefunction overlapp
  %            femE: FemLab-solution for the electron
  %            femH: FemLab-solution for the hole

  global fem % FemLab structure
  global withShell % = 0, if no CdS shell around the core, 1 else
  flclear fem % Delete any existing former solutions

  % Calcualtion of the thickness of the CdS-shell around the core.
  % The scaling factor 0.09816 was taken from TEM images.

  fid = fopen('D:\rohrm docs\thesis\Figures\EBfields\OvlvsEfield\
          params.txt', 'wt');
  for k= 0.075 : 0.001 : Efield
```

```
    Shell = (AR - 1) * 0.09816;% * k;
    Length = AR*Rad*2;
    BandGapDiff = 0.78; % Difference in bandgap for CdSe and CdS
    Bang = 1.68;

    MakeGeom(Rad, Rad+Shell, Length); % Draw the geometry
    SetMaterConst(LBOffset, withShell, k); % Set material constants
    SetEquations; % Set the differential equations

    % Calculate the solution
    [Chi, EElec, EHole, EExc, Ovl, femE, femH] = SolveEqu(Rad, Bang,...
     NbrIter);

    %Write Efield, overlap and EExc
    fprintf(fid, '%2.4d %6.8d %6.8d %6.8d %6.8d %6.8d\n', k, Ovl,
    % Chi, EHole, EElec, EExc);
  end
  fclose(fid)
end

function MakeGeom(CoreR, ShellR, Length)
  % MakeGeom creates the geometry
  % Parameter: CoreR: Diameter of the CdSe core
  %            ShellR: Radius of the CdS shell
  %            Length: Length of the nanorod

  global fem
  global withShell % Saves, wether or not there's a CdS shell
  % around the core

  withShell = (CoreR == ShellR);
```

```
  CdS = DrawHalfRod(ShellR, Length);
  CdSe = DrawHalfCircle(CoreR);

  clear s
  s.objs={CdS,CdSe};
  fem.draw=struct('s',s);
  fem.geom=geomcsg(fem);

  function HalfCirc = DrawHalfCircle(rad)
    tmpCirc=ellip2(1,1,'base','center','pos',[0,0]);
    tmpRect=rect2(2,4,'base','corner','pos',[-2,-2]);
    HalfCirc = geomcomp({tmpCirc,tmpRect},'ns',{'tmpCirc','tmpRect'},...
                                                                    ',
    HalfCirc = scale(HalfCirc, rad, rad, 0, 0);
  end

  function g = DrawHalfRod(rad, leng)
    g1=rect2(rad,leng,'base','corner','pos',[0,-rad]);
    g = fillet(g1,'radii',rad,'point',[2,3]);
  end
end

function SetMaterConst(BandEdge, noShell, Elecf)
  % SetMaterConst sets the material and scaling constants
  %
  % Parameter: BandEdge: Band edge difference between CdSe and CdS
  %            AR: Aspectratio of the nanorods

  global fem
```

```
% Initialising and creating the mesh
  fem.mesh = meshinit(fem);

% Set the material constants

  fem.const={'hq','1.054573E-34','me','9.10939E-31','sch_coeff',...
             'hq^2/(2*me*1E-18*qe)','Bandgap','0.78','qe',...
             '1.6021773E-19','eps0','8.8542E-12','poi_coeff',...
             '1E9/eps0','pi','3.141592654'};%,'Ey','k'}; can be...


  clear equ;
  equ.ind = [1,2];
  equ.dim = {'u_elec','u_hole','v_elec','v_hole'};

  if (noShell)
      equ.expr = {'mElec',{0.13,0.2},'mHole',{0.45,0.7},'VElec',...
                  {0, BandEdge},'VHole',{0, 'Bandgap - VElec'},...
                  'epsmat',5.8,'Ey',Elecf};
  else
      equ.expr = {'mElec',{0.2,0.13},'mHole',{0.7,0.45},...
                   'VElec',{BandEdge,0},'VHole',{'Bandgap - VElec',...
                    0},'epsmat',5.8,'Ey',Elecf};
  end
  fem.equ = equ;

% Sets the scaling conditions
  fem.expr = {'u_elec_norm','u_elec/sqrt(Int_u_elec)','u_hole_norm',...
              'u_hole/sqrt(Int_u_hole)','rho_elec','u_elec_norm^2*qe',...
              'rho_hole','u_hole_norm^2*qe','VElec_ges',...
              'VElec-v_hole+y*Ey','VHole_ges','VHole-v_elec-y*Ey'};
```

```
    clear elem
    elem{1} = struct('elem',{'elcplscalar'},'var',{{'Int_u_elec',...
     'Int_u_hole'}},'g',{{'1'}},'src',{{{{},{},struct('expr',...
     {{{'2*pi*x*u_elec^2'},{'2*pi*x*u_hole^2'}}},'ipoints',{{{'4'},...
     {'4'}}},'ind',{{{'1','2'}}})}}},'geomdim',{{{}}},'global',{{'1','2'}});

    fem.elemcpl = elem;
end

function SetEquations
  % SetEquations sets the differential equations and the boundary conditions

  global fem
  global withShell

  if withShell
      brd = [2,2,1,1,1,1];
  else
      brd = [2,2,2,1,1,1,1,1];
  end

  % Application mode 1: Schrdinger equation for the electron
    clear appl
    appl.mode.class = 'FlPDEC';
    appl.dim = {'u_elec','u_elec_t'};
    appl.name = 'SchroedElec';
    appl.assignsuffix = '_SchroedElec';
    clear bnd
    bnd.type = {'dir','neu'};
    bnd.ind = brd;
    appl.bnd = bnd;
```

```
clear equ
equ.c = 'x*sch_coeff/mElec';
equ.a = 'x*VElec_ges';
equ.f = 0;
equ.da = 'x';
equ.ind = [1,1];
appl.equ = equ;
fem.appl{1} = appl;

% Application mode 2: Schrdinger equation for the hole
clear appl
appl.mode.class = 'FlPDEC';
appl.dim = {'u_hole','u_hole_t'};
appl.name = 'SchroedHole';
appl.assignsuffix = '_SchroedHole';
clear prop
prop.weakconstr=struct('value',{'off'},'dim',{{'lm3','lm4'}});
appl.prop = prop;
clear bnd
bnd.type = {'dir','neu'};
bnd.ind = brd;
appl.bnd = bnd;
clear equ
equ.c = 'x*sch_coeff/mHole';
equ.a = 'x*VHole_ges';
equ.f = 0;
equ.da = 'x';
equ.ind = [1,1];
appl.equ = equ;
fem.appl{2} = appl;
```

```
% Application mode 3: Poisson equation for the electron
  clear appl
  appl.mode.class = 'FlPDEC';
  appl.dim = {'v_elec','v_elec_t'};
  appl.name = 'PoiElec';
  appl.assignsuffix = '_PoiElec';
  clear prop
  prop.weakconstr=struct('value',{'off'},'dim',{{'lm5','lm6'}});
  appl.prop = prop;
  clear bnd
  bnd.type = {'dir','neu'};
  bnd.ind = brd;
  appl.bnd = bnd;
  clear equ
  equ.c = 'x*epsmat';
  equ.f = 'x*rho_elec*poi_coeff';
  equ.ind = [1,1];
  appl.equ = equ;
  fem.appl{3} = appl;

% Application mode 4: Poisson equation for the hole
  clear appl
  appl.mode.class = 'FlPDEC';
  appl.dim = {'v_hole','v_hole_t'};
  appl.name = 'PoiHole';
  appl.assignsuffix = '_PoiHole';
  clear prop
  prop.weakconstr=struct('value',{'off'},'dim',{{'lm7','lm8'}});
  appl.prop = prop;
  clear bnd
  bnd.type = {'dir','neu'};
```

```
    bnd.ind = brd;
    appl.bnd = bnd;
    clear equ
    equ.c = 'x*epsmat';
    equ.f = 'x*rho_hole*poi_coeff';
    equ.ind = [1,1];
    appl.equ = equ;
    fem.appl{4} = appl;
    fem.border = 1;
end

function [Chi, EElec, EHole, EExc, Ovl, femE, femH] =...
 SolveEqu(rad, BG, NbrIter)
  % SolveEqu; Iterating the extended effective mass model
  % Parameter: NbrIter: Number of iterations for the EeMm
  % Return: EElec: Energy eigenvalue for the electron
  %         EHole: Energy eigenvalue for the hole
  %         Ovl: Wavefunction overlapp
  %         femE: FemLab-solution for the electron
  %         femH: FemLab-solution for the hole

  global fem;
  % Initialise
  SolH = 0; SolE = 0; SolHPot = 0; SolEPot = 0;

  % Use the Multiphysics mode
  fem=multiphysics(fem);

  % Creates the extended mesh (extended mesh)
  fem.xmesh=meshextend(fem);
```

```
fem.sol=femeig(fem, 'u', 0, 'solcomp',{'u_hole'}, 'outcomp',...
 {'u_hole'}, 'neigs', 1, 'shift', -1);
femH = fem;
EHole = fem.sol.lambda;
SolH = fem.sol.u;


if (NbrIter > 0)
  for i = 1:1:NbrIter
      % Calculate the potential of the hole;
          fem.sol=femlin(fem, 'u', femH.sol, 'solcomp',{'v_hole'}, ...
                         'outcomp', {'v_hole'});
          femHPot = fem;
          SolHPot = fem.sol.u;


      % Calculate the wavefunction of the electron;
          fem.sol=femeig(fem, 'u', femHPot.sol, 'solcomp',{'u_elec'}, ...
                         'outcomp', {'u_elec'}, 'neigs', 1, 'shift', -1);
          femE = fem;
          EElec = fem.sol.lambda;
          SolE = fem.sol.u;


      % Calculate the potential of the electron;
          fem.sol=femlin(fem, 'u', femE.sol, 'solcomp',{'v_elec'}, ...
                         'outcomp', {'v_elec'});
          femEPot = fem;
          SolEPot = fem.sol.u;


      % Calculate the wavefunction of the hole;
          fem.sol=femeig(fem, 'u', femEPot.sol, 'solcomp',{'u_hole'}, ...
                         'outcomp', {'u_hole'}, 'neigs', 1, 'shift', -1);
          femH = fem;
```

```
            EHole = fem.sol.lambda;
            SolH = fem.sol.u;
    end
  else
    % If no iteration is done, the electron wavefunction is going to be
    % calculated without the hole potential
    fem.sol=femeig(fem, 'u', 0, 'solcomp', {'u_elec'}, 'outcomp', ...
                  {'u_elec'}, 'neigs', 1, 'shift', -1);
    femE = fem;
    EElec = fem.sol.lambda;
    SolE = fem.sol.u;
  end

  % Calculate the wavefunction overlap
    fem = CombineSol(fem, SolE, SolH, SolEPot, SolHPot, NbrIter);
    IntHo = postint(fem, 'abs(u_hole)^2');
    IntEl = postint(fem, 'abs(u_elec)^2');
    Chi = postint(fem, 'abs(u_elec)^2 * abs(u_hole)^2')* rad^2/(2*IntHo * IntEl);
    Ovl = postint(fem, 'u_elec*u_hole');
    EExc = EHole + EElec + BG;
    %postsurf(fem, 'u_hole');
    % Normalise, for electron and hole wavefunction are not normalised yet.
    Ovl = Ovl / sqrt(IntEl * IntHo);


function [fem] = CombineSol(fem, SolE, SolH, SolEPot, SolHPot, NbrIter)
  % CombineSol writes all the solutions into one FemLab structure
  % Parameter: fem: FemLab structure the solutions are going to be written to
  %            SolE: Solution for the electron wavefunction
  %            SolH: Solution for the hole wavefunction
  %            SolEPot: Potential of the electron
```

```
  %            SolHPot: Potentisl of the hole
  %            NbrIter: Number of iterations
  % Rckgabe:  fem: FemLab structure


  anz = length(SolE);
  for i = 1:1:anz
    if SolE(i) == 0
      if SolH(i) ~= 0
          SolE(i) = SolH(i);
      else
        if (NbrIter > 0)
            if SolHPot(i) ~= 0
                SolE(i) = SolHPot(i);
            else
                if SolEPot(i) ~= 0
                    SolE(i) = SolEPot(i);
                end
            end
        end
      end
    end
  end
  fem.sol = femsol(SolE, 'lambda', 0);
end
end
```

Appendix B

Extended effective mass approximation with external electric fields

The numerical method and algorithm we used makes it very easy to add a number of external fields into the calculation. In order to accommodate for an external electric field we have to modify equations 3.2 and 3.3 and include additional potentials:

$$H_e = -\frac{\hbar^2}{2m_e^2}\nabla^2 e + V_e(\vec{r}_e) + V_{h,eff}(\vec{r}_e) + V_{ext}(\vec{r}_e), \tag{B.1}$$

$$H_h = -\frac{\hbar^2}{2m_h^2}\nabla^2 h + V_h(\vec{r}_h) + V_{e,eff}(\vec{r}_h) + V_{ext}(\vec{r}_h). \tag{B.2}$$

The added external potentials $V_{ext}(\vec{r}_{e,h})$ allow us to treat external electric fields applied to the NR. In the case of a constant external electric field the potential is given by

$$V_{ext}(\vec{r}) = \vec{F} \cdot \vec{r}, \tag{B.3}$$

where $\vec{F}$ represents the electric field strength. If this vector is oriented parallel or anti-parallel to the NR $\hat{c}$-axis we can solve the problem in 2-dimensional cylinder coordinates. If this vector however has a non-vanishing component perpendicular to the NR $\hat{c}$-axis then the problem needs to be solved in 3-dimensional coordinates.

Bibliography

[1] S. Chandra, F. L. Deepak, J. B. Gruber, and D. K. Sardar, *Synthesis, Morphology, and Optical Characterization of Nanocrystalline Er3+:Y2O3*, Journal of Physical Chemistry C **114**, 874 (2010).

[2] W. Di, X. Wang, and X. Ren, *Nanocrystalline CePO(4):Tb as a novel oxygen sensing material on the basis of its redox responsive reversible luminescence*, Nanotechnology **21**, 75709 (2010).

[3] Z. Y. Feng, P. C. Dai, X. C. Ma, J. H. Zhan, and Z. J. Lin, *Monodispersed cation-disordered cubic AgInS2 nanocrystals with enhanced fluorescence*, Applied Physics Letters **96** (2010).

[4] J. Jiang, J. P. Liu, R. M. Ding, X. X. Ji, Y. Y. Hu, X. Li, A. Z. Hu, F. Wu, Z. H. Zhu, and X. T. Huang, *Direct Synthesis of CoO Porous Nanowire Arrays on Ti Substrate and Their Application as Lithium-Ion Battery Electrodes*, Journal of Physical Chemistry C **114**, 929 (2010).

[5] R. H. Wang, X. W. Wang, and J. H. Xin, *Advanced Visible-Light-Driven Self-Cleaning Cotton by Au/TiO2/SiO2 Photocatalysts*, Acs Applied Materials & Interfaces **2**, 82 (2010).

[6] M. J. Mulvihill, X. Y. Ling, J. Henzie, and P. Yang, *Anisotropic etching of silver nanoparticles for plasmonic structures capable of single-particle SERS*, J Am Chem Soc **132**, 268 (2010).

[7] L. P. Liu, Z. B. Zhuang, T. Xie, Y. G. Wang, J. Li, Q. Peng, and Y. D. Li, *Shape Control of CdSe Nanocrystals with Zinc Blende Structure*, Journal of the American Chemical Society **131**, 16423 (2009).

[8] Y. Zeng, T. Zhang, H. T. Fan, W. Y. Fu, G. Y. Lu, Y. M. Sui, and H. B. Yang, *One-Pot Synthesis and Gas-Sensing Properties of Hierarchical ZnSnO3 Nanocages*, Journal of Physical Chemistry C **113**, 19000 (2009).

[9] L. Manna, E. C. Scher, and A. P. Alivisatos, *Synthesis of soluble and processable rod-, arrow-, teardrop-, and tetrapod-shaped CdSe nanocrystals*, Journal of the American Chemical Society **122**, 12700 (2000).

[10] Y. Li, R. Mastria, A. Fiore, C. Nobile, L. Yin, M. Biasiucci, G. Cheng, A. M. Cucolo, R. Cingolani, L. Manna, and G. Gigli, *Improved Photovoltaic Performance of Heterostructured Tetrapod-Shaped CdSe/CdTe Nanocrystals Using C60 Interlayer*, Advanced Materials **21**, 4461 (2009).

[11] J. L. Baker, A. Widmer-Cooper, M. F. Toney, P. L. Geissler, and A. P. Alivisatos, *Device-Scale Perpendicular Alignment of Colloidal Nanorods*, Nano Letters **10**, 195 (2010).

[12] N. Zhao, K. Liu, J. Greener, Z. H. Nie, and E. Kumacheva, *Close-Packed Superlattices of Side-by-Side Assembled Au-CdSe Nanorods*, Nano Letters **9**, 3077 (2009).

[13] Y. J. Min, M. Akbulut, K. Kristiansen, Y. Golan, and J. Israelachvili, *The role of interparticle and external forces in nanoparticle assembly*, Nature Materials **7**, 527 (2008).

[14] T. Mokari, C. G. Sztrum, A. Salant, E. Rabani, and U. Banin, *Formation of asymmetric one-sided metal-tipped semiconductor nanocrystal dots and rods*, Nature Materials **4**, 855 (2005).

[15] R. Rossetti and L. Brus, *Electron-hole recombination emission as a probe of surface-chemistry in aqueous CdS colloids*, Journal of Physical Chemistry **86**, 4470 (1982).

[16] R. Rossetti, S. Nakahara, and L. E. Brus, *Quantum size effects in the redox potentials, resonance Raman-spectra, and electronic-spectra of CdS crystallites in aqueous-solution*, Journal of Chemical Physics **79**, 1086 (1983).

[17] L. E. Brus, *A simple model for the ionization-potential, electron-affinity, and aqueous redox potentials of small semiconductor crystallites*, Journal of Chemical Physics **79**, 5566 (1983).

[18] L. E. Brus, *Electron-electron and electron-hole interactions in small semiconductor crystallites - the size dependence of the lowest excited electronic state*, Journal of Chemical Physics **80**, 4403 (1984).

[19] M. G. Bawendi, W. L. Wilson, L. Rothberg, P. J. Carroll, T. M. Jedju, M. L. Steigerwald, and L. E. Brus, *Electronic-structure and photoexcited-carrier dynamics in nanometer-sized CdSe clusters*, Physical Review Letters **65**, 1623 (1990).

[20] M. G. Bawendi, P. J. Carroll, W. L. Wilson, and L. E. Brus, *Luminescence properties of CdSe quantum crystallites: Resonance between interior and surface localized states*, The Journal of Chemical Physics **96**, 946 (1992).

[21] C. B. Murray, D. J. Norris, and M. G. Bawendi, *Synthesis and Characterization of Nearly Monodisperse CdE (E = S, Se, Te) Semiconductor Nanocrystallites*, Journal of the American Chemical Society **115**, 8706 (1993).

[22] A. P. Alivisatos, *Semiconductor clusters, nanocrystals, and quantum dots*, Science **271**, 933 (1996).

[23] H. M. Schmidt and H. Weller, *Photochemistry of colloidal semiconductors. 15. Quantum size effects in semiconductor crystallites - Calculation of the energy-spectrum for the confined exciton*, Chemical Physics Letters **129**, 615 (1986).

[24] D. J. Norris, A. Sacra, C. B. Murray, and M. G. Bawendi, *Measurement of the Size-Dependent Hole Spectrum in Cdse Quantum Dots*, Physical Review Letters **72**, 2612 (1994).

[25] M. Bruchez, M. Moronne, P. Gin, S. Weiss, and A. P. Alivisatos, *Semiconductor nanocrystals as fluorescent biological labels*, Science **281**, 2013 (1998).

[26] A. Chemseddine and H. Weller, *Highly monodisperse quantum sized CdS particles by size-selective precipitation*, Berichte Der Bunsen-Gesellschaft-Physical Chemistry Chemical Physics **97**, 636 (1993).

[27] N. Gaponik, D. V. Talapin, A. L. Rogach, K. Hoppe, E. V. Shevchenko, A. Kornowski, A. Eychmuller, and H. Weller, *Thiol-capping of CdTe nanocrystals: An alternative to organometallic synthetic routes*, Journal of Physical Chemistry B **106**, 7177 (2002).

[28] B. O. Dabbousi, J. RodriguezViejo, F. V. Mikulec, J. R. Heine, H. Mattoussi, R. Ober, K. F. Jensen, and M. G. Bawendi, *(CdSe)ZnS core-shell quantum dots: Synthesis and characterization of a size series of highly luminescent nanocrystallites*, Journal of Physical Chemistry B **101**, 9463 (1997).

[29] X. G. Peng, M. C. Schlamp, A. V. Kadavanich, and A. P. Alivisatos, *Epitaxial growth of highly luminescent CdSe/CdS core/shell nanocrystals with photostability and electronic accessibility*, Journal of the American Chemical Society **119**, 7019 (1997).

[30] W. J. Parak, T. Pellegrino, and C. Plank, *Labelling of cells with quantum dots*, Nanotechnology **16**, R9 (2005).

[31] W. Liu, M. Howarth, A. B. Greytak, Y. Zheng, D. G. Nocera, A. Y. Ting, and M. G. Bawendi, *Compact Biocompatible Quantum Dots Functionalized for Cellular Imaging*, Journal of the American Chemical Society **130**, 1274 (2008).

[32] R. L. Orndorff, M. R. Warnement, J. N. Mason, R. D. Blakely, and S. J. Rosenthal, *Quantum Dot Ex Vivo Labeling of Neuromuscular Synapses*, Nano Letters **8**, 780 (2008).

[33] N. P. Stern, M. Poggio, M. H. Bartl, E. L. Hu, G. D. Stucky, and D. D. Awschalom, *Spin dynamics in electrochemically charged CdSe quantum dots*, Physical Review B **72**, 161303 (2005).

[34] J. Berezovsky, O. Gywat, F. Meier, D. Battaglia, X. Peng, and D. D. Awschalom, *Initialization and read-out of spins in coupled core-shell quantum dots*, Nature Physics **2**, 831 (2006).

[35] I. Zutic, J. Fabian, and S. Das Sarma, *Spintronics: Fundamentals and applications*, Reviews of Modern Physics **76**, 323 (2004).

[36] S. Chanyawadee, R. T. Harley, M. Henini, D. V. Talapin, and P. G. Lagoudakis, *Photocurrent enhancement in hybrid nanocrystal quantum-dot p-i-n photovoltaic devices*, Physical Review Letters **102**, 077402 (2009).

[37] C. P. Li, S. W. Yeh, H. C. Chang, J. Y. Huang, and K. H. Wei, *Effect of the orientation of CdSe nanorods on the electron mobility of CdSe/P4VP nanodomains self-assembled within a poly(styrene-b-(4)-vinyipyridine) diblock copolymer thin film*, Small **2**, 359 (2006).

[38] S. Nizamoglu, E. Sari, J. H. Baek, I. H. Lee, and H. V. Demir, *Green/Yellow Solid-State Lighting via Radiative and Nonradiative Energy Transfer Involving Colloidal Semiconductor Nanocrystals*, Ieee Journal of Selected Topics in Quantum Electronics **15**, 1163 (2009).

[39] S. Nizamoglu, O. Akin, and H. V. Demir, *Quantum efficiency enhancement in nanocrystals using nonradiative energy transfer with optimized donor-acceptor ratio for hybrid LEDs*, Applied Physics Letters **94**, 243107 (2009).

[40] V. Sukhovatkin, S. Hinds, L. Brzozowski, and E. H. Sargent, *Colloidal Quantum-Dot Photodetectors Exploiting Multiexciton Generation*, Science **324**, 1542 (2009).

[41] D. V. Talapin, R. Koeppe, S. Gotzinger, A. Kornowski, J. M. Lupton, A. L. Rogach, O. Benson, J. Feldmann, and H. Weller, *Highly emissive colloidal CdSe/CdS heterostructures of mixed dimensionality*, Nano Letters **3**, 1677 (2003).

[42] A. L. Efros, M. Rosen, M. Kuno, M. Nirmal, D. J. Norris, and M. Bawendi, *Band-edge exciton in quantum dots of semiconductors with a degenerate valence band: Dark and bright exciton states*, Physical Review B **54**, 4843 (1996).

[43] M. Kuno, M. Nirmal, G. Bawendi, A. Efros, and M. Rosen, *Magnetic circular dichroism study of CdSe quantum dots*, Journal of Chemical Physics **108**, 4242 (1998).

[44] M. Chamarro, C. Gourdon, P. Lavallard, O. Lublinskaya, and A. I. Ekimov, *Enhancement of electron-hole exchange interaction in CdSe nanocrystals: A quantum confinement effect*, Physical Review B **53**, 1336 (1996).

[45] E. Johnston-Halperin, D. D. Awschalom, S. A. Crooker, A. L. Efros, M. Rosen, X. Peng, and A. P. Alivisatos, *Spin spectroscopy of dark excitons in CdSe quantum dots to 60 T*, Physical Review B **63**, 205309 (2001).

[46] M. Furis, J. A. Hollingsworth, V. I. Klimov, and S. A. Crooker, *Time- and polarization-resolved optical spectroscopy of colloidal CdSe nanocrystal quantum dots in high magnetic fields*, Journal of Physical Chemistry B **109**, 15332 (2005).

[47] M. Furis, H. Htoon, M. A. Petruska, V. I. Klimov, T. Barrick, and S. A. Crooker, *Bright-exciton fine structure and anisotropic exchange in CdSe nanocrystal quantum dots*, Physical Review B **73**, 241313 (2006).

[48] H. Htoon, S. A. Crooker, M. Furis, S. Jeong, A. L. Efros, and V. I. Klimov, *Anomalous Circular Polarization of Photoluminescence Spectra of Individual CdSe Nanocrystals in an Applied Magnetic Field*, Physical Review Letters **102**, 017402 (2009).

[49] J. A. Gupta, D. D. Awschalom, X. Peng, and A. P. Alivisatos, *Spin coherence in semiconductor quantum dots*, Physical Review B **59**, R10421 (1999).

[50] J. A. Gupta, D. D. Awschalom, A. L. Efros, and A. V. Rodina, *Spin dynamics in semiconductor nanocrystals*, Physical Review B **66**, 125307 (2002).

[51] M. Ouyang and D. D. Awschalom, *Coherent spin transfer between molecularly bridged quantum dots*, Science **301**, 1074 (2003).

[52] S. A. Empedocles, R. Neuhauser, K. Shimizu, and M. G. Bawendi, *Photoluminescence from single semiconductor nanostructures*, Advanced Materials **11**, 1243 (1999).

[53] E. Rothenberg, M. Kazes, E. Shaviv, and U. Banin, *Electric field induced switching of the fluorescence of single semiconductor quantum rods*, Nano Letters **5**, 1581 (2005).

[54] J. Muller, J. M. Lupton, P. G. Lagoudakis, F. Schindler, R. Koeppe, A. L. Rogach, J. Feldmann, D. V. Talapin, and H. Weller, *Wave function engineering in elongated*

semiconductor nanocrystals with heterogeneous carrier confinement, Nano Letters **5**, 2044 (2005).

[55] S. J. Park, S. Link, W. L. Miller, A. Gesquiere, and P. F. Barbara, *Effect of electric field on the photoluminescence intensity of single CdSe nanocrystals*, Chemical Physics **341**, 169 (2007).

[56] K. Becker, J. M. Lupton, J. Muller, A. L. Rogach, D. V. Talapin, H. Weller, and J. Feldmann, *Electrical control of Forster energy transfer*, Nature Materials **5**, 777 (2006).

[57] R. M. Kraus, P. G. Lagoudakis, A. L. Rogach, D. V. Talapin, H. Weller, J. M. Lupton, and J. Feldmann, *Room-temperature exciton storage in elongated semiconductor nanocrystals*, Physical Review Letters **98** (2007).

[58] V. M. Agranovich, G. C. La Rocca, and F. Bassani, *Efficient electronic energy transfer from a semiconductor quantum well to an organic material*, JETP Letters **66**, 748 (1997).

[59] D. Basko, G. C. La Rocca, F. Bassani, and V. M. Agranovich, *Forster energy transfer from a semiconductor quantum well to an organic material overlayer*, European Physical Journal B **8**, 353 (1999).

[60] D. M. Basko, V. M. Agranovich, F. Bassani, and G. C. La Rocca, *Energy transfer from a semiconductor quantum dot to an organic matrix*, European Physical Journal B **13**, 653 (2000).

[61] M. Achermann, M. A. Petruska, S. Kos, D. L. Smith, D. D. Koleske, and V. I. Klimov, *Energy-transfer pumping of semiconductor nanocrystals using an epitaxial quantum well*, Nature **429**, 642 (2004).

[62] G. Heliotis, G. Itskos, R. Murray, M. D. Dawson, I. M. Watson, and D. D. C. Bradley, *Hybrid inorganic/organic semiconductor heterostructures with efficient non-radiative energy transfer*, Advanced Materials **18**, 334 (2006).

[63] S. Kos, M. Achermann, V. I. Klimov, and D. L. Smith, *Different regimes of Forster-type energy transfer between an epitaxial quantum well and a proximal monolayer of semiconductor nanocrystals*, Physical Review B **71** (2005).

[64] M. Achermann, M. A. Petruska, D. D. Koleske, M. H. Crawford, and V. I. Klimov, *Nanocrystal-based light-emitting diodes utilizing high-efficiency nonradiative energy transfer for color conversion*, Nano Letters **6**, 1396 (2006).

[65] N. W. Ashcroft and N. D. Mermin, *Solid State Physics*, Thomson Learning (1976).

[66] C. Kittel, *Introduction to Solid State Physics*, John Willey & Sons, 8th Edition (2004).

[67] H. Ibach and H. Lüth, *Solid-state Physics: An Introduction to Principles of Materials Science*, Springer, 3rd Edition (2003).

[68] C. E. Mortimer, *Chemistry: A Conceptual Approach*, Wadsworth Publishing Co. Inc., 5th Edition (1983).

[69] D. J. Norris, *Electronic Structure in Semiconductor Nanocrystals*, in V. I. Klimov, Editor, *Semiconductor and Metal Nanocrystals*, Volume 87 of *Optical Engineering*, 65–100, Marcel Dekker, Inc., New York (2004).

[70] P. Eckerlin, H. Kandler, and A. Stegherr, *Landolt-Bornstein: Numerical Data and Functional Relationships in Science and Technology: Group 3: Condensed Matter: Structure Data of Elements and Intermetallic Phases*, Springer, Berlin - Heidelberg - New York (1971).

[71] S. Sapra, S. Mayilo, T. A. Klar, A. L. Rogach, and J. Feldmann, *Bright White-Light Emission from Semiconductor Nanocrystals: by Chance and by Design*, Advanced Materials **19**, 569 (2007).

[72] S. V. Gaponenko, *Optical Properties of Semiconductor Nanocrystals*, Cambridge Studies in Modern Optics, Cambridge University Press, Cambridge (1998).

[73] A. L. Efros and M. Rosen, *The electronic structure of semiconductor nanocrystals*, Annual Review of Materials Science **30**, 475 (2000).

[74] Y. Kayanuma, *Wannier exciton in microcrystals*, Solid State Communications—Solid State Communications **59**, 405 (1986).

[75] D. J. Norris, A. L. Efros, M. Rosen, and M. G. Bawendi, *Size dependence of exciton fine structure in CdSe quantum dots*, Physical Review B **53**, 16347 (1996).

[76] A. L. Efros, *Luminescence Polarization of Cdse Microcrystals*, Physical Review B **46**, 7448 (1992).

[77] T. Förster, *Zwischenmolekulare Energiewanderung und Fluorezenz*, Annalen der Physik **2**, 55 (1948).

[78] D. L. Dexter, *A Theory of Sensitized Luminescence in Solids*, Journal of Chemical Physics **21**, 836 (1953).

[79] T. Franzl, D. S. Koktysh, T. A. Klar, A. L. Rogach, J. Feldmann, and N. Gaponik, *Fast energy transfer in layer-by-layer assembled CdTe nanocrystal bilayers*, Applied Physics Letters **84**, 2904 (2004).

[80] S. Hohng, C. Joo, and T. Ha, *Single-molecule three-color FRET*, Biophysical Journal **87**, 1328 (2004).

[81] S. Blumstengel, S. Sadofev, C. Xu, J. Puls, and F. Henneberger, *Converting Wannier into Frenkel excitons in an inorganic/organic hybrid semiconductor nanostructure*, Physical Review Letters **97** (2006).

[82] S. Rohrmoser, J. Baldauf, R. T. Harley, P. G. Lagoudakis, S. Sapra, A. Eychmuller, and I. M. Watson, *Temperature dependence of exciton transfer in hybrid quantum well/nanocrystal heterostructures*, Applied Physics Letters **91**, 3 (2007).

[83] L. Landau and E. Lifshitz, *Quantum Mechanics*, Volume 3 of *Course of Theoretical Physics*, Pergamon Press, Oxford (1960).

[84] R. Zimmermann, F. Grosse, and E. Runge, *Excitons in semiconductor nanostructures with disorder*, Pure and Applied Chemistry **69**, 1179 (1997).

[85] C. J. Deatcher, C. Liu, S. Pereira, M. Lada, A. G. Cullis, Y. J. Sun, O. Brandt, and I. M. Watson, *In situ optical reflectometry applied to growth of indium gallium*

nitride epilayers and multi-quantum well structures, Semiconductor Science and Technology **18**, 212 (2003).

[86] L. T. Tan, R. W. Martin, K. P. O'Donnell, and I. M. Watson, *Photoluminescence and phonon satellites of single InGaN/GaN quantum wells with varying GaN cap thickness*, Applied Physics Letters **89**, 101910 (2006).

[87] G. Itskos, G. Heliotis, P. G. Lagoudakis, J. M. Lupton, N. P. Barradas, E. Alves, S. Pereira, I. M. Watson, M. D. Dawson, J. Feldmann, R. Murray, and D. D. C. Bradley, *Efficient dipole-dipole coupling of Mott-Wannier and Frenkel excitons in (Ga,In)N quantum well/polyfluorene semiconductor heterostructures*, Physical Review B **76** (2007).

[88] D. V. Talapin, A. Rogach, A. Kornowski, M. Haase, and H. Weller, *Highly Luminescent Monodisperse CdSe and CdSe/ZnS Nanocrystals Synthesized in a Hexadecylamine-Trioctylphosphine Oxide-Trioctylphospine Mixture*, Nano Letters **1**, 207 (2001).

[89] U. E. H. Laheld and G. T. Einevoll, *Excitons in CdSe quantum dots*, Physical Review B **55**, 5184 (1997).

[90] G. T. Einevoll, *Confinement of excitons in quantum dots*, Physical Review B **45**, 3410 (1992).

[91] K. L. Janssens, B. Partoens, and F. M. Peeters, *Magnetoexcitons in planar type-II quantum dots in a perpendicular magnetic field*, Physical Review B **64** (2001).

[92] L. Edsberg, *An Introduction to Computation and Modeling for Differential Equations*, WileyBlackwell (2008).

[93] J. Muller, *Elektrische Manipulation der Lichtemission von einzelnen CdSe/CdS Nanostäbchen*, PhD thesis (2005).

[94] T. J. Lin, H. L. Chen, Y. F. Chen, and S. F. Cheng, *Room-temperature nanolaser from CdSe nanotubes embedded in anodic aluminum oxide nanocavity arrays*, Applied Physics Letters **93**, 223903 (2008).

[95] R. D. Schaller, M. Sykora, J. M. Pietryga, and V. I. Klimov, *Seven excitons at a cost of one: Redefining the limits for conversion efficiency of photons into charge carriers*, Nano Letters **6**, 424 (2006).

[96] X. H. Gao, Y. Y. Cui, R. M. Levenson, L. W. K. Chung, and S. M. Nie, *In vivo cancer targeting and imaging with semiconductor quantum dots*, Nature Biotechnology **22**, 969 (2004).

[97] L. S. Li, J. Walda, L. Manna, and A. P. Alivisatos, *Semiconductor nanorod liquid crystals*, Nano Letters **2**, 557 (2002).

[98] S. Acharya, S. Kundu, J. P. Hill, G. J. Richards, and K. Ariga, *Nanorod-driven orientational control of liquid crystal for polarization-tailored electro-optic devices*, Advanced Materials **21**, 989 (2009).

[99] A. H. Nethercot, *Prediction of Fermi energies and photoelectric thresholds based on electronegativity concepts*, Physical Review Letters **33**, 1088 (1974).

[100] L. S. Li, M. Marjanska, G. H. J. Park, A. Pines, and A. P. Alivisatos, *Isotropic-liquid crystalline phase diagram of a CdSe nanorod solution*, Journal of Chemical Physics **120**, 1149 (2004).

[101] N. Le Thomas, E. Herz, O. Schops, U. Woggon, and M. V. Artemyev, *Exciton fine structure in single CdSe nanorods*, Physical Review Letters **94**, 016803 (2005).

[102] M. Nirmal, D. J. Norris, M. Kuno, M. G. Bawendi, A. L. Efros, and M. Rosen, *Observation of the Dark Exciton in CdSe Quantum Dots*, Physical Review Letters **75**, 3728 (1995).

[103] J. Smith, P. Sher, S. Daniels, N. Pickett, P. O'Brien, P. A. Dalgarno, and R. J. Warburton, *Power law dynamics at nanosecond time scales in the fluorescence decay of semiconductor nanocrystals*, arXiv:cond-mat/0604292v2 (2008).

[104] H. Ham and H. N. Spector, *Exciton linewidth due to scattering by polar optical phonons in semiconducting cylindrical quantum wire structures*, Physical Review B **62**, 13599 (2000).

[105] V. D. Kulakovskii, G. Bacher, R. Weigand, T. Kummell, A. Forchel, E. Borovitskaya, K. Leonardi, and D. Hommel, *Fine structure of biexciton emission in symmetric and asymmetric CdSe/ZnSe single quantum dots*, Physical Review Letters **82**, 1780 (1999).

[106] M. Bayer, A. Kuther, A. Forchel, A. Gorbunov, V. B. Timofeev, F. Schafer, J. P. Reithmaier, T. L. Reinecke, and S. N. Walck, *Electron and hole g factors and exchange interaction from studies of the exciton fine structure in In0.60Ga0.40As quantum dots*, Physical Review Letters **82**, 1748 (1999).

[107] J. J. Finley, D. J. Mowbray, M. S. Skolnick, A. D. Ashmore, C. Baker, A. F. G. Monte, and M. Hopkinson, *Fine structure of charged and neutral excitons in InAs-Al0.6Ga0.4As quantum dots*, Physical Review B **66** (2002).

[108] J. Puls, M. Rabe, H. J. Wnsche, and F. Henneberger, *Magneto-optical study of the exciton fine structure in self-assembled CdSe quantum dots*, Physical Review B **60**, R16303 (1999).

[109] D. Gammon, E. S. Snow, B. V. Shanabrook, D. S. Katzer, and D. Park, *Fine Structure Splitting in the Optical Spectra of Single GaAs Quantum Dots*, Physical Review Letters **76**, 3005 (1996).

[110] S. V. Goupalov and E. L. Ivchenko, *Electron–hole long-range exchange interaction in semiconductor quantum dots*, Journal of Crystal Growth **184-185**, 393 (1998).

[111] M. Chamarro, C. Gourdon, P. Lavallard, and A. I. Ekimov, *Enhancement of exciton exchange interaction by quantum confinement in CdSe nanocrystals*, Japanese Journal of Applied Physics **34**, 12 (1995).

[112] U. Woggon, F. Gindele, O. Wind, and C. Klingshirn, *Exchange interaction and phonon confinement in CdSe quantum dots*, Physical Review B (Condensed Matter)—Physical Review B (Condensed Matter) **54**, 1506 (1996).

[113] A. B. Kapustina, B. V. Petrov, A. V. Rodina, and R. P. Seisyan, *Weak- and strong-field magnetooptics of wurtzite CdSe: parameters of quasi-cubic approximation*, Journal of Crystal Growth **214-215**, 899 (2000).

[114] S. N. Walck and T. L. Reinecke, *Exciton diamagnetic shift in semiconductor nanostructures*, Physical Review B **57**, 9088 (1998).

[115] S. Kudera, L. Carbone, L. Manna, and W. J. Parak, *Growth mechanism, shape and composition control of semiconductor nanocrystals*, in A. L. Rogach, Editor, *Semiconductor Nanocrystal Quantum Dots*, 1–35, SpringerWienNewYork (2008).

[116] T. Someya, H. Akiyama, and H. Sakaki, *Laterally Squeezed Excitonic Wave Function in Quantum Wires*, Physical Review Letters **74**, 3664 (1995).

[117] M. Bayer, S. N. Walck, T. L. Reinecke, and A. Forchel, *Exciton binding energies and diamagnetic shifts in semiconductor quantum wires and quantum dots*, Physical Review B **57**, 6584 (1998).

[118] M. Funato, C. Bradford, A. Balocchi, J. Smith, K. Prior, and B. Cavenett, *Photoluminescence Studies of the Formation of MgS/CdSe Quantum Dots Grown by Molecular Beam Epitaxy*, physica status solidi (b) **229**, 477 (2002).

[119] K. Kyhm, J. H. Kim, S. M. Kim, and H.-s. Yang, *Gain dynamics and excitonic transition in CdSe colloidal quantum dots*, Optical Materials **30**, 158 (2007).

[120] O. Millo, D. Katz, D. Steiner, E. Rothenberg, T. Mokari, M. Kazes, and U. Banin, *Charging and quantum size effects in tunnelling and optical spectroscopy of CdSe nanorods*, Nanotechnology **15**, R1 (2004).

[121] J. Muller, J. M. Lupton, A. L. Rogach, J. Feldmann, D. V. Talapin, and H. Weller, *Monitoring surface charge movement in single elongated semiconductor nanocrystals*, Physical Review Letters **93**, 4 (2004).

[122] J. Muller, J. M. Lupton, A. L. Rogach, J. Feldmann, D. V. Talapin, and H. Weller, *Monitoring surface charge migration in the spectral dynamics of single CdSe/CdS nanodot/nanorod heterostructures*, Physical Review B **72**, 12 (2005).

[123] R. M. Kraus, P. G. Lagoudakis, J. Muller, A. L. Rogach, J. M. Lupton, J. Feldmann, D. V. Talapin, and H. Weller, *Interplay between auger and ionization processes in nanocrystal quantum dots*, Journal of Physical Chemistry B **109**, 18214 (2005).

[124] R. Kohlrausch, *Theorie des elektrischen Rückstandes in der Leidener Flasche*, Annalen der Physik und Chemie **167**, 179 (1854).

[125] C. P. Lindsey and G. D. Patterson, *Detailed comparison of the Williams-Watts and Cole-Davidson functions*, Journal of Chemical Physics **73**, 3348 (1980).

[126] J. C. Phillips, *Stretched exponential relaxation in molecular and electronic glasses*, Reports on Progress in Physics **59**, 1133 (1996).

[127] M. N. Berberan-Santos, E. N. Bodunov, and B. Valeur, *Mathematical functions for the analysis of luminescence decays with underlying distributions 1. Kohlrausch decay function (stretched exponential)*, Chemical Physics **315**, 171 (2005).

[128] B. R. Fisher, H. J. Eisler, N. E. Stott, and M. G. Bawendi, *Emission intensity dependence and single-exponential behavior in single colloidal quantum dot fluorescence lifetimes*, Journal of Physical Chemistry B **108**, 143 (2004).

[129] A. F. van Driel, I. S. Nikolaev, P. Vergeer, P. Lodahl, D. Vanmaekelbergh, and W. L. Vos, *Statistical analysis of time-resolved emission from ensembles of semiconductor quantum dots: Interpretation of exponential decay models*, Physical Review B **75** (2007).

[130] X. W. Zhang and J. B. Xia, *Effects of magnetic field on the electronic structure of wurtzite quantum dots: Calculations using effective-mass envelope function theory*, Physical Review B **72**, 075363 (2005).

[131] S. A. Crooker, T. Barrick, J. A. Hollingsworth, and V. I. Klimov, *Multiple temperature regimes of radiative decay in CdSe nanocrystal quantum dots: Intrinsic limits to the dark-exciton lifetime*, Applied Physics Letters **82**, 2793 (2003).

[132] L. Besombes, L. Marsal, K. Kheng, T. Charvolin, L. S. Dang, A. Wasiela, and H. Mariette, *Fine structure of the exciton in a single asymmetric CdTe quantum dot*, Journal of Crystal Growth **214**, 742 (2000).

[133] Y. B. Lyanda-Geller, T. L. Reinecke, and M. Bayer, *Exciton fine structure in coupled quantum dots*, Physical Review B **69** (2004).

[134] A. Vinattieri, J. Shah, T. C. Damen, D. S. Kim, L. N. Pfeiffer, M. Z. Maialle, and L. J. Sham, *Exciton Dynamics in Gaas Quantum-Wells under Resonant Excitation*, Physical Review B **50**, 10868 (1994).

[135] B. Alen, J. Bosch, D. Granados, J. Martinez-Pastor, J. M. Garcia, and L. Gonzalez, *Oscillator strength reduction induced by external electric fields in self-assembled quantum dots and rings*, Physical Review B **75**, 045319 (2007).

[136] P. A. Dalgarno, J. M. Smith, J. McFarlane, B. D. Gerardot, K. Karrai, A. Badolato, P. M. Petroff, and R. J. Warburton, *Coulomb interactions in single charged self-assembled quantum dots: Radiative lifetime and recombination energy*, Physical Review B **77**, 245311 (2008).

[137] G. Bastard, E. E. Mendez, L. L. Chang, and L. Esaki, *Variational calculations on a quantum well in an electric field*, Physical Review B **28**, 3241 (1983).

[138] H. J. Polland, L. Schultheis, J. Kuhl, E. O. Gobel, and C. W. Tu, *Lifetime enhancement of two-dimensional excitons by the quantum-confined Stark-effect*, Physical Review Letters **55**, 2610 (1985).

[139] X. G. Peng, L. Manna, W. D. Yang, J. Wickham, E. Scher, A. Kadavanich, and A. P. Alivisatos, *Shape control of CdSe nanocrystals*, Nature **404**, 59 (2000).

[140] N. P. Barradas, E. Alves, S. Pereira, and I. M. Watson, *RBS analysis of InGaN/-GaN quantum wells for hybrid structures with efficient Forster coupling*, Nuclear Instruments & Methods in Physics Research Section B-Beam Interactions with Materials and Atoms **266**, 1402 (2008).

[141] Z. A. Peng and X. Peng, *Formation of High-Quality CdTe, CdSe, and CdS Nanocrystals Using CdO as Precursor*, Journal of the American Chemical Society **123**, 183 (2001).

[142] D. J. Norris, M. Nirmal, C. B. Murray, A. Sacra, and M. G. Bawendi, *Size-dependent optical spectroscopy of II-VI semiconductor nanocrystallites (quantum dots)*, Zeitschrift Fur Physik D-Atoms Molecules and Clusters **26**, 355 (1993).

[143] V. I. Klimov, D. W. McBranch, C. A. Leatherdale, and M. G. Bawendi, *Electron and hole relaxation pathways in semiconductor quantum dots*, Physical Review B **60**, 13740 (1999).

[144] V. I. Klimov, A. A. Mikhailovsky, D. W. McBranch, C. A. Leatherdale, and M. G. Bawendi, *Quantization of multiparticle Auger rates in semiconductor quantum dots*, Science **287**, 1011 (2000).

[145] E. S. Jeon, V. Kozlov, Y. K. Song, A. Vertikov, M. Kuball, A. V. Nurmikko, H. Liu, C. Chen, R. S. Kern, C. P. Kuo, and M. G. Craford, *Recombination dynamics in InGaN quantum wells*, Applied Physics Letters **69**, 4194 (1996).

[146] M. Artemyev, B. Moller, and U. Woggon, *Unidirectional alignment of CdSe nanorods*, Nano Letters **3**, 509 (2003).

[147] I. Dierking, G. Scalia, P. Morales, and D. LeClere, *Aligning and reorienting carbon nanotubes with nematic liquid crystals*, Advanced Materials **16**, 865 (2004).

[148] J. Lagerwall, G. Scalia, M. Haluska, U. Dettlaff-Weglikowska, S. Roth, and F. Giesselmann, *Nanotube alignment using lyotropic liquid crystals*, Advanced Materials **19**, 359 (2007).

[149] R. A. M. Hikmet, P. T. K. Chin, D. V. Talapin, and H. Weller, *Polarized-light-emitting quantum-rod diodes*, Advanced Materials **17**, 1436 (2005).